THESIS

EFFECT OF LATENT HEATING ON MESOSCALE VORTEX DEVELOPMENT DURING EXTREME PRECIPITATION: COLORADO, SEPTEMBER 2013

Submitted by

Annareli Morales

Department of Atmospheric Science

In partial fulfillment of the requirements

For the Degree of Master of Science

Colorado State University

Fort Collins, Colorado

Fall 2014

Master's Committee:

Advisor: Sonia M. Kreidenweis
Co-Advisor: Russ S. Schumacher

Jorge A. Ramirez

ABSTRACT

EFFECT OF LATENT HEATING ON MESOSCALE VORTEX DEVELOPMENT DURING EXTREME PRECIPITATION: COLORADO, SEPTEMBER 2013

From 9-16 September 2013, a slow-moving cut-off low in the southwestern U.S. funneled unseasonal amounts of moisture to the Colorado Front Range, resulting in extreme precipitation and flooding. The heaviest precipitation during the September 2013 event occurred over the northern Colorado Front Range, producing a 7-day total of over 380 mm of rain. The flash flooding caused over $3 billion in damage to property and infrastructure and resulted in eight fatalities.

This study will focus on the precipitation and mesoscale features during 11-12 September 2013 in Boulder, CO. During the evening of 11 September, Boulder experienced flash flooding as a result of high rain rates accumulating over 180 mm of rain in 6 hours. From 0400-0700 UTC 12 September, a mesoscale vortex (mesovortex) was observed to travel northwestward towards Boulder. This circulation enhanced upslope flow and was associated with localized deep convection. The mesovortex originated in an area common for the development of a lee vortex known as the Denver Cyclone. We hypothesize that this mesoscale vortex is *not* associated with lee vortex formation, such as the Denver Cyclone, but developed through the release of latent heat from microphysical process.

The Advanced Research Weather Research and Forecast (ARW) model was used to 1) produce a control simulation that properly represented the evolution and processes of interest during the event and 2) test the importance of latent heating to the development and evolution of the mesovortex. The results from various latent heating experiments suggested that the

mesovortex did not develop through lee vortex formation and the latent heat released just before and during the mesovortex event was important to its development. Results also showed latent heating affected the flow field, resulting in a positive feedback between the circulation, associated low-level jet, and convection leading to further upslope flow and precipitation development. Further experiments showed condensation of cloud water was the dominant microphysical process responsible for a positive vertical gradient in latent heating near the surface. This gradient led to potential vorticity generation; a similar mechanism to that of a mesoscale convective vortex, except closer to the surface. Finally, an experiment where the latent heating was reduced by half after 1800 UTC 11 September resulted in no mesovortex development and a substantial decrease in precipitation. The results from this study have relevant implications to the representation of microphysical processes in numerical weather prediction models. The capability to forecast the development of these mesovortices and their subsequent environmental and hydrological effects could be critical for decision makers and the public, given their association with high rain fall rates.

ACKNOWLEDGEMENTS

I would like to thank my advisors, Sonia Kreidenweis and Russ Schumacher, for their continuous support, guidance, patience, and knowledge. Thank you for believing in me when I did not. Thanks to Jorge Ramirez for his helpful revisions and comments to improve this work. Big thanks to Eric Aligo for his assistance with implementing the microphysics heating calculations into the parameterization and patience with answering all my questions. Thank you to Greg Thompson, Hugh Morrison, and Sue van den Heever for their helpful discussions and insightful suggestions. I would also like to thank Jamie Schmidt for all her help throughout this process, from checking that my application materials were in to making sure I had all the signatures I needed to submit my thesis. Last, but not least, I would like to thank my friends and family for their love and support. I would have lost my mind without you all.

This research was supported by the Significant Opportunities in Atmospheric Research and Science (SOARS) program and the National Science Foundation Science and Technology Center for Multi-Scale Modeling of Atmospheric Processes (CMMAP), managed by Colorado State University under cooperative agreement No. AGS-0425247. SOARS is managed by the University Corporation for Atmospheric Research and is funded by the National Science Foundation, the National Oceanic and Atmospheric Administration (NOAA), the Cooperative Institute for Research in Environmental Science, the University of Colorado at Boulder, and CMMAP.

The forecast verification in this study was performed with the use of the Model Evaluation Tools (MET). MET was developed at the National Center for Atmospheric Research (NCAR) through grants from the United States Air Force Weather Agency (AFWA) and NOAA. NCAR is sponsored by the United States National Science Foundation.

DEDICATION

This work is dedicated to my late father, Francisco Morales. It is one step closer to fulfilling a promise.

TABLE OF CONTENTS

LIST OF TABLES

LIST OF FIGURES

1. Introduction

Flash flooding is not uncommon in Colorado. The state has a long history of extreme precipitation and flooding events (McKee and Doesken 1997; Grigg et al. 1999; Bolinger 2013). Colorado's complex topography (Figure 1.1) plays a large role in the production of precipitation. The dramatic rise in elevation from the eastern plains towards the mountainous western half of the state (over 2,000 m difference in elevation) provides mechanical forcing from orographic lift to vertically transport moist, unstable air parcels to their condensation level. Thus, there is a tendency for high rainfall events in Colorado to occur along the Front Range and eastern foothills of the Rocky Mountains (McKee and Doesken 1997).

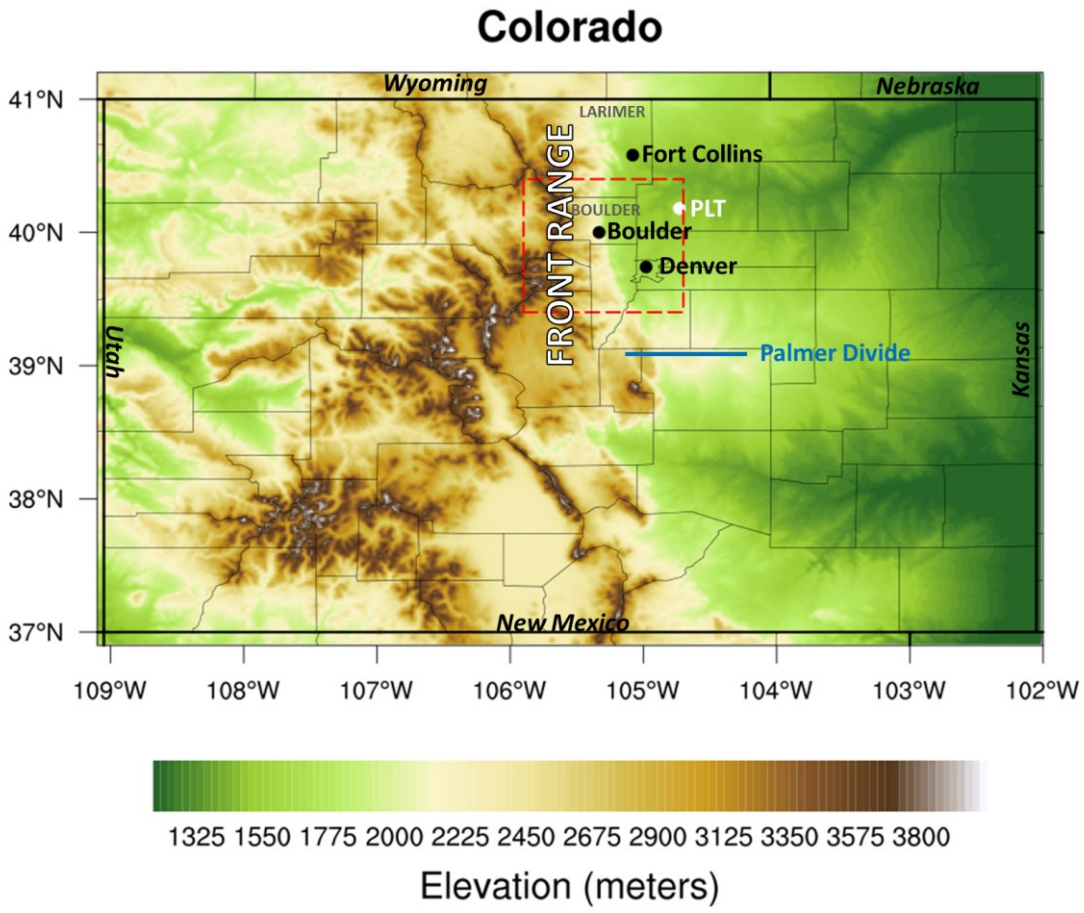

Figure 1.1: Topography of Colorado using ETOPO1 GRM data (Amante and Eakins 2009).

Elevation of Colorado (m; color) and US states (thick line) and county (thin line) boundaries depicted. The cities of Fort Collins, Boulder, and Denver are placed as a reference, as well as other geographic markers. The white filled-in circle labeled "PLT" represents the location of the Platteville profiler. The red dashed box depicts the domain over which averaging is performed in the analysis.

Along the Colorado Front Range, flash flooding events tend to occur more frequently in June, July, and August (Maddox et al. 1980). During these months the North American Monsoon takes place in the southwestern U.S., characterized by a southerly shift in the large-scale wind patterns resulting in increased moisture transport from the eastern Pacific Ocean and Gulf of California (Adams and Comrie 1997). Thus, the monsoon season results in a higher availability of precipitable water, i.e. the amount of water vapor in a column of air that could condense and fall out as rain (McKee and Doesken 1997).

Maddox et al. (1980) aimed to classify flash floods and heavy rainfall events over the western U.S. and found that most of them occur with "weak large-scale patterns", which otherwise would look benign to a forecaster. The large-scale pattern associated with Type I western flooding events (most common east of the Sierra Mountain ranges) involves a northward-moving, weak short-wave trough along the western edge of an upper-level ridge (Figure 1.2; Maddox et al. 1980). Conditions during these types of flash flooding events were characterized by high surface dewpoints (>13°C (55°F)) and deep moisture from the surface to 300 hPa, with precipitable water values exceeding 20 mm between the surface and 500 hPa (Maddox et al. 1980). The atmospheric profiles during this type of event tend to have tropical characteristics (high tropopause height, nearly saturated conditions into the upper troposphere) as well as veering winds with height (associated with warm air advection) (Maddox et al. 1980). Similar conditions during the week of 9 September 2013 setup the ingredients which would result in extreme precipitation and flash flooding for large portions of Colorado.

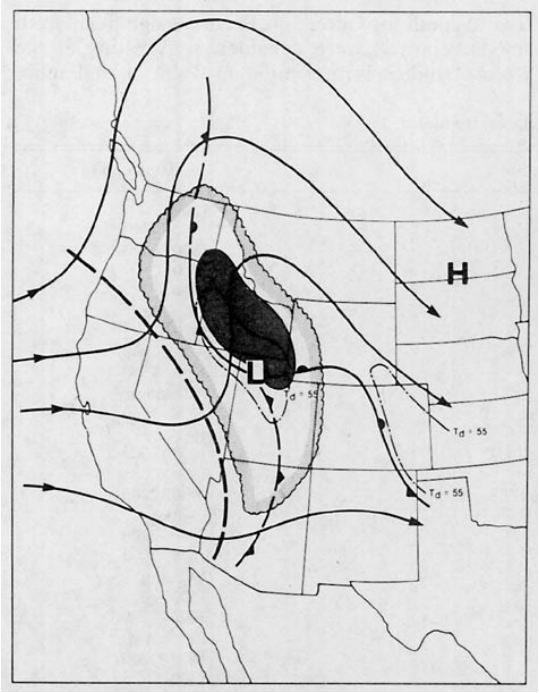

Figure 1.2: 500 hPa pattern associated with Type I western flood events (from Maddox et al. 1980).

1.1 9-16 September 2013 – Colorado Extreme Rainfall and Flooding Event

An unusually moist stationary weather pattern from 9-16 September 2013 led to unprecedented rainfall and historic flooding throughout Colorado, especially across the northern Front Range and northeastern plains. In Boulder, the 1-day, 2-day, and 7-day total rainfall records were broken with 230.6 mm (9.08 in.), 292.6 mm (11.52 in.), and 429.3 mm (16.9 in.), respectively (Lukas 2013). This extreme precipitation event led to widespread economic and societal impacts. Multiple roads were damaged or completely wiped out, leaving many towns isolated without power or drinking water (Young 2014). Following the floods, air and ground rescue efforts began delivering supplies and evacuating stranded residents and their pets. Flood waters caused severe damage to property and infrastructure estimated to incur economic costs of over $2 billion (EQECAT 2014) and resulted in nine deaths.

1.1.1 Synoptic Pattern

Four historic floods of interest for comparison with the 2013 event are: the Big Thompson Canyon Flood of 1976 (Caracena et al. 1979; Maddox et al. 1978) and the Fort Collins Flood of 1997 (Grigg et al. 1999; Petersen et al. 1999), two historic Colorado floods; the Rapid City, SD Flood of 1972 (Maddox et al. 1978); and the Madison County, VA Flood of 1995 (Pontrelli et al. 1999). These events all produced extreme amounts of rainfall leading to millions of dollars in damages and many injuries and fatalities (Table 1.1). The details of each flood event are different, but the overall large-scale patterns are the same: a negatively tilted 500 hPa ridge with an embedded northward-moving short-wave trough west of the ridge (Figure 1.3).

Table 1.1: Description of selected historic floods

	Storm Description	**Precipitation**	**Impact**	**References**
Big Thompson Flood – 31 July 1976	Relatively stationary band of thunderstorms	Over 300 mm of rain in 4 hours	100+ deaths $35.5 million in damages	Caracena et al. 1979; Maddox et al. 1978
Fort Collins, CO Flood – 28 July 1997	Quasi-stationary storm system	Over 250 mm of rain in 6 hours	5 fatalities, many injured >$200 million in damage to City $100 million in damage to CSU campus	Grigg et al. 1999; Petersen et al. 1999
Rapid City, SD Flood – 9 June 1972	Narrow band of convection	380 mm of rain	236 fatalities >$100 million in damages	Maddox et al. 1978
Madison County, VA Flood – 27 June 1995	Two consecutive mesoscale convective systems	Over 600 mm	3 fatalities >$200 million in damages	Pontrelli et al. 1999

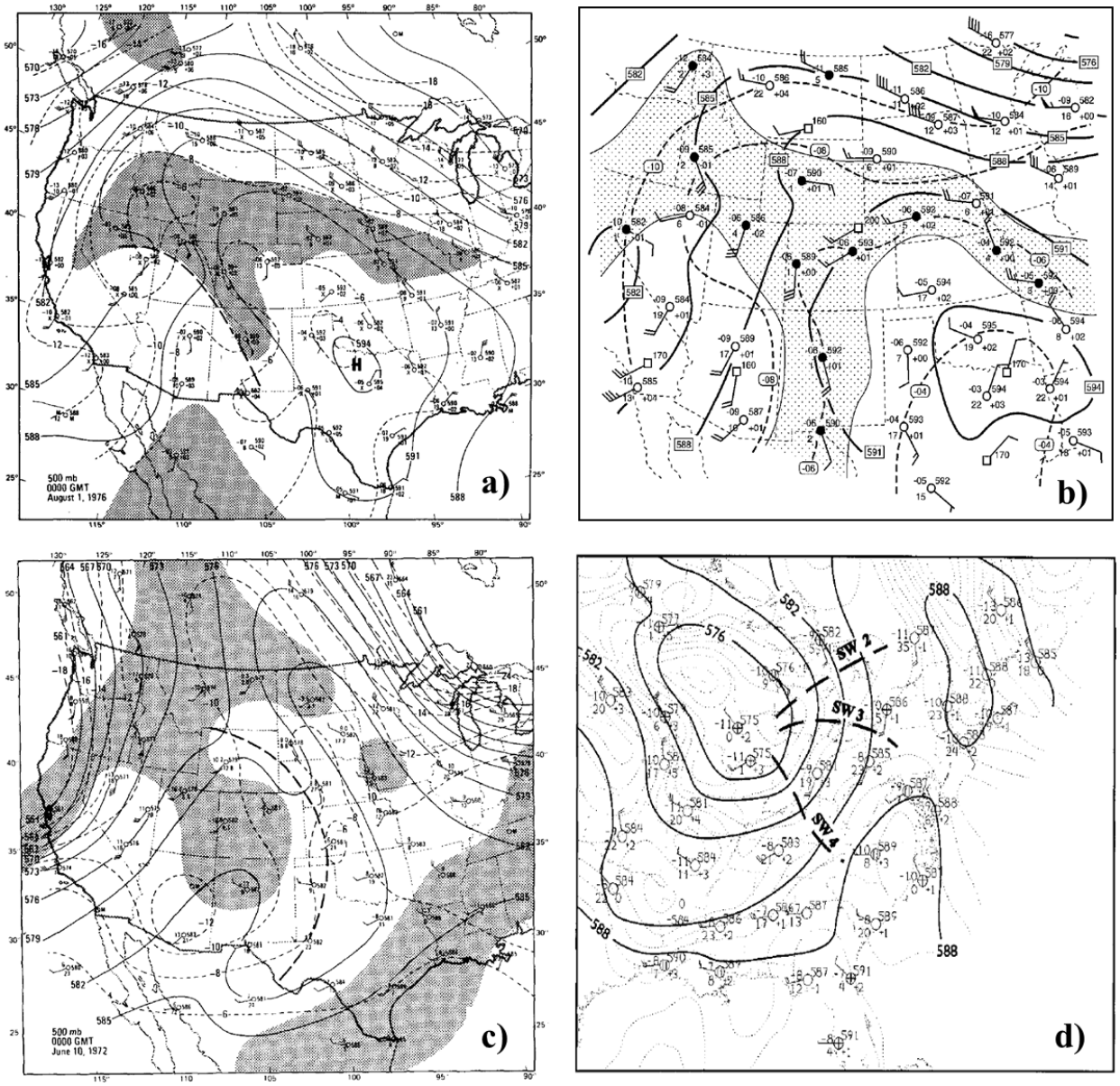

Figure 1.3: 500 hPa analysis for historic extreme precipitation and flooding events.
For 0000 UTC on (a) 1 August 1976 during the Big Thompson storm (from Maddox et al. 1978), (b) 29 July 1997 during the Fort Collins flood (from Petersen et al. 1999), (c) 10 June 1972 for the Rapid City, SD flood (from Maddox et al. 1978), and (d) 28 June 1995 for the Madison county, VA flood (from Pontrelli et al. 1999).

The 2013 event studied here has similarities to past historic floods, especially in the large-scale synoptic setup. “When a portion of the 500 mb short wave breaks into, or cuts off within, the long-wave ridge, the situation is especially dangerous if significant moisture and

instability are present" (Maddox et al. 1980). During the September 2013 event, the short-wave trough embedded within the ridge subsequently cut-off from the mean flow and remained relatively stationary over Nevada and Utah (Figure 1.4a,b). The upper-level ridge acted to block the progress of weather systems that could have caused the movement of the cut-off low, leading to a stagnant weather pattern that persisted for more than a week. The slow-moving (at times stationary) cut-off low was responsible for air parcel trajectories originating from over the Gulf of Mexico in the lower troposphere and from the East Pacific (off the western coast of Mexico) in the upper troposphere (Figure 1.5), leading to extremely high precipitable water values. The precipitable water (PW) values at Denver broke daily records for many days, reaching amounts as high as 35 mm (1.38 in.; Figure 1.6). This moisture content is extremely rare for September and more often seen during the monsoon season (July-August) (McKee and Doesken 1997). Although rare for this time of year, the deep layer moisture and PW values of over 25 mm during this event were similar to the historic floods described above, which occurred during the typical monsoon season.

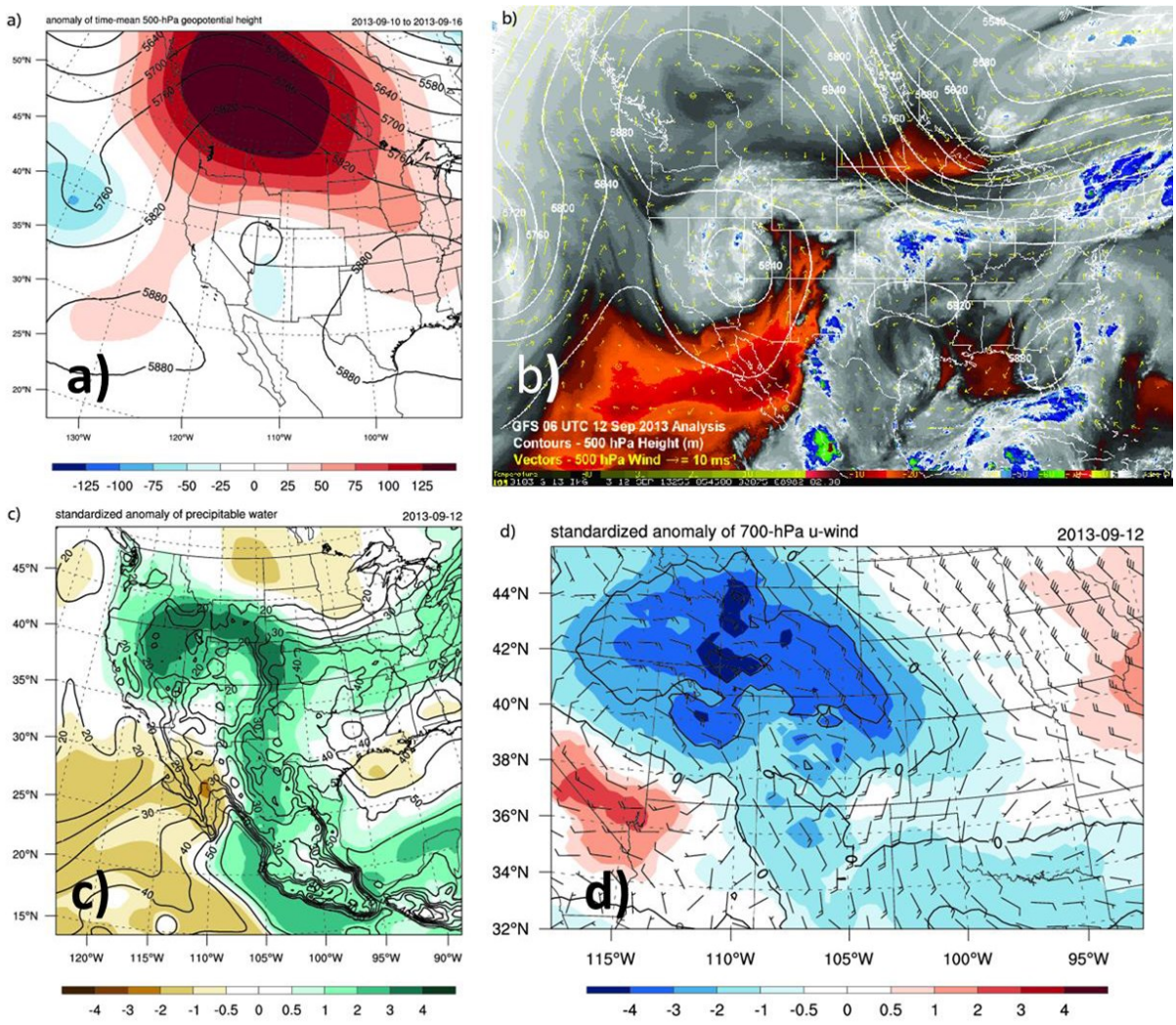

Figure 1.4: Synoptic overview of September 2013 Colorado extreme precipitation event (a) time-mean 500 hPa geopotential height (m; black contours at 60 m intervals) and anomaly (m; color), (b) GOES-13 water vapor overlayed with 500 hPa geopotential height contours (m; white contours at 40 m intervals) and wind vectors (m/s) at 0600 UTC 12 September 2013, (c) column-integrated precipitable water (mm; black contours at 5 mm intervals) and standardized anomaly (units of standard deviation; color) for 12 September 2013, and (d) 700 hPa zonal winds (m/s; black contours at 5 m/s intervals for values ≤ 0), standardized anomaly (color), and wind barbs (kts) for 12 September 2013. From Gochis et al. (2014, manuscript submitted to BAMS.)

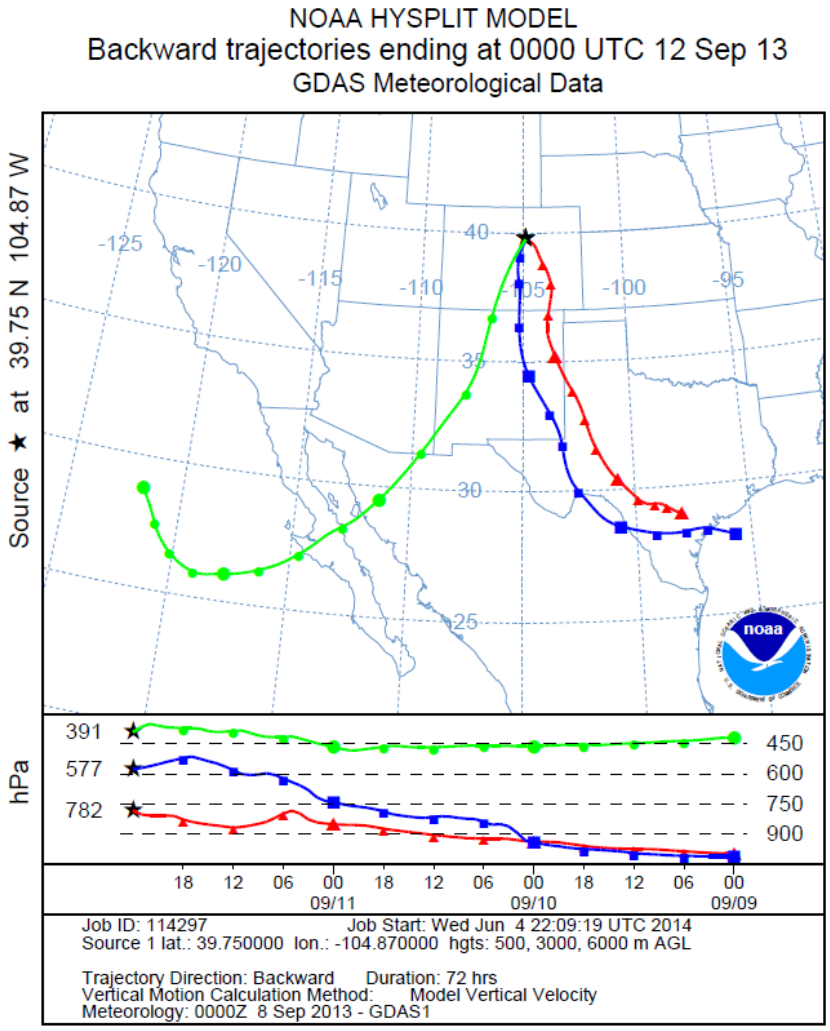

Figure 1.5: HYSPLIT model backward trajectory ending at 0000 UTC 12 September 2013. 72-hour backward trajectories for three height levels (500, 3000, 6000 m AGL) plotted in hPa from the NOAA HYSPLIT model (Draxler and Rolph 2013). NCEP's Global Data Assimilation System (GDAS) was used as the meteorological input for the trajectories.

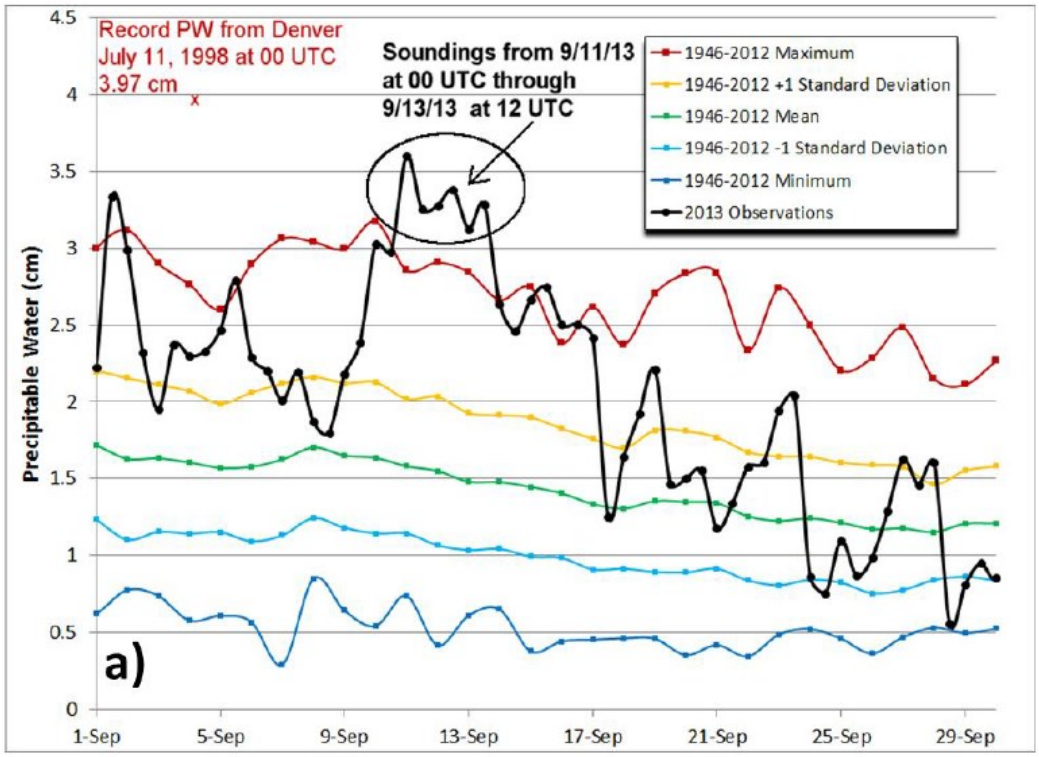

Figure 1.6: Precipitable water (cm) from the surface to 300 hPa for September 2013 observations and the 1946-2012 maximum, minimum, mean, and standard deviations (from Gochis et al. 2014, manuscript submitted to BAMS).

The September 2013 case did have some differences from the typical Type I western flash flood event. The Type I flash floods described in Maddox et al. (1980) tend to be associated with short-lived, localized thunderstorms that produce extreme precipitation during the afternoon-evening hours (e.g. Big Thompson flood (Caracena et al. 1979) and Fort Collins 1997 flood (Grigg et al. 1999)). The September 2013 event produced widespread precipitation along the Front Range and eastern plains of Colorado over several days, as well as over New Mexico and western Kansas. This study will focus on the precipitation over the northern Colorado Front Range near the city of Boulder (see Figure 1.1 for location reference) from 11-12 September 2013, when rainfall rates were the highest (Figure 1.7).

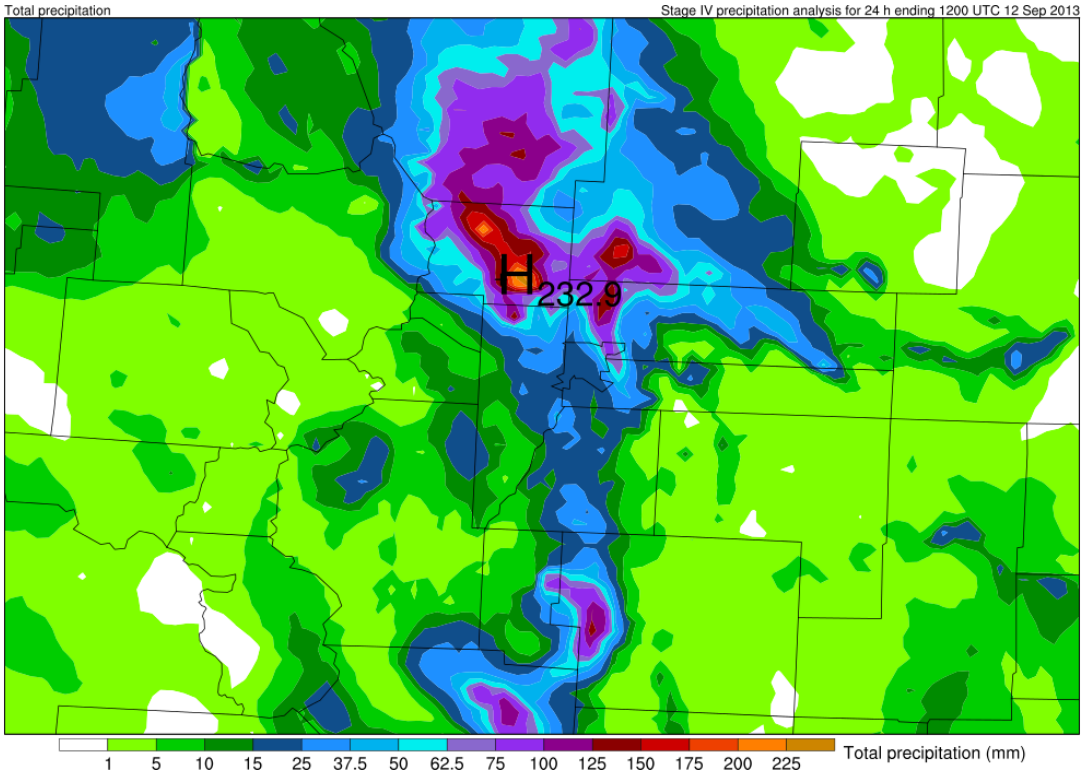

Figure 1.7: NCEP Stage IV 24 hr accumulated precipitation for north-central Colorado. 24 hr accumulated precipitation (mm) valid at 1200 UTC 12 September for the NCEP Stage IV analysis (observations). High precipitation value is 232.9 mm in Boulder County.

The initial lifting mechanism in the region was a baroclinic zone (cold front) that stretched from eastern Canada to eastern Colorado (Bolinger 2013; Gochis et al. 2014) associated with an upper-level trough in eastern Canada (Figure 1.4b). The position of the cut-off low west of Colorado and the subtropical high pressure system located over the south-southeastern U.S. helped to transport warm, moist air northward and westward into the Colorado Front Range (Figure 1.4d) (Gochis et al. 2014). Due to the dramatic change in topography from eastern to western Colorado (Figure 1.1), orographic lift was also able to initiate and maintain convection throughout the precipitation event. Orographic lift was a common trigger for convection in the Big Thompson, Fort Collins, Rapid City, and Madison County floods; for some events the location of the convection was determined by the local terrain.

1.2 11-12 September 2013 – Heaviest Precipitation

Heavy precipitation occurred throughout the entire event, with only brief breaks in the storm, but on the evening of 11 September into the 12th (0400-0700 UTC), the city of Boulder experienced its most extreme hourly rainfall rates (>40 mm/hr or >1.6 in./hr; Figure 1.7 and Figure 1.8). This time period was also associated with colder cloud tops and lightning, characteristics of deep convection versus more stratiform precipitation (Figure 1.8).

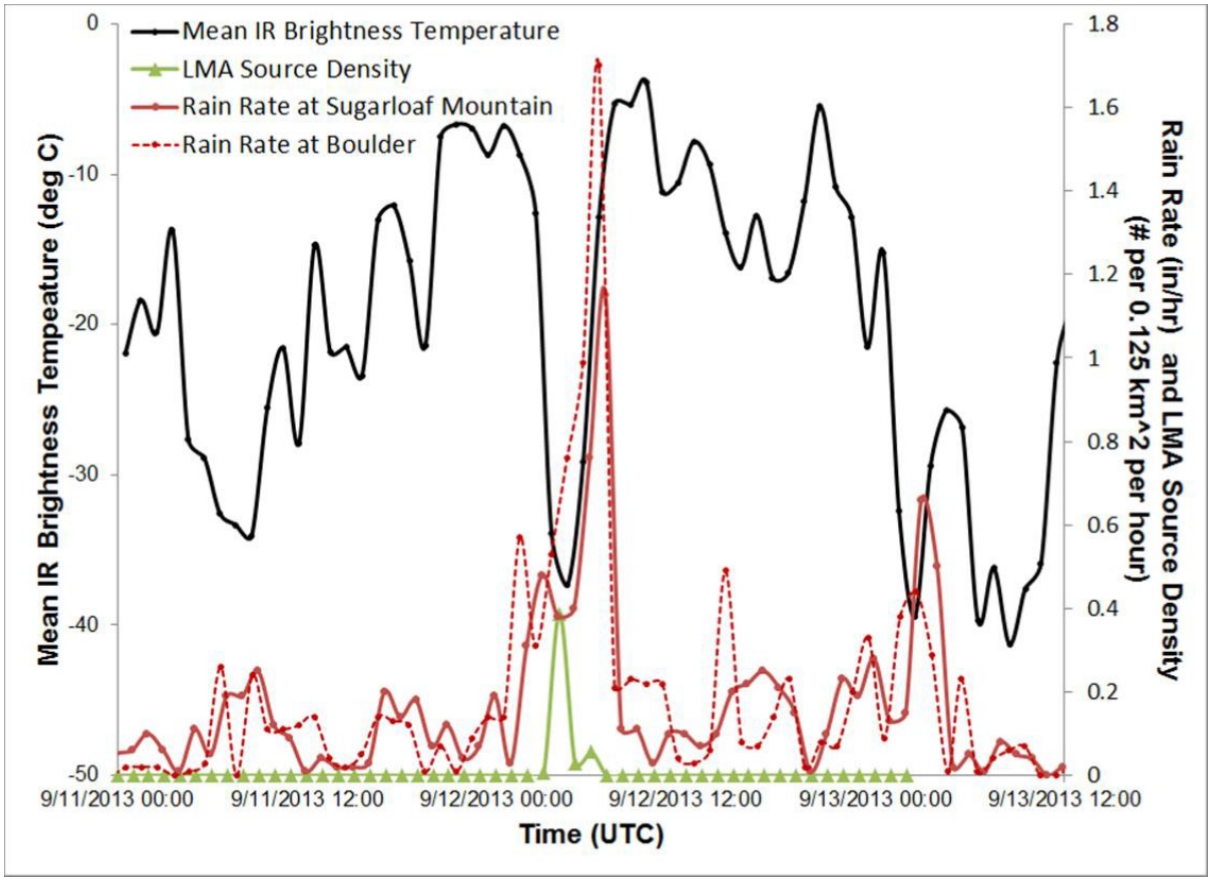

Figure 1.8: Precipitation and rain gauge data for Boulder for 9-13 September (from Gochis et al. 2014, manuscript submitted to BAMS).
Mean IR brightness temperatures (°C; solid black), lightning mapping array (LMA) source density (# km^{-2} hr^{-1}; green), and rain rate (in) for locations at Sugarloaf Mountain (solid red) and Boulder (dashed red), CO.

The ingredients needed to produce heavy precipitation are those that can increase both the time-averaged rain rate ($\bar{R}$) and an event's duration (D), described through $P = \bar{R}D$, where P is the total precipitation (Doswell et al. 1996). Simply stated, "the heaviest precipitation occurs where the rainfall rate is the highest for the longest time" (Doswell et al. 1996). To produce a high rainfall rate, high moisture content, upward motion, and high precipitation efficiencies are required. Precipitation efficiency describes the amount of condensate falling as rain compared to the amount of condensate available within the cloud. Rain evaporation, entrainment of dry air, and advection of condensate aloft by strong updrafts will act to reduce precipitation efficiency. Tropical sounding features such as high freezing level, low cloud base, weak vertical wind shear, and a deep layer of high moisture content are generally associated with high precipitation efficiency (Maddox et al. 1977; Davis 2001). The duration of the event is determined by the system speed, size and organization.

The slow-moving large-scale system provided the high moisture content and south-southeasterly winds towards the Front Range resulting in widespread, almost continuous precipitation from 9-16 September. The precipitation system was very large, covering not just Colorado, but many neighboring states with clouds (Figure 1.4b) and precipitation. Because of the weak vertical wind shear, the storms themselves were not very organized, i.e. there were no lines or individual clusters of cells similar to a squall line, mesoscale convective system (MCS), or supercells. Flash flood-producing storm systems may be convective or nonconvective, where the latter are not as deep (i.e. cloud tops may not be very cold) and can produce heavy rain through orographically forced updrafts (Doswell et al. 1996). The September event studied here had embedded convective precipitation within a widespread nonconvective system (Figure 1.9). Figure 1.9b covers a region focused over Boulder county and southern Larimer County and

demonstrates the direction of the radar reflectivity echoes was from east to west during the time of heaviest precipitation (denoted by dotted box).

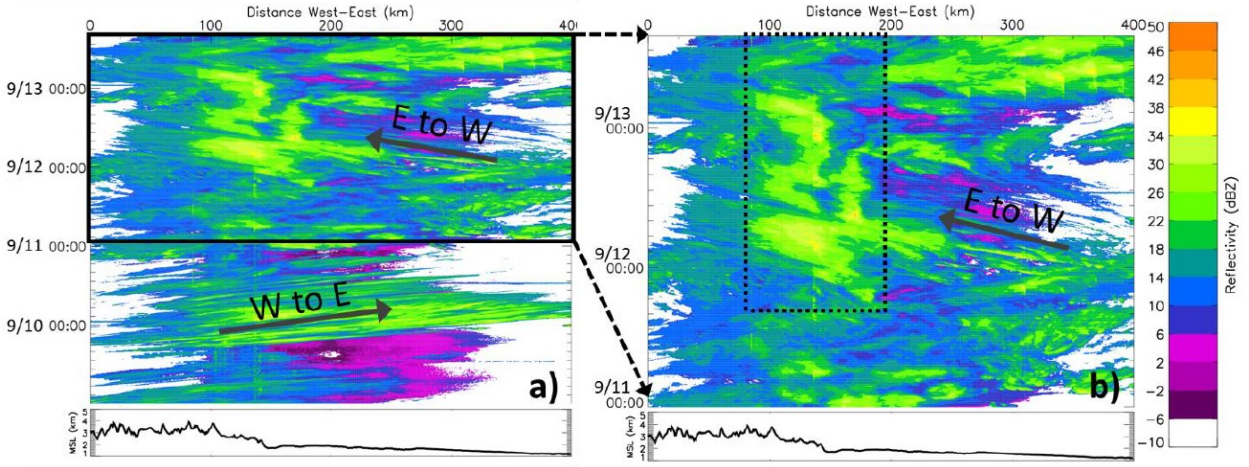

Figure 1.9: Hovmöller plots of radar reflectivity from Gochis et al. 2014 (manuscript submitted to BAMS).
Radar reflectivity (dBZ) from the Denver NEXRAD (KFTG) corresponding to an area focusing over Denver, Boulder County and southern Larimer County for (a) 09-13 September 2013 and (b) 11-13 September 2013. The dotted box in b) denotes the period of heavy precipitation and flooding. The arrows denote the general direction of the radar echoes ('E to W' means east to west, and vice versa). The mean longitudinal topography is included at the bottom of the figure (higher elevation to the west).

From 0000 UTC 11 September to 1200 UTC 13 September, six consecutive soundings measuring precipitable water broke the 1946-2012 maximum record for daily observations in Denver (Figure 1.6). An atmospheric sounding taken on 0000 UTC 12 September from Denver shows the atmosphere was close to saturation, with a very high tropopause height (~150 hPa), weak vertical wind shear, and high freezing level (~600 hPa) (Figure 1.10). The sounding in Figure 1.10 is representative of the environment from 9-16 September, having characteristics more commonly found in a tropical environment (favored for heavy rainfall) than that of a midlatitude, mountainous region. Due to the high amounts of moisture, the lifting condensation level (LCL) and level of free convection (LFC) were close to each other with cloud base very

low to the ground (~844 hPa). Thus, orographic lifting would be expected to provide sufficient lift to get parcels to their condensation level.

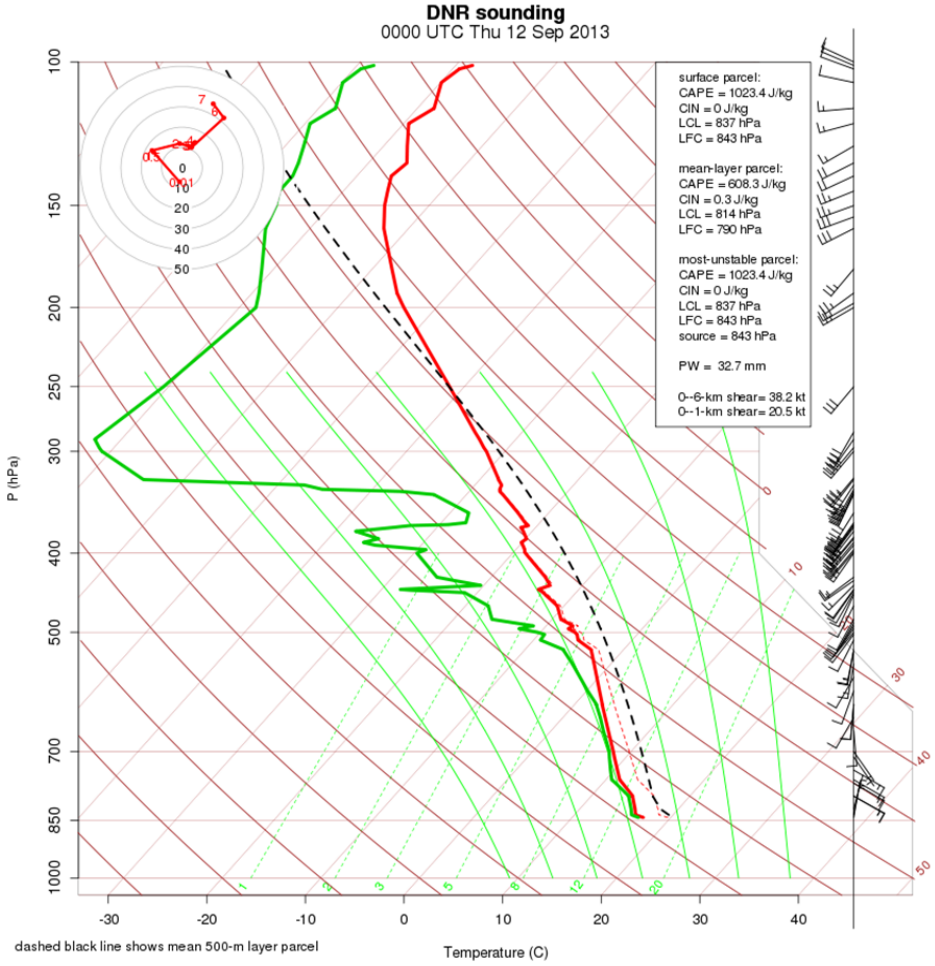

Figure 1.10: Atmospheric profile for 0000 UTC 12 September at Denver (DNR).

The environment during this event had low values (~1000 J/kg or less) of convective available potential energy (CAPE) with little to no convective inhibition (CIN) and was generally moist adiabatic to neutral (Figure 1.10). Low to moderate CAPE is favored for more efficiently producing rainfall than environments with the potential for stronger updrafts (Davis 2001). This is because stronger updrafts would tend to advect moisture and condensate aloft, which acts to decrease the precipitation efficiency and enhance mixed-phase and ice processes,

resulting in the production of high-density graupel and hail. Observations of hydrometeors from the Denver (KFTG) radar from 0200-0600 UTC 12 September show ice species (aggregates, wet snow, low-density graupel) were available in the storm near the freezing level (Figure 1.11a). Ice species falling through the 0°C level could melt and become small raindrops, which could then fall through a relatively deep layer of liquid cloud and grow through collision-coalescence (Gochis et al. 2014). Flash floods tend to be associated with 3-4 km thick warm cloud layers (Chappell 1993); the warm-cloud layer in this case was approx. 2.5 km deep, which is unusually thick for Colorado. The combination of a deep layer of warm, cloudy air to promote warm rain processes, not-excessively-strong updrafts to increase residence time of a parcel within the warm cloud layer, and a highly saturated environment inhibiting both high rain evaporation and entrainment of dry air resulted in high precipitation efficiencies during this event as seen by the amount of rainfall reaching the surface (Figure 1.7).

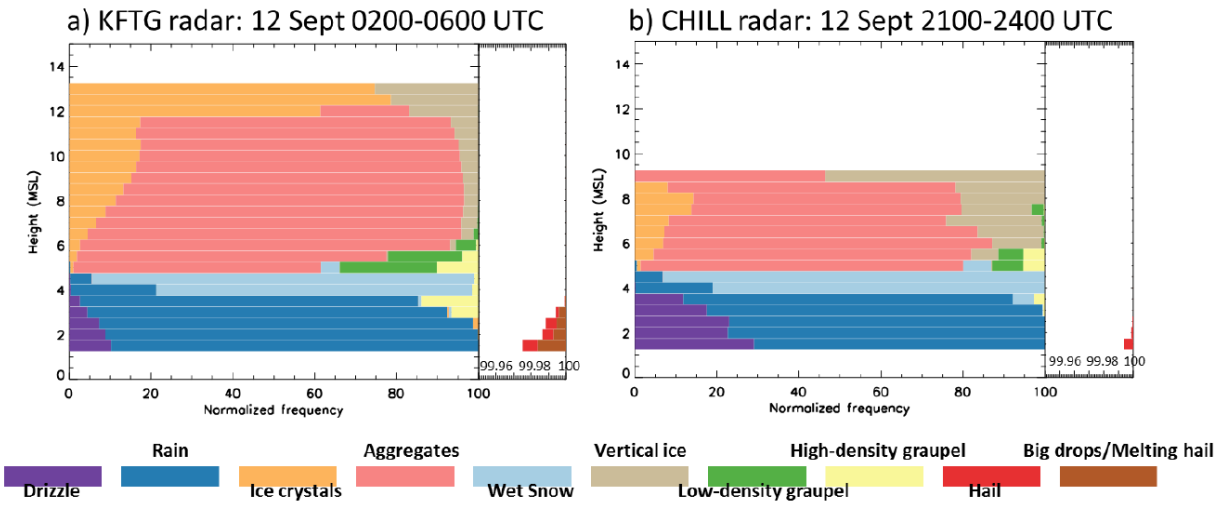

Figure 1.11: Normalized frequency of occurrence for each hydrometeor type with height (from Gochis et al. 2014, manuscript submitted to BAMS).
(a) KFTG radar for 0200-0600 UTC 12 September and (b) CHILL radar for 2100-0600 UTC 12 September.

1.2.1 Mesoscale Features

Amid this region of heaviest rainfall, a cyclonic mesoscale circulation developed north of Denver, CO. Observations of radial velocity from the Denver (KFTG) radar show a rotational signature from 0400-0700 UTC on 12 September (Figure 1.12). The mesoscale vortex (mesovortex) traveled northwestward towards the city of Boulder. The rotation was associated with enhanced southeasterly (upslope) flow over Boulder County. East of Boulder County, the Platteville (PLT) wind profiler (see Figure 1.1 for reference location) observed this enhanced low-level flow. The PLT profiler shows a low-level jet (LLJ) with maximum speeds of 30 kts between 0400 UTC and 0700 UTC 12 September (Figure 1.13). This time period was also associated with bands of localized deep convection (> 40 dBZ echoes) traveling east to west towards higher elevations (Figure 1.9 and Figure 1.14). These observations suggest a connection between the high rain rates and the mesovortex, both observed to occur over Boulder between 0400-0700 UTC.

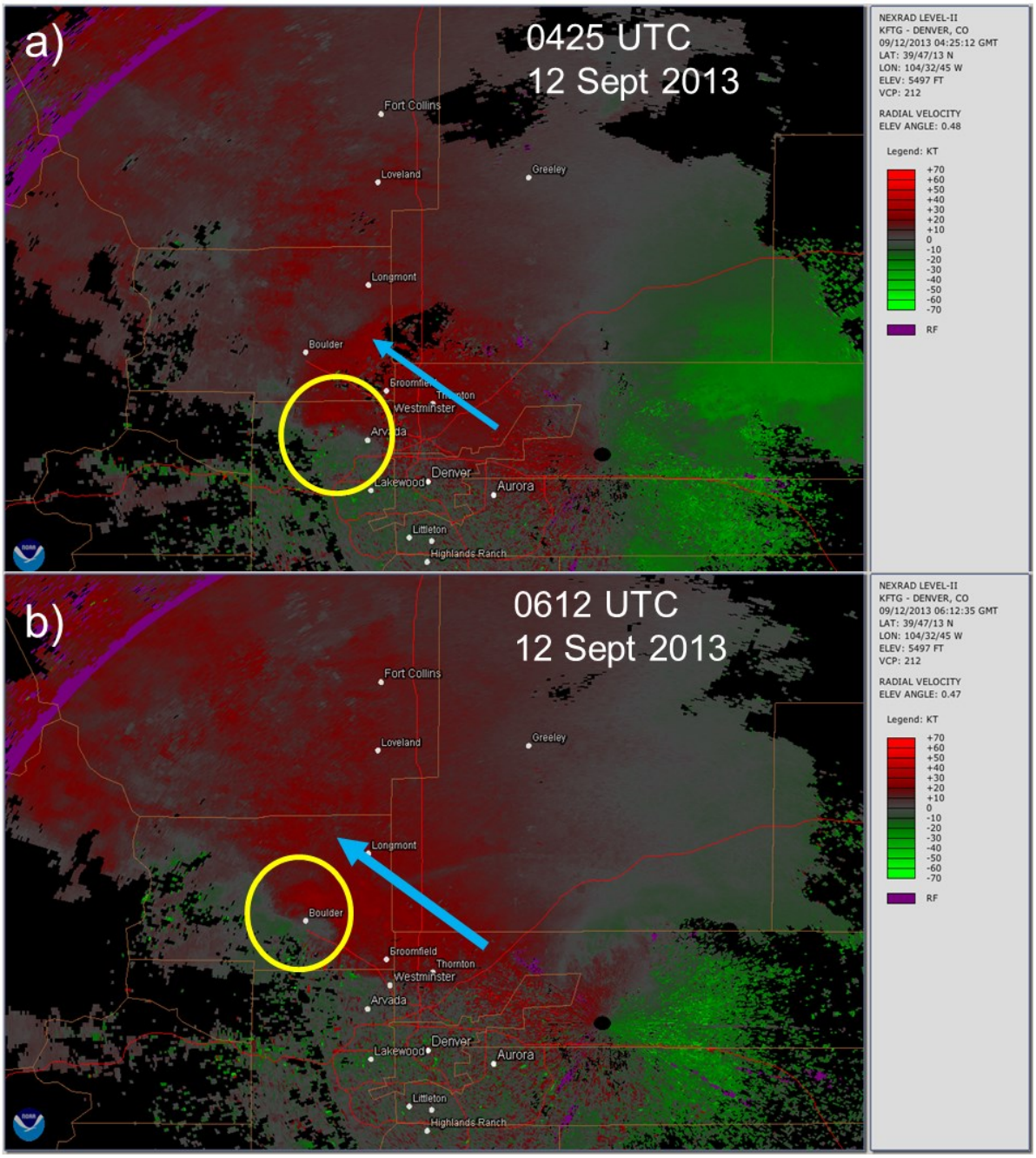

Figure 1.12: Observed radial velocity from the Denver (KFTG) radar for 12 September 2013. Times shown are (a) 0425 UTC and (b) 0612 UTC. The radar's elevation angle is 0.5°. The yellow circle denotes the location of the mesoscale vortex and the blue arrow represents upslope flow (thickness illustrates enhancement at 0612 UTC). Enhanced upslope flow shown by higher values of outbound radial velocity (red). Adapted from images courtesy of R. Schumacher.

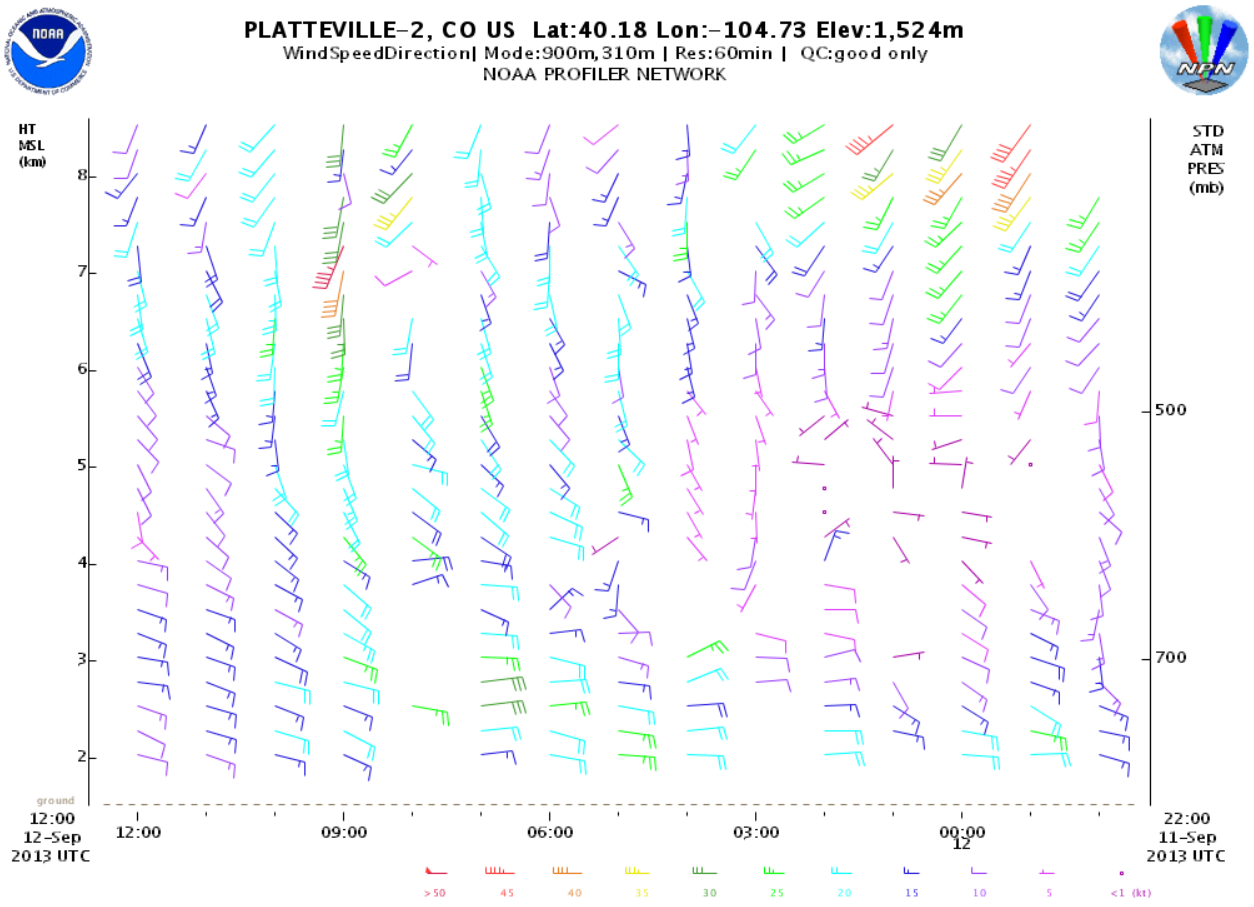

Figure 1.13: Platteville (PLT), CO wind profiler data from 2200 UTC 11 September 2013 to 1200 UTC 12 September 2013.
Time increases from right to left. Vertical axis is height (MSL in km). Wind speeds are color coded (kts). Location of PLT profiler can be found in Figure 1.1. Figure courtesy of R. Schumacher.

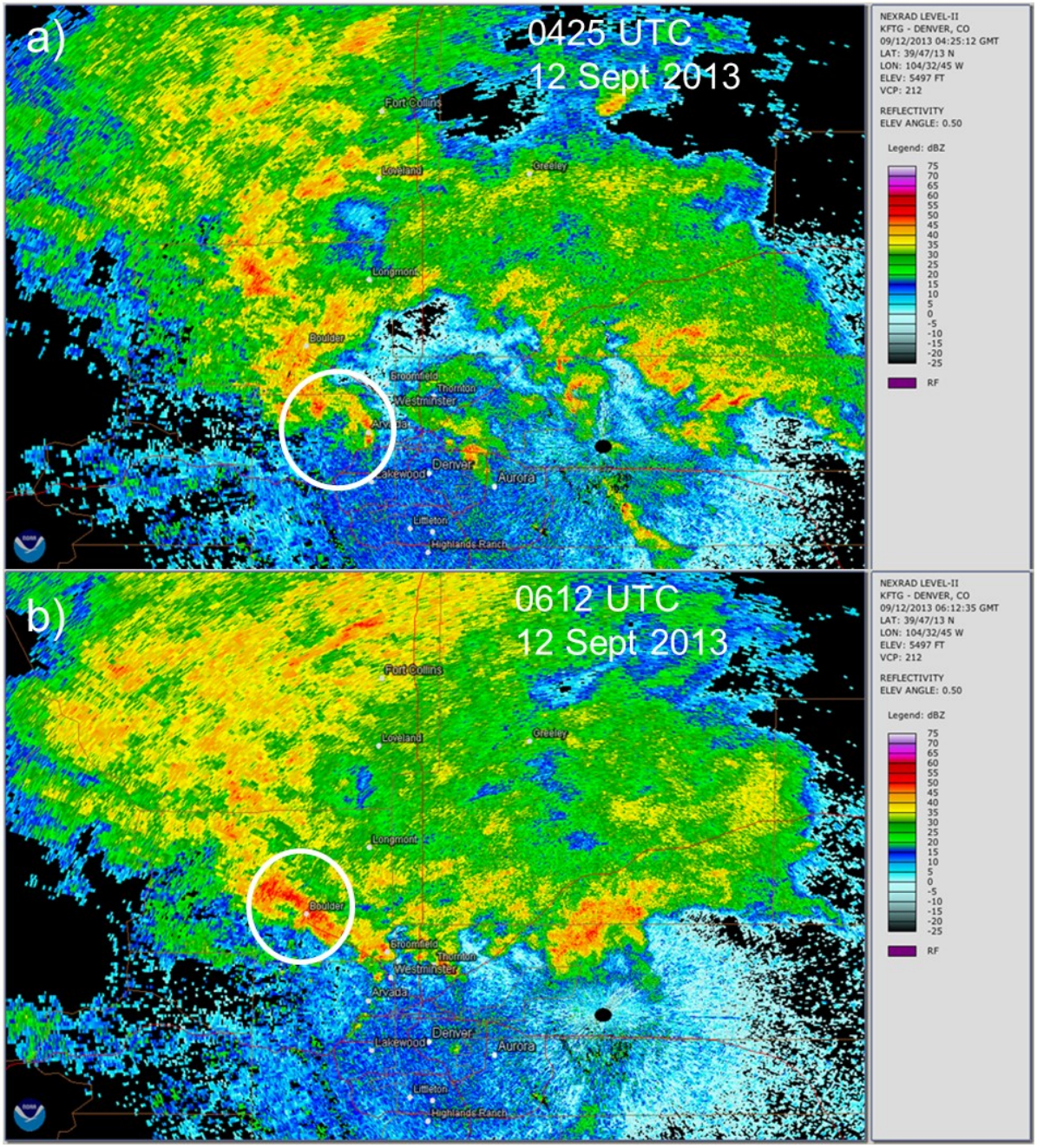

Figure 1.14: Observed radial reflectivity from the Denver (KFTG) radar for 12 September 2013. Times shown are (a) 0425 UTC and (b) 0612 UTC. The radar's elevation angle is 0.5°. The white circle denotes the location of the mesoscale vortex, same as those in Figure 1.12. Enhanced convection shown by higher reflectivity values. Adapted from images courtesy of R. Schumacher.

Surface observations at 0300 UTC show some of the rotation associated with the mesovortex (Figure 1.15). At this time, the area over which the rotation resided was overcast with saturated conditions and light winds (~5 m/s). The cyclonic circulation originated in an area known for the development of an orographically-induced circulation, i.e. the Denver Cyclone (Szoke et al. 1984; Wilczak and Glendening 1988; Crook et al. 1990; Wilczak and Christian 1990; Szoke 1991). The possible mechanism for the development of this mesoscale feature will be further explored in Section 1.3.

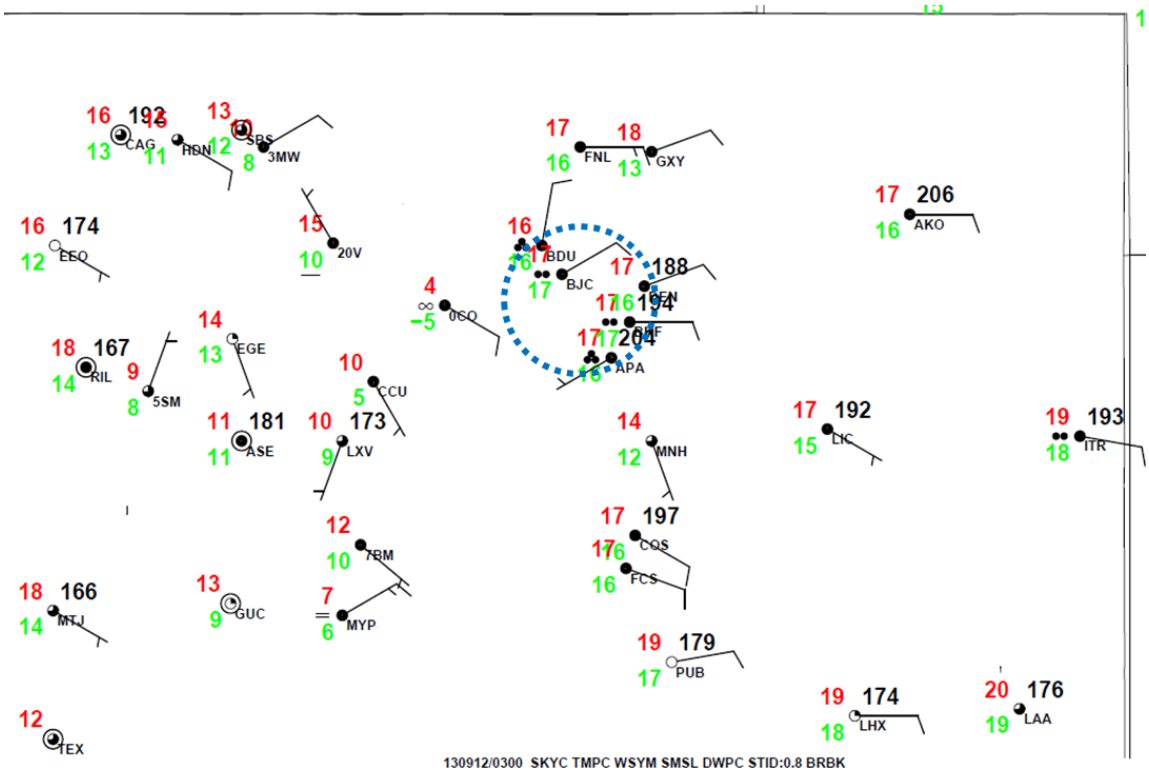

Figure 1.15: Surface observations for 0300 UTC 12 September over a large portion of Colorado. Surface stations denoting temperature (°C; red), dewpoint temperature (°C; green), wind barbs (kts), mean sea level pressure with first 9 or 10 omitted (hPa; black), and sky cover (filled in circle means overcast). Dotted blue circle denotes the area of rotation. Station names for locations of interest are: BDU = Boulder, DEN = Denver, and FNL = Fort Collins-Loveland. Figure courtesy of Russ Schumacher.

1.3 Possible Mechanisms for Mesoscale Vortex Development

The mechanisms that will be explored in this study to determine the origin of the cyclonic circulation observed during the September 2013 extreme precipitation and flooding event will be 1) terrain blocking/lee vortex formation and 2) vorticity generation via vertical gradients in latent heating. Due to the location where the cyclone first developed, a plausible idea would be for the mesoscale vortex to have developed in a similar manner as the Denver Cyclone. However, the immense amount of precipitation falling over such a widespread area would be expected to release a large amount of latent heat through microphysical phase changes (i.e. condensation, deposition, freezing) and this heating could also induce rotational flow, as explained below.

1.3.1 Lee Vortex Formation (Denver Cyclone)

1.3.1.1 Description

The Denver Cyclone is a cyclonic mesoscale vortex or gyre that forms in the lee of the east-west oriented ridge, the Palmer Divide, near Denver in northeastern Colorado. A related phenomenon known as the Denver Convergence and Vorticity Zone (DCVZ, Szoke et al. 1984) is characterized by a region of converging surface winds often located on the eastern flank of the circulation. These mesoscale features are sometimes associated with generating severe weather near Denver and the eastern plains, including hail and flooding (Blanchard and Howard 1986) and tornadoes (Szoke et al. 1984; Wakimoto and Wilson 1989). A typical diameter for the Denver Cyclone is about 100 km and its lifetime is on the order of 10 hours (Wilczak and Glendening 1988; Crook et al. 1990). Observational studies have shown the circulation can remain relatively stationary (Wilczak and Glendening 1988; Wilczak and Christian 1990) or travel northward (Crook et al. 1990; Szoke 1991). The low-level flow that is observed during a

Denver Cyclone or DCVZ is usually south-southeasterly (Szoke et al. 1984; Wilczak and Glendening 1988; Crook et al. 1990; Wilczak and Christian 1990; Szoke 1991). Wilczak and Christian (1990) found the vortex center of their case study gyre to be associated with low-level convergence during the night, but divergence in the presence of significant daytime heating. They also found the vortex had a "warm-core", which can sometimes lead to the observance of a cloud-free "eye" in satellite imagery (Szoke 1991).

1.3.1.2 Mechanisms for Vortex Development

Studies suggest the Denver Cyclone forms from low-level flow interacting with the local topography. As the southerly to southeasterly flow encounters an obstacle (the Palmer Divide) it can either go over it or be blocked and have to go around it. The Froude number, Fr, is used to determine if a flow will be blocked,

$$\mathrm{Fr} = \frac{\mathrm{U}}{\mathrm{NH}}, \qquad (1)$$

where U is the mean wind speed, N is the Brunt−Väisäla frequency (a measure of stability), and H is the height of the obstacle. In order to have at least some of the flow blocked by the terrain, Fr must be less than one (e.g. large N and weak U). Low Fr environments have been found to generate cyclonic circulation in the lee of the Palmer Divide through baroclinically generated horizontal vorticity as isentropes bend upward/downward with the flow over the obstacle (Smolarkiewicz and Rotunno 1989; Crook et al. 1990). Crook et al. (1990) found that generation of surface vorticity through wave breaking (caused by isentropes turning over) and a leftward deflection induced through blocking by the Front Range could contribute as additional mechanisms to the formation of the circulation. Southerly flow would be blocked by the Palmer Divide, while southeasterly flow, having a component perpendicular to the Front Range, could be more easily blocked without having such strict stability requirements (Crook et al. 1990).

Although low Fr seems important for the initial generation of the circulation, the Denver Cyclone has been observed in well-mixed environments with larger Fr (Wilczak and Glendening 1988) and during day and night (Wilczak and Christian 1990). Thus, terrain blocking or lee vortex formation may not be the only mechanism involved in its formation (Szoke 1991; Davis 1997).

1.3.2 Vorticity Generation via Latent Heating

1.3.2.1 Description

Latent heat represents the energy released or absorbed by a system or substance (e.g. water) as it changes phases without changing its temperature, and is expressed in units of J kg^{-1}. Phase changes such as evaporation, melting, and sublimation will absorb energy from the environment, while condensation, freezing, and deposition will release latent heat. For example, rain evaporation would absorb energy from its environment and lead to cooling of the air (latent cooling). Similarly, condensation of cloud water would release energy and lead to heating of the atmosphere (latent heating).

The latent heating profile within a storm can vary between the convective and stratiform precipitation regions. Studies have found that heating profiles characteristic to convective areas within an MCS (Johnson 1986; Houze 1989) and squall line (Gallus and Johnson 1991) tend to have a peak in latent heating in the mid-troposphere (Figure 1.16), where condensation is maximized. In the stratiform area, the peak in latent heating tends to be located aloft, where the anvil extends away from the core updraft within the convective area (Figure 1.16). A cooling peak in the lower troposphere is also a characteristic of the stratiform heating profile, mainly caused by melting and evaporation as hydrometeors fall from the stratiform region (Figure 1.17).

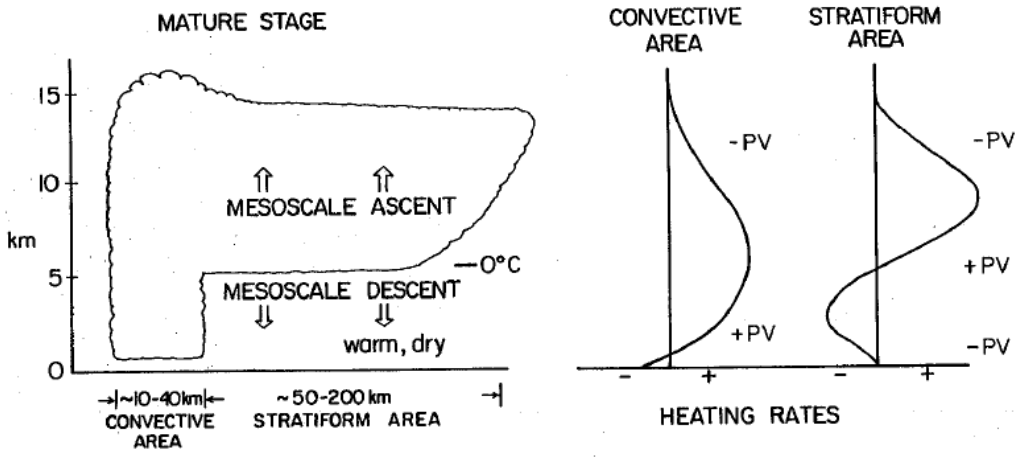

Figure 1.16: Schematic of latent heating profiles for mature MCS from Johnson (1986).

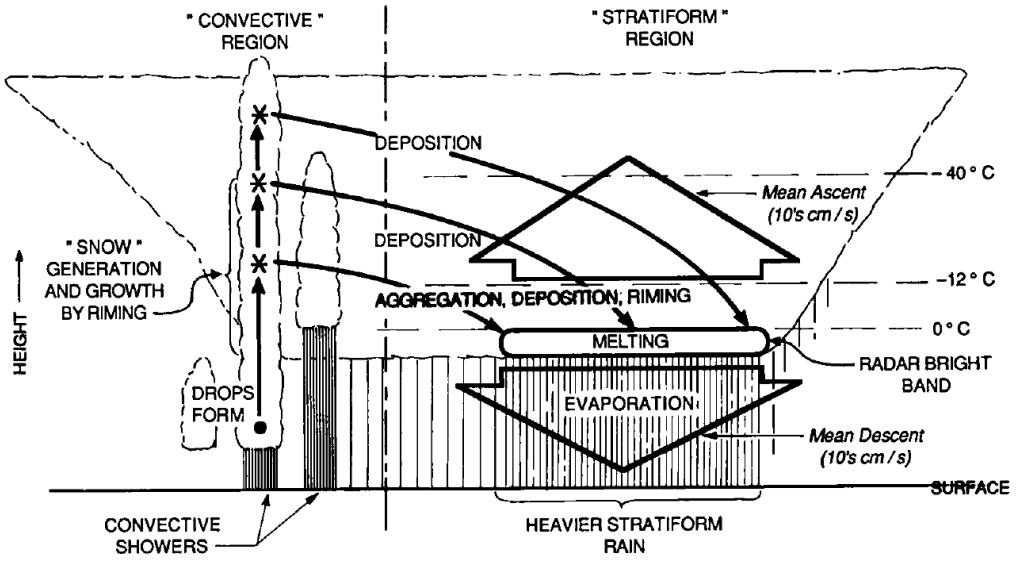

Figure 1.17: Schematic of hydrometeor processes within an MCS from Houze (1989).

1.3.2.2 Mechanism for Vortex Development

The release of energy as latent heating is important to additional growth of a storm during convection because it can increase the buoyancy of air parcels leading to increased vertical velocity and low-level convergence (Danard 1964; Houze 1984), which can help vertically transport warm, moist air from the surface to be condensed at mid- to upper-levels. A study by

Raymond and Jiang (1990) proposed that MCS could help maintain themselves through interactions between the environmental wind shear and potential vorticity (PV) anomalies generated by the release of latent heat.

As previously mentioned, latent heating can cause buoyancy differences, which can lead to upward motions transporting mass across isentropic surfaces. PV is conserved between two isentropic surfaces, so an updraft will act to reduce the mass below the source of heating, causing PV to increase (Haynes and McIntyre 1987; Raymond and Jiang 1990). Thus, a positive PV anomaly will be induced below the diabatic warming, forming a cyclonic circulation around the anomaly (Figure 1.18).

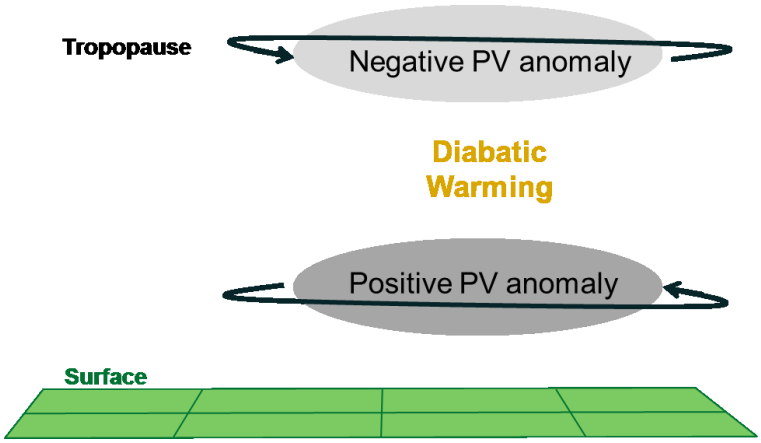

Figure 1.18: Structure of PV anomalies due to convection adapted from Raymond and Jiang (1990).

Through this mechanism, a positive PV anomaly would be found below the mid-tropospheric peak in the stratiform heating profile and near the surface below the lower-tropospheric peak in the convective heating profile (Figure 1.16). This relationship can be described through Equation 2,

$$\frac{d(\mathrm{PV})}{dt} \approx (\zeta + f)\frac{d\dot{\theta}}{dz} \qquad (2)$$

where ζ is the relative vorticity, f is the Coriolis parameter, and $\dot{\theta}$ represents diabatic heating through latent heat release. Equation 2 shows that vertical gradients in latent heating cause the PV of an air parcel to not be conserved. This can lead to the development of mesoscale convective vortices (MCVs; Johnston 1981; Bartels and Maddox 1991; Bartels et al. 1997; Trier et al. 2000), which are generally associated with a mid-tropospheric positive PV anomaly that develops in the stratiform region of an MCS (Figure 1.16).

A positive PV anomaly will tend to deform the isentropic surfaces and bend them towards the anomaly as illustrated in Figure 1.19a. Low-level flow within a vertically sheared environment would then experience isentropic lift downshear of the anomaly and descent upshear. The cyclonic circulation induced from the positive PV anomaly will also have ascent associated with the northward moving winds as they glide up the isentropic surfaces that are sloped from south to north owing to the synoptic-scale baroclinity (Figure 1.19b). This ascent on the downshear side of the MCV can influence the initiation of convection on the next day, which can act to strengthen the PV anomaly through vortex stretching or generate a new MCV, thus extending its lifetime (Menard and Fritsch 1989; Bartels and Maddox 1991; Trier et al. 2000).

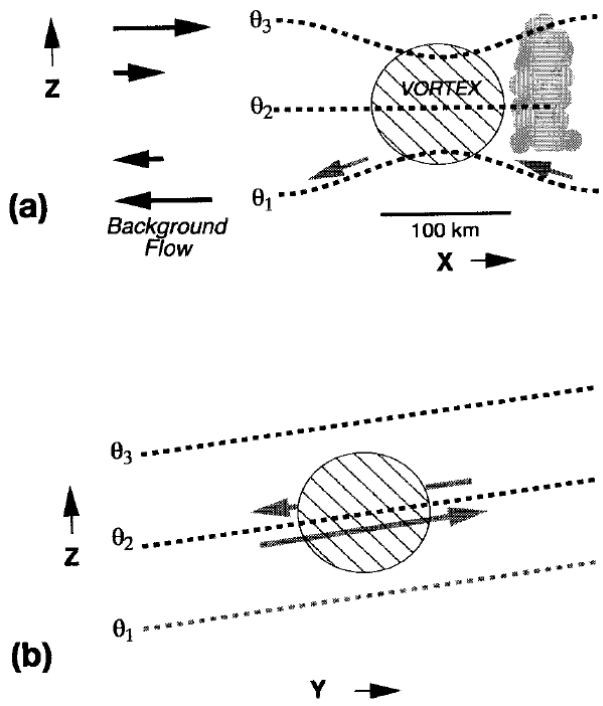

Figure 1.19: Diagram of isentropic lifting as low-level flow encounters a positive PV anomaly within ambient vertical wind shear (from Trier et al. 2000).
(a) Zonal cross-section of positive PV anomaly embedded in sheared flow within isentropic surfaces; upglide is located on the upwind side of the vortex. (b) Meridional cross-section of the vortex induced by the PV anomaly; upglide is associated with the northward moving winds.

For a mesoscale circulation to form near the surface, similar to the circulation investigated in this study, a profile with convective heating characteristics (similar to the convective area profile in Figure 1.16) or a profile where there is little or no evaporative cooling near the surface (Rogers and Fritsch 2001; Schumacher and Johnson 2008) would be favored. This would shift the maximum warming in Figure 1.18 downward from the mid-troposphere, allowing for a cyclonic circulation to form closer to the ground. Although the event studied here does not have the convective organization typical to that of the MCSs analyzed in previous studies (Johnson 1986; Houze 1984; Raymond and Jiang 1990), the widespread and persistent

precipitation observed does compare. Therefore, analogies can be made between MCS maintenance and the formation of the mesoscale vortex in this study.

1.4 Project Goals

This study aims to investigate the processes that led to the development of a mesoscale vortex observed from 00-06 UTC 12 September 2013 near the Denver/Boulder area in Colorado. The first goal of this project was to properly model the mesoscale vortex and use the simulation to understand the circulation's characteristics and its effect on the surrounding atmospheric flow, convection, and surface precipitation. Once a control simulation is properly established, the next goal is to understand whether this circulation was associated with lee vortex formation (mechanism responsible for the Denver Cyclone) or if it developed through the dynamic-thermodynamic feedbacks from the release of latent heat. Further analysis will then be performed to understand the role of latent heating to the mesovortex development and evolution, as well as the role of microphysical processes to latent heating within the model. The capability of numerical weather prediction (NWP) models to properly represent these microphysical processes can then have an effect on the forecasting of similar mesovortices during extreme precipitation and their feedbacks to convection, precipitation, and the local environment.

2. Methods

2.1 Model Description and Configuration

The Advanced Research Weather Research and Forecasting (ARW) model version 3.3.1 was used to simulate the heavy precipitation event explored in this study. ARW is a three-dimensional non-hydrostatic regional numerical weather prediction model (Skamarock et al. 2008). The model configuration is a two-way nested grid with three domains (Figure 2.1). The outer domain has a horizontal grid spacing (Δx) of 36 km, the inner domain has Δx = 12 km, and the innermost domain has Δx = 4km. The model contains 36 stretched vertical levels (higher resolution near the surface) and a 50-hPa model top. The time steps used are 144, 48, and 16 seconds for the 36 km, 12 km, and 4 km domains, respectively. Simulations are initialized at 0000 UTC 11 September 2013 and run for 60 hours, ending at 1200 UTC 13 September 2013.

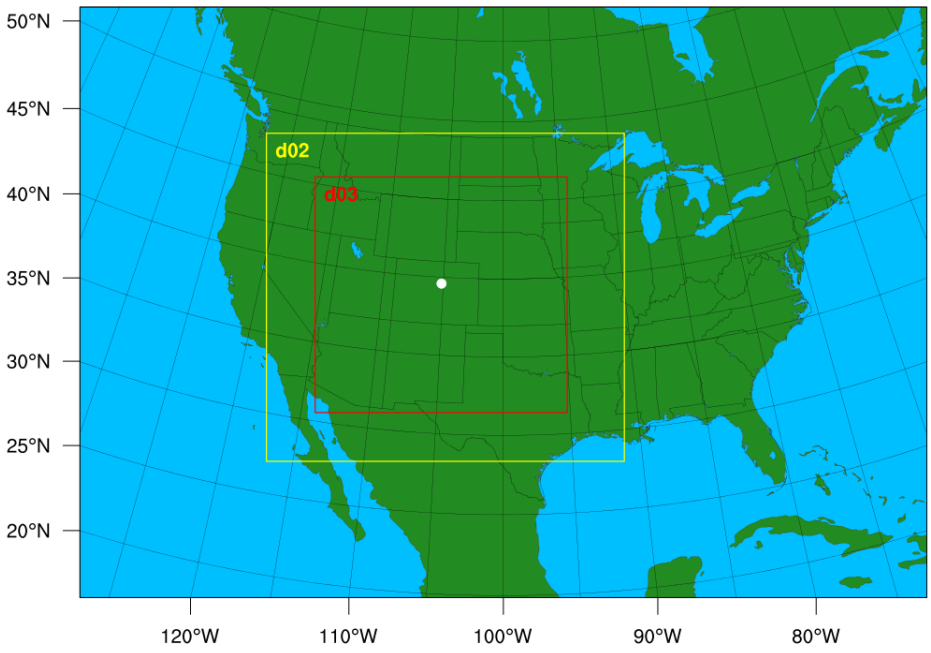

Figure 2.1: ARW model domain configuration with telescoping nests.

Outer domain has a horizontal grid spacing (Δx) of 36 km, inner domain (d02; yellow) Δx = 12 km, and innermost domain (d03; red) Δx = 4 km. A marker location for Boulder, CO (white dot) is provided for reference.

The National Centers for Environmental Prediction (NCEP) Global Forecast System (GFS) model at a 0.5° grid provided the initial and lateral boundary conditions, which were updated every three hours. The Grell-Devenyi 3 (G3; Grell and Devenyi 2002) cumulus parameterization scheme was used for the coarser domains (36 and 12 km). The 4 km nest ran at "convection-permitting" scale so no cumulus parameterization was applied. The Thompson microphysics (MP) scheme (Thompson et al. 2008) was used for all domains. Further detail on the Thompson scheme can be found in section 2.2. The Dudhia shortwave (Dudhia 1989) and the Rapid Radiative Transfer Model (RRTM; Mlawer et al. 1997) longwave radiation schemes were used. The 4-layer Noah land surface model (Chen and Dudhia 2001) was used to calculate the surface heat, moisture, and momentum fluxes, communicating these to the planetary boundary layer, parameterized by the Yonsei University (YSU; Hong et al. 2006) non-local scheme.

This configuration was adapted from the member of the ensemble run by the Schumacher Group at Colorado State University that produced the best forecast of the rainfall in this event. Their ensemble has five members using the ARW model (v3.3.1) with a variety of initial conditions (ICs), lateral boundary conditions, and parameterizations for cumulus, microphysics, land surface, shortwave/longwave radiation, and the planetary boundary layer (http://schumacher.atmos.colostate.edu/weather/csuwrf_info.php). For the ensemble initialized at 0000 UTC 11 September 2013, the 12-36 hour precipitation forecast for "member 2" best captured the "bulls-eye" of high precipitation along the northern Front Range compared to the stage IV analysis from NCEP (Figure 2.2). The model configuration for member 2 was applied

to produce the control simulation in this study, with the addition of a second nested domain with finer resolution (4 km).

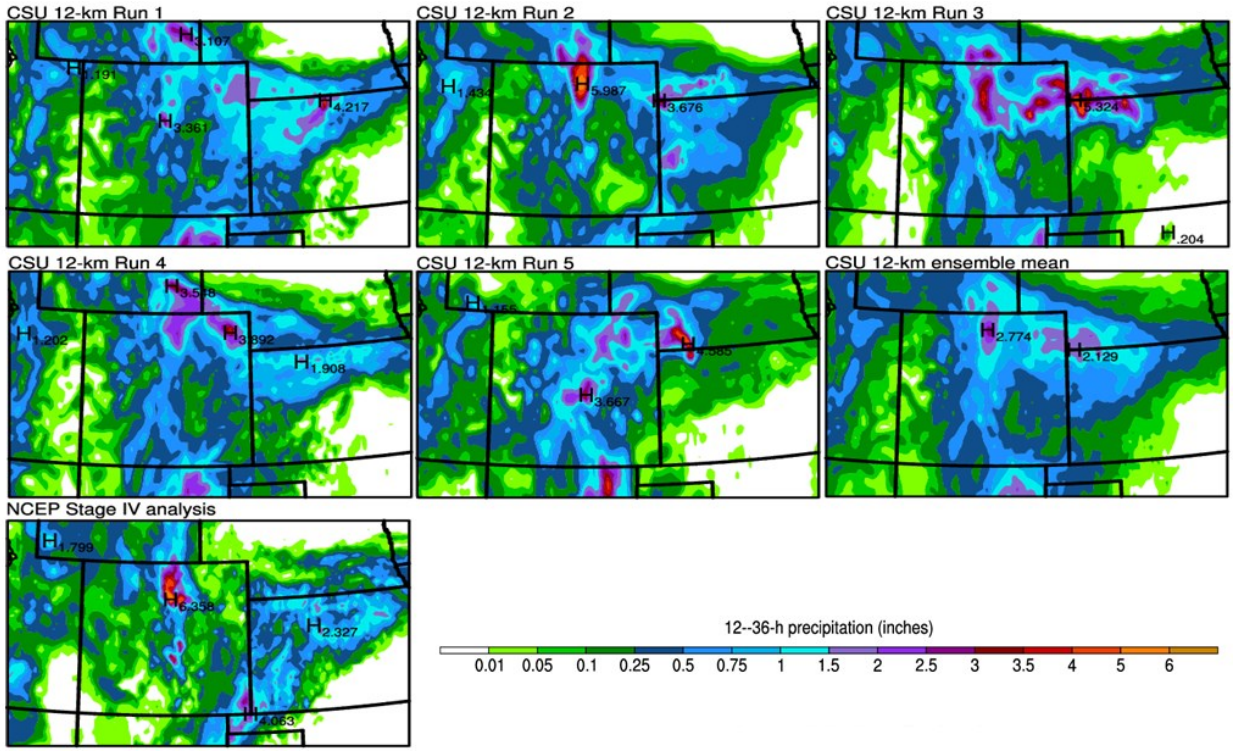

Figure 2.2: Accumulated precipitation for the 36h forecast initialized at 0000 UTC 11 September for the five CSU ARW 12 km ensemble members, the ensemble mean, and the NCEP Stage IV analysis. Images from R. Schumacher CO flood website: http://colorains.blogspot.com/

A study by Schwartz (2014) performed sensitivity tests varying ICs and microphysics parameterizations for a 48 hour simulation initialized at 1200 UTC 11 September 2013 using the ARW (v3.3.1) model. The ICs tested were from the North American Mesoscale Forecast System (NAM) and GFS models. For each IC, the Thompson and Morrison microphysics schemes were applied in separate runs. Their results showed "systematic differences were not attributable to the varied ICs or MP schemes" and that simulations with 1 km horizontal grid spacing better resolved the observed precipitation compared to 4 km (Schwartz 2014). The sensitivity to microphysical parameterization was briefly explored during this study; we found that using the

Morrison scheme did generate the mesoscale feature of interest (i.e., a mesoscale vortex), but the location of maximum precipitation was shifted east with higher precipitation amounts (see Appendix A). We will demonstrate that the use of the GFS ICs and Thompson microphysics for a forecast at 4 km horizontal grid spacing provides a reasonable representation of the mesoscale features of interest, produces a reasonable precipitation forecast, and results in correspondence of the observed and simulated precipitation structures.

2.2 Microphysics Parameterization

As previously noted, the Thompson microphysics scheme (Thompson et al. 2008) was used in this study. The features in this scheme are designed and tuned for operational forecasting, i.e. incorporating microphysical observations and reducing computational costs where possible to enable real-time simulations (Thompson et al 2008). The Thompson scheme is a bulk one-moment (mass mixing ratio only) scheme that is capable of predicting two moments (both mass mixing ratio and number concentration) for rain and cloud ice, as follows. This parameterization contains five hydrometeor species: cloud water, rain, cloud ice, snow, and graupel. With the exception of snow, a generalized gamma distribution (Equation 3) is assumed for each hydrometeor species.

$$N(D) = \frac{N_t}{\Gamma(\mu+1)} \lambda^{\mu+1} D^{\mu} e^{-\lambda D} \tag{3}$$

In Equation 3, N_t is the total number of particles, D is the particle diameter, μ is the shape parameter, and λ is the slope of the distribution. This equation can also be written as

$$N(D) = N_0 D^{\mu} e^{-\lambda D}, \tag{4}$$

where N_0 is the intercept parameter of the distribution. This variable is allowed to vary and is determined from the mixing ratio, as described in Thompson et al. (2008), thus permitting

variations in the number concentration (i.e., effectively predicting an additional moment of the distribution beyond the mass mixing ratio).

The number concentration of cloud water droplets is prescribed and set as a constant, where the default value is 400 cm^{-3}. An experiment using a cloud droplet concentration of 250 cm^{-3} did not inhibit the development of a mesoscale vortex, but did change its location, similar to the result using a completely different microphysics scheme (see Appendix A). The shape parameter for the cloud water distribution is derived through an empirical relationship with the previously set number concentration. Both of these parameters are important in the autoconversion (conversion from cloud water to rain) process in this scheme (Thompson et al. 2008).

Since the Thompson scheme is able to predict two moments for cloud ice, the only free parameter is μ, which is set to zero for the control simulation due to a lack of observational guidance to determine its value (Thompson et al. 2008). Setting μ to zero returns an exponential number distribution (Equation 4).

The Thompson scheme allows a shift in the rain size distribution depending on whether the rain appears to have been produced through melting of ice or collision-coalescence (warm rain process) (Thompson et al. 2008). The intercept parameter will thus vary depending on the dominance of either small drops formed through melting of ice/snow or larger drops formed as drizzle drops grow through accretion. Similarly, graupel also has a varying intercept parameter which is diagnosed from the graupel mixing ratio. The bulk graupel particle density is set to 500 kg m^{-3} for the control simulation and μ for both rain and graupel is set to zero.

The assumed size distribution for snow depends on both ice water content and temperature and is represented as the sum of exponential and gamma distributions. Unlike other

bulk microphysical parameterizations, snow is assumed to have a non-spherical shape (fractal-like aggregate crystals) with density varying inversely with diameter. In this scheme, snow forms through depositional growth of cloud ice; cloud ice particles that grow beyond a threshold size of 200 μm in diameter are "immediately transferred to the snow category" (Thompson et al. 2008).

2.3 Experimental Setup

2.3.1 Latent Heating Experiments

To test the relative importance of lee vortex formation and generation of vorticity via latent heat release from convection in producing the observed mesovortex, a simple experiment was performed in which the latent heating from microphysics (LH) was completely turned off during the simulation (LH_OFF). Phase changes could still occur within the model, but latent heating and cooling associated with these phase changes was not allowed.

After analysis of the LH_OFF experiment, we hypothesized that the origin of the mesovortex that enhanced upslope flow and heavy rain fall on 12 September was in the details of the location and strength of the latent heat release from the storm just prior to the development of the rotational flow. We tested this hypothesis by running the control simulation (herein referred to as "control") with LH turned off for part of the simulation. Again, phase changes were still allowed in the model, but their associated release/uptake of latent heat was not. Experiment LHON_LHOFF was performed to determine if precipitation that occurred on the day prior (11 September) had any impact on the mesovortex observed on 12 September. In this experiment, the latent heating remained on for the first 18 hours of the simulation, from 00Z to 18Z on 11 September 2013, and then was turned off for the remaining 42 hours. The first 18 hours were chosen because by that time the "first round" of precipitation had occurred and dissipated, and

thus the effects of precipitation and heating from these processes would be realized in the model; there were about 6-8 hours remaining in the simulated atmosphere before the mesovortex was observed. The experiment LHOFF_LHON sought to test if the latent heating associated with the precipitation that occurred on the same day as the mesovortex event (12 September) was the primary influence on its development. For this experiment latent heating was turned off for the first 18 hours and then turned on for the remaining 42 hours, from 1800 UTC 11 September to 1200 UTC 13 September 2013. A summary of all the experiments and the mechanisms tested in each experiment can be found in Table 2.1 and Table 2.2, respectively.

Table 2.1: Summary of Latent Heating Experiments

	Latent Heating (LH)			
Forecast Time	Control (LH_ON)	LH_OFF	LHON_LHOFF	LHOFF_LHON
11 Sept 00-18Z	ON	OFF	ON	OFF
11 Sept 18Z – 13 Sept 12Z	ON	OFF	OFF	ON

Table 2.2: Mechanisms Tested by Each Experiment

Experiment	**Reasoning**
Control (LH_ON)	Simulation is used as a proxy for mesoscale observations of the event
LH_OFF	Simulation is used to test the importance of either latent heating or lee vortex formation to the development of the mesovortex
LHON_LHOFF	Simulation is used to test if latent heating from precipitation on prior day had impact on the mesovortex development on 12 September 2013
LHOFF_LHON	Simulation is used to test if latent heating from precipitation on 12 September 2013 had impact on mesovortex development that same day

2.3.2 Latent Heating Calculations

Further analysis of the control simulation was conducted to explore the contribution of microphysics processes to latent heating during the event. This was done by calculating the temperature tendency for "bulk" microphysics processes, i.e. sublimation/deposition, freezing, melting, and condensation/evaporation. The instantaneous freezing (melting) of cloud water (cloud ice) was also incorporated because it was included as a source of latent heating in the Thompson microphysics scheme. The individual processes included in each bulk term can be found in Appendix B. The following equations and constants were used to calculate the temperature tendencies for the bulk microphysics terms:

$$\Delta T = L_x \, {C_p}^{-1} \rho^{-1} \, mprate \tag{5}$$

$$C_p = 1004 \, (1 + 0.887 Q_v), \tag{6}$$

$$\rho = \frac{0.622 \text{ P}}{\text{R T(K)}(Q_v + 0.622)} \tag{7}$$

These equations were obtained from the Thompson parameterization within the ARW model. L_x is the latent heat of vaporization, fusion, or sublimation in J kg^{-1}, C_p is the heat capacity at a constant pressure in J kg^{-1} K^{-1}, ρ is the air density in kg m^{-3}, $mprate$ is the accumulated microphysics process rate in kg kg^{-1} for each forecast hour, Q_v is the water vapor mixing ratio in kg kg^{-1}, P is pressure in Pa, R is the gas constant for dry air (R = 287.04 J kg^{-1} K^{-1}), and T is the temperature in K. For the condensation/evaporation term, density was excluded from the calculation in Equation 5.

The instantaneous freezing/melting temperature tendencies were calculated in a similar manner as their treatment within the model, namely, any cloud ice would instantly melt into cloud water if it was above 0°C and cloud water would instantly freeze if located below the homogeneous freezing temperature (235.16 K or -38°C).

There was a small discrepancy between the calculated total microphysics heating (as described above) and the total microphysics heating calculated explicitly by the model (Figure 2.3). The reason behind this discrepancy may be due to the way the model derives the amount of heating. The model retrieves the required variables in the equations at every time step, but the manually calculated values come from variables collected at every hour when the data are output. The resulting differences in temperature were less than 1 K, and the shape of the microphysics heating profiles were very similar. Therefore, although there are small quantitative differences between the derived and model-predicted latent heating profiles, these differences do not affect the interpretation of the results.

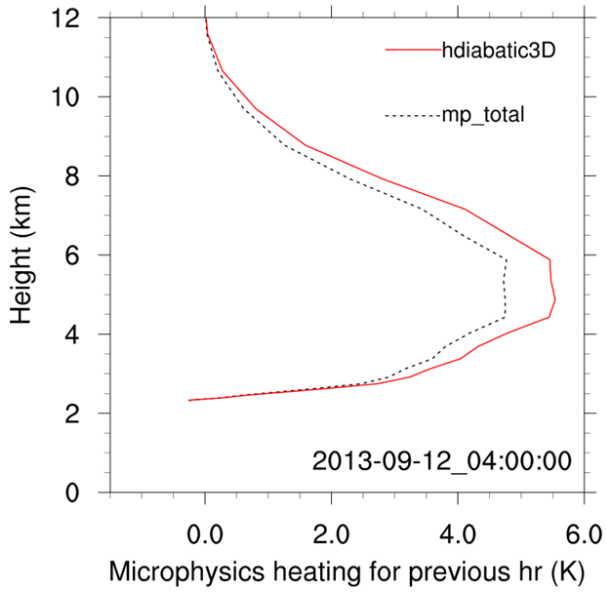

Figure 2.3: Vertical profiles of latent heating from microphysics (K) for values explicitly derived by the model ("hdiabatic3D"; red solid line) and the calculated total ("mp_total"; black dotted line).

2.3.3 Latent Heating Sensitivity Experiment

After exploring the dominant microphysical processes occurring during the simulation, a simple test was implemented to isolate the impacts of latent heating from a process responsible

for the positive vertical gradient in diabatic heating near the surface. We hypothesized that a reduction in latent heating from cloud water condensation would reduce the vertical gradient in latent heating, leading to less generated PV and inducing a weaker (or no) cyclonic circulation. To test this hypothesis, we ran an experiment (referred to as LHOFF_LHHALF) in which the contribution of latent heat from condensation/evaporation of cloud water was reduced by half. Similar to LHOFF_LHON, the latent heat was not reduced until 1800 UTC 11 September.

Reducing the latent heat contribution while allowing the same conversion of mass between phases is not physical. Of course, removing a large fraction of the energy source will feed back to convection and will change the simulation even for this scenario. Another option to simulate less latent heat release might be to reduce the droplet number concentration, as can be seen from the following equation:

$$L_v \frac{dM_{cw}}{dt} \propto L_v N_D^{2/3} M_{cw}^{1/3} C (s - s_k) \quad (8)$$

where the total rate of cloud water mass change multiplied by the latent heat per unit mass (on left hand side) gives the rate of release of energy. Assuming the cloud water mass ($M_{cw}^{1/3}$), constants (C), and a driving force (s-s_k) do not change much with rate of condensation, the release of energy will be directly proportional to the number concentration of cloud water droplets ($N_D^{2/3}$). However, reduced droplet number concentrations will also cascade into other microphysical processes (e.g., drizzle formation rates may be affected), and thus the impact of the heating alone on the vortex development cannot be isolated and assessed with such a change. We chose to adjust the latent heating directly as that appears to have fewer immediate microphysical feedbacks.

3. Results and Discussion

3.1 Control Simulation

3.1.1 Large-Scale Conditions

The synoptic pattern that helped establish the ingredients needed for heavy precipitation on 11-12 September was well represented by the ARW control simulation (LH_ON). Figure 3.1 shows that prior to the mesoscale vortex event, the position of the forecasted cut-off low was in the southwestern U.S., similar to the observations. In the lower troposphere, both the previously mentioned low and the position of the subtropical high in the southeastern U.S. were forecasted well (Figure 3.2). The wind patterns that transported moisture aloft from the western coast of Mexico and those near the surface that transported moisture from the Gulf of Mexico towards the Colorado Front Range, were also well represented (Figure 3.1 and Figure 3.2, respectively).

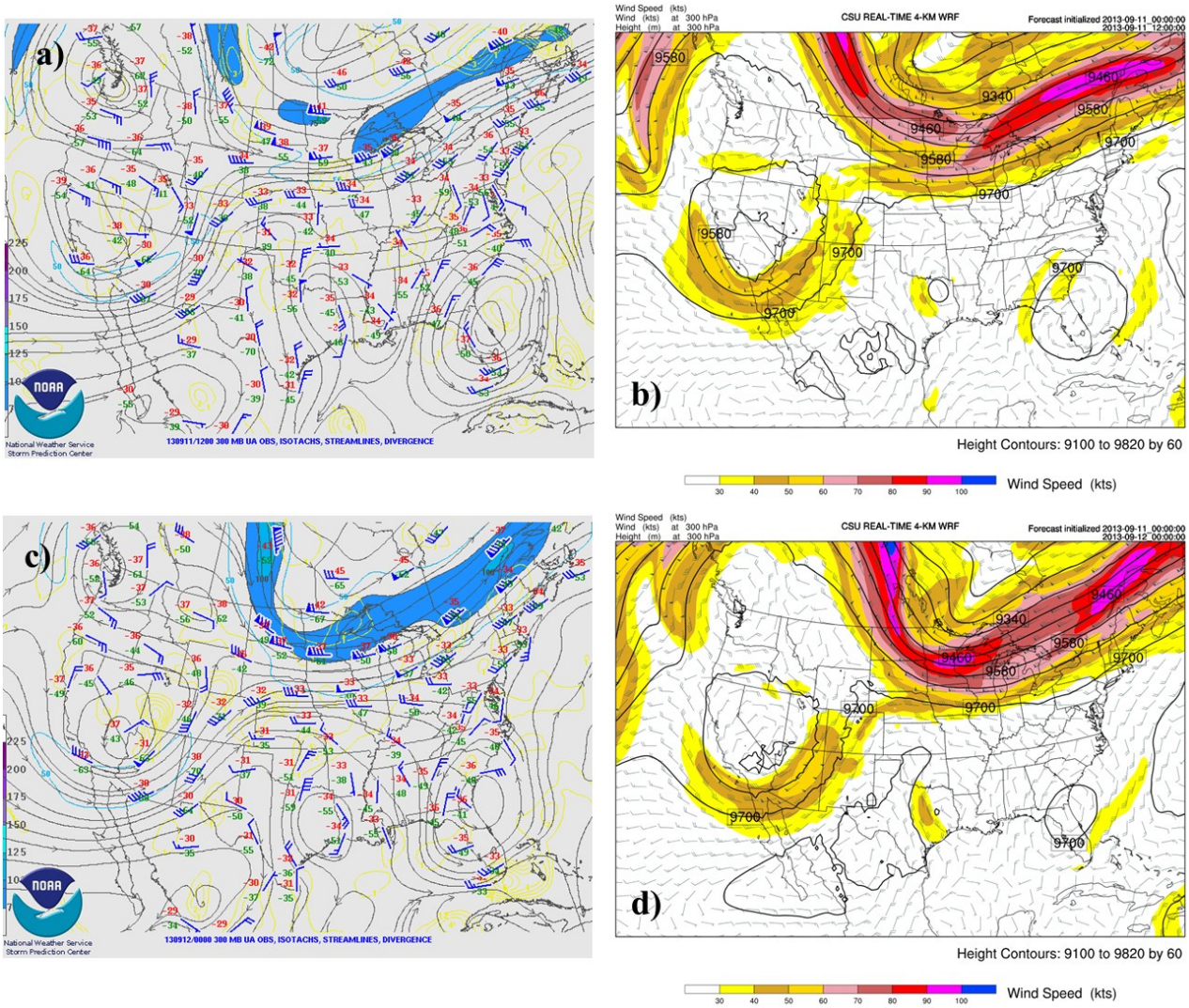

Figure 3.1: 300 hPa maps of the ARW forecast (left) and SPC analysis (right) for (a-b) 1200 UTC 11 September and (c-d) 0000 UTC 12 September.

The figures on the left side show upper air observations, streamlines (gray contours), and isotachs (kts; color). Figures on the right side show geopotential heights (m; black contours), winds (kts; barbs) and absolute vorticity (10^{-5} s^{-1}; color fill).

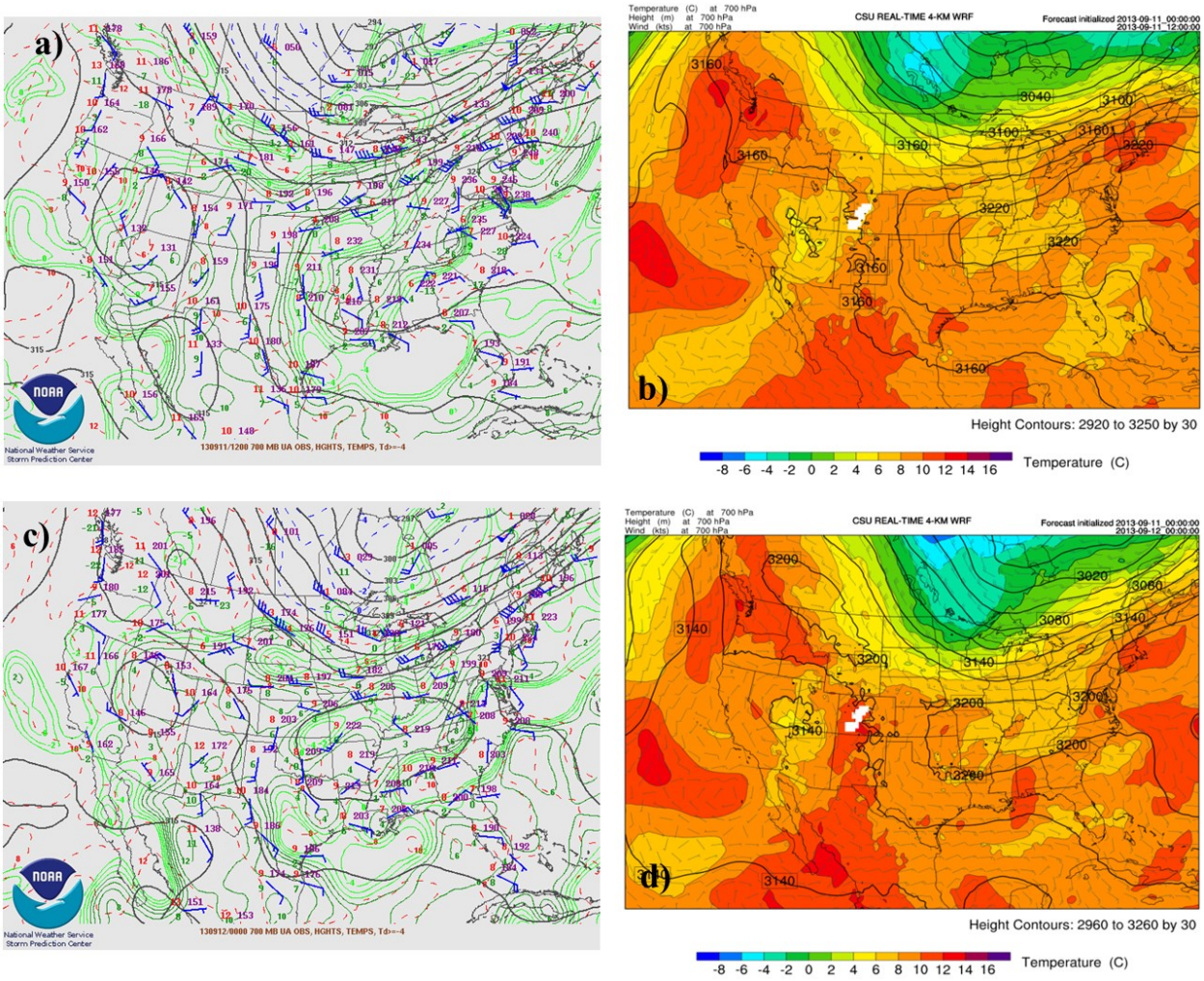

Figure 3.2: 700 hPa maps of ARW forecast (left) and SPC analysis (right) for (a-b) 1200 UTC 11 September and (c-d) 0000 UTC 12 September.
The figures on the left side show upper air observation, geopotential heights (dm; black contours), temperature (°C; red dashed contours), and dewpoint temperatures (°C; green contours). Figures on the right side show geopotential heights (m; black contours), winds (kts; barbs) and absolute vorticity (10^{-5} s^{-1}; color fill).

The large-scale transport of moisture led to high values of PW in eastern Colorado (Figure 3.3a). The control simulation represented the high PW values of over 30 kg m^{-2} very well (Figure 3.3b).

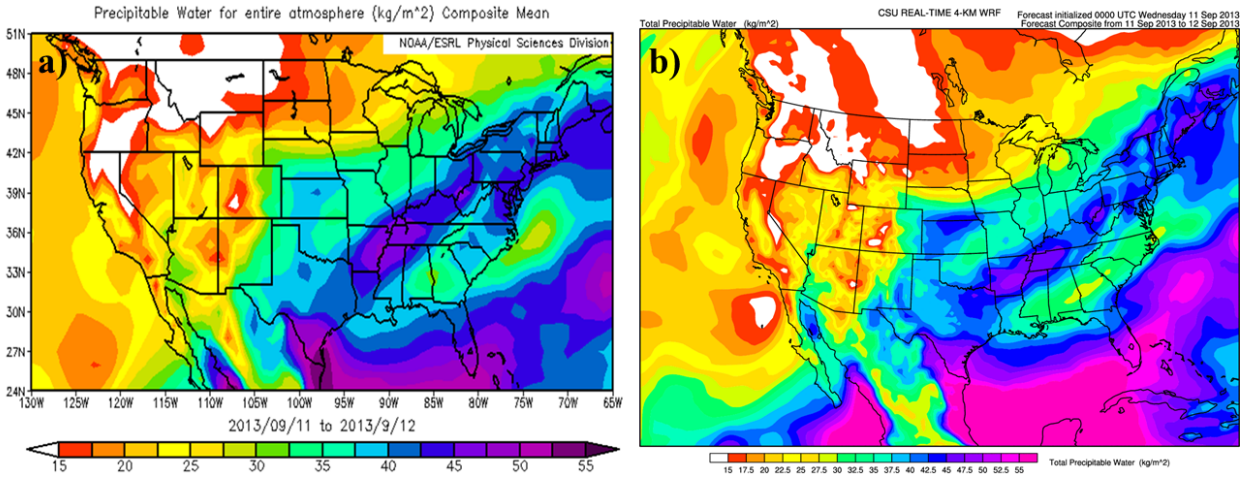

Figure 3.3: Precipitable water for entire atmosphere (kg/m^2) from the (a) NCEP North American Regional Reanalysis and (b) ARW forecast. Values are composite mean for 11 Sept. 2013 and 12 Sept. 2013. Image (a) provided by the NOAA/ESRL Physical Science Division, Boulder Colorado from their website at http://www.esrl.noaa.gov/psd/.

The atmospheric profile for Denver prior to the mesoscale vortex formation showed moist conditions from the surface to 500 hPa, with PW values of 32.7 mm (Figure 3.4a). The saturated conditions near the surface suggest that this radiosonde was launched through clouds and possibly precipitation. The forecast sounding is moist above 700 hPa and has a relatively dryer layer near the surface, most likely because the profile went through an environment where there was no cloud or precipitation near the surface (not shown) in that particular location at the given time (Figure 3.4b). Because of this drier surface layer, the forecasted PW was a bit lower than the observed, with a value of 28.87 mm. For both profiles the lower troposphere winds were generally weak (~5 m/s) and from the southeast, resulting in upslope flow near the surface (Figure 3.4).

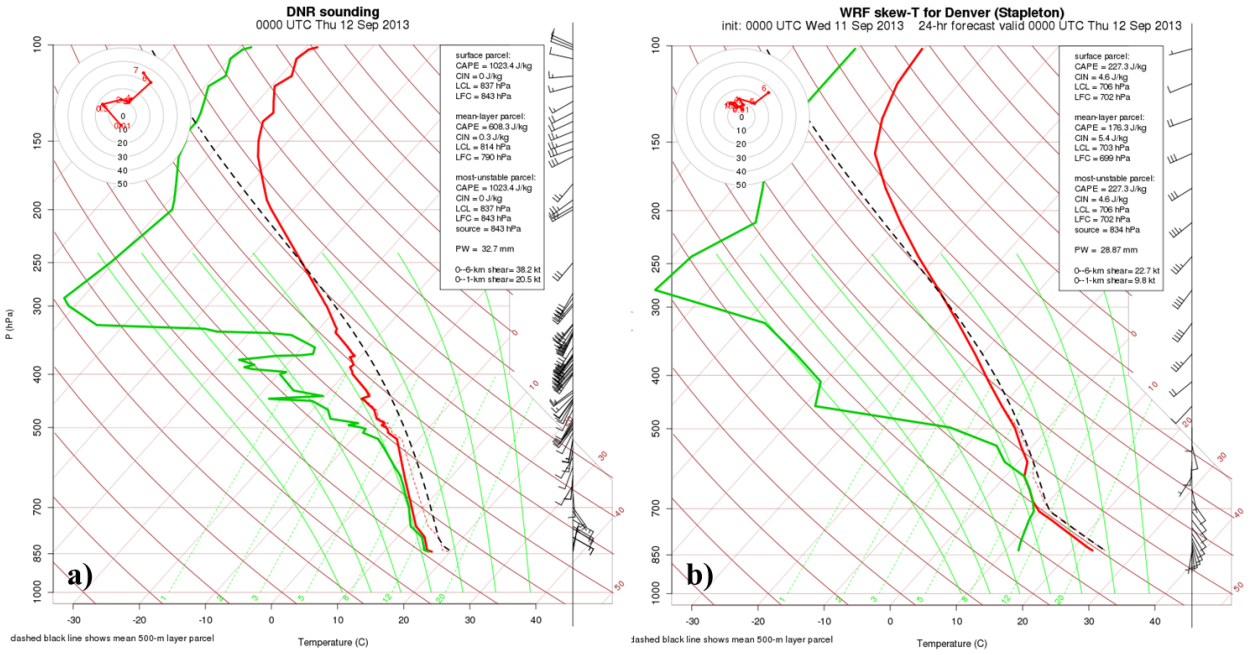

Figure 3.4: Atmospheric profiles for Denver (DNR) at 0000 UTC 12 September for (a) observations and (b) ARW forecast.
Red solid line is temperature profile, green solid line is dewpoint temperature profile, and black dashed line shows mean 500 m layer parcel.

3.1.2 Radar Reflectivity

A comparison between the radar reflectivity from the observations and the control simulation at 1 km above ground level (AGL) shows that the heavy precipitation event was well represented (Figure 3.5). For example, at 0600 UTC the precipitation over Boulder and Larimer counties was well placed, with higher reflectivity values over Boulder as shown in Figure 3.5e. This is not to say the model was perfect; the simulations sometimes missed the intensity, location, or areal extent (further precipitation analysis in Section 3.1.4). For example, Figure 3.5b shows high reflectivity values were modeled over central Boulder County and over Fort Collins, when the observations indicate that there were smaller convective cells east of Boulder and Fort Collins. The northwest-southeast oriented band of precipitation east of Boulder at 0300 UTC attempted to form in the simulation, but ended up as broken areas of precipitation. The

horizontal grid spacing used in the innermost domain allows for convection, but it is not fine enough to simulate the sizes of the smaller cells seen in the observations. Nevertheless, the model configuration produced a good representation of the event along the Colorado Front Range that is of primary interest to this study, as demonstrated further in the next section where various skill scores are evaluated.

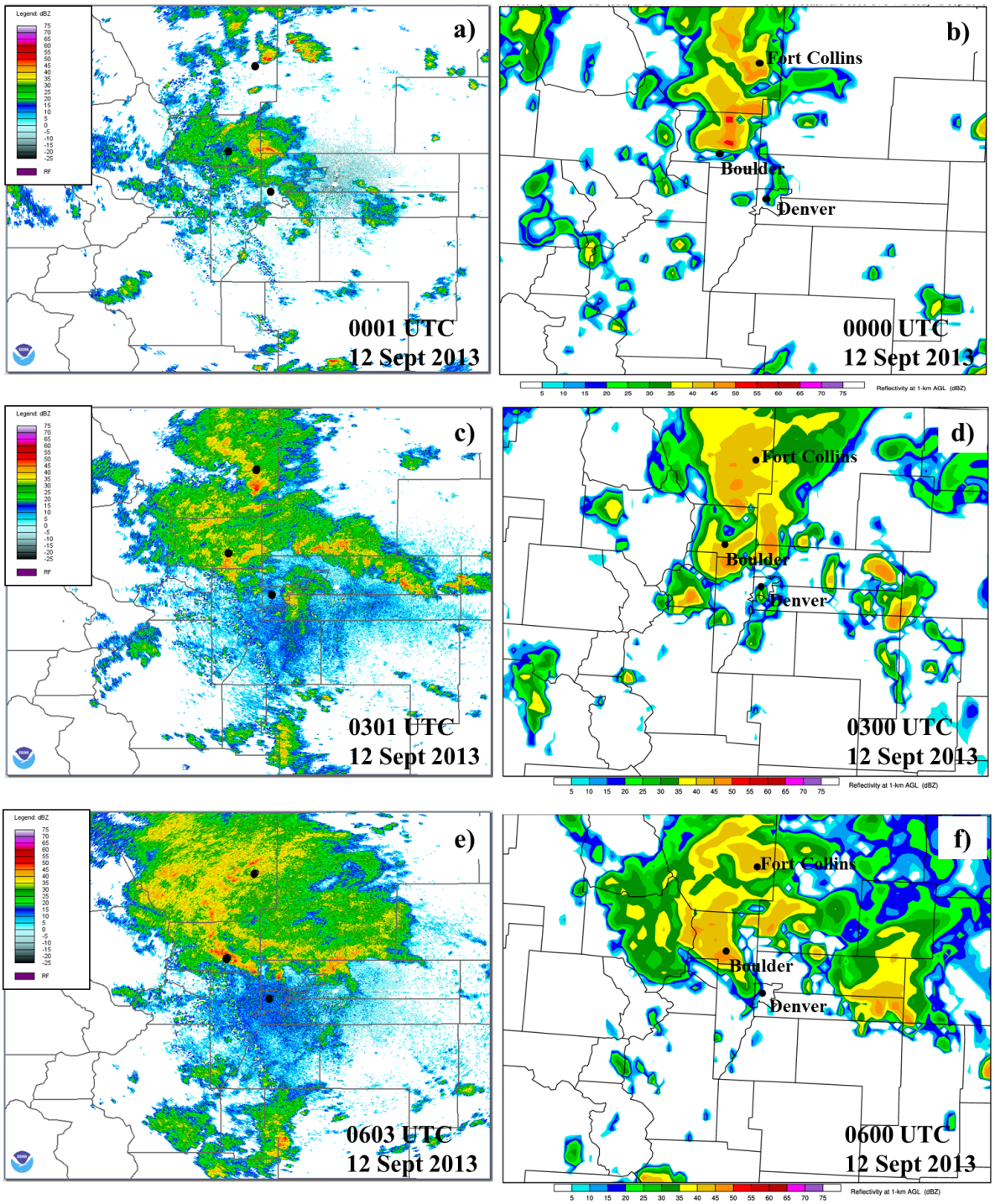

Figure 3.5: Radar reflectivity for NEXRAD Level II data from KFTG (Denver, CO) (left) and ARW forecast at 1 km AGL (right) for (a-b) 0000 UTC 12 September, (c-d) 0300 UTC 12 September, and (e-f) 0600 UTC 12 September. NEXRAD data is for an elevation angle of 0.5°. Markers for major cities are provided as a reference.

3.1.3 Accumulated Precipitation

Traditional verification metrics, e.g. Gilbert Skill Score (GSS), Heidke Skill Score (HSS), the frequency bias (FBIAS), and Fraction Skill Score (FSS), were used to verify the 12-36 hour accumulated precipitation for a number of precipitation thresholds (>12.5 mm, >25 mm, >50 mm, >100 mm, and >150 mm). In general, a score of 1 is a perfect forecast for all skill scores. The verification was performed by using the Meteorological Evaluation Tools (MET) software (Developmental Testbed Center 2013) to compare the ARW forecast to the NCEP Stage IV analysis (which combines radar and rain gauge observations; Lin and Mitchell 2005). The NCEP Stage IV precipitation analysis did have some problems with its estimates during the event, e.g., biases caused by radar reflectivity rainfall relationships (Gochis et al. 2014), but for the purpose of this study, which focuses on the mesoscale regions of heavy rainfall rather than the specific point maxima, the interpretation of the results are not likely to be affected (even if the specific quantitative calculations vary slightly). For a description of these verification methods and how they are derived see Appendix C.

For the 12-36 hour accumulated precipitation ending at 1200 UTC 12 September within the 4 km domain, the skill scores were representative of a good forecast. The verification area focused over Colorado and included neighboring states (area same as shown in Figure 3.7a). Both the GSS and HSS remained below 0.5 and were also constant with threshold, except for the highest threshold which had very low skill (i.e. higher amounts of precipitation were more difficult to forecast). The FBIAS was near 1 for lower precipitation thresholds, increased for 50 mm and 100 mm thresholds (overprediction of forecasted rainfall), then decreased for the highest threshold (Figure 3.6). The FSS tended to be fairly constant above 0.5 with increasing threshold (Figure 3.6).

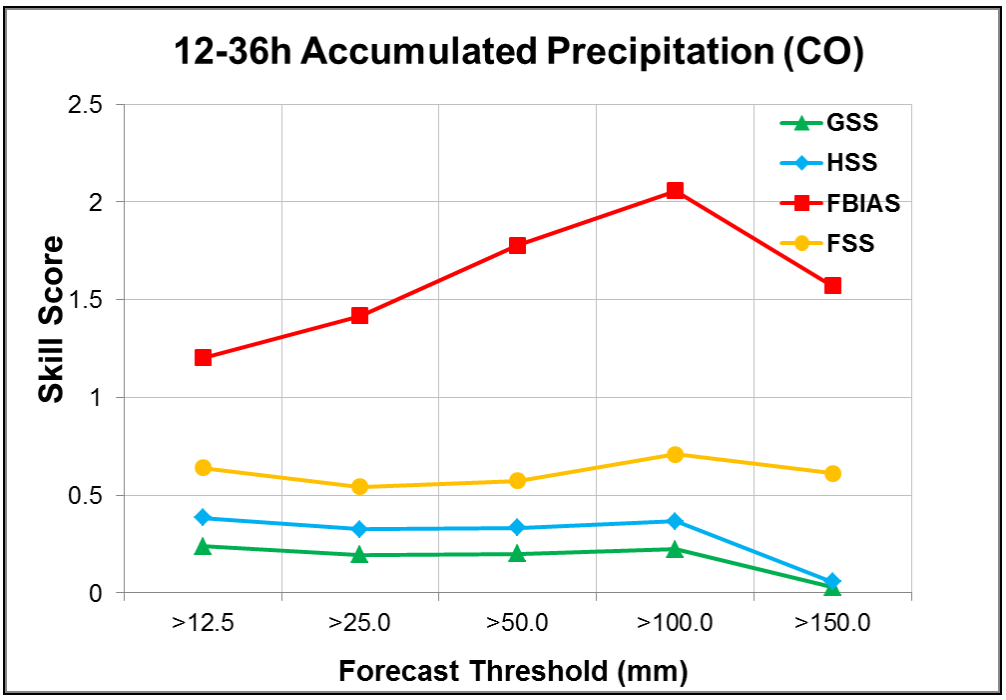

Figure 3.6: Forecast skill scores for the 12-36 hour accumulated precipitation.
The ARW forecast was verified against the Stage IV observations over the state of Colorado using the Model Evaluation Tools (MET) software. The Gilbert Skill Score (GSS; green triangle), Heidke Skill Score (HSS; cyan diamond), Frequency Bias (FBIAS; red square), and Fraction Skill Score (FSS; yellow square) were evaluated for thresholds of 12.5 mm, 25 mm, 50 mm, 100 mm, and 150 mm.

The control simulation captured the main regions of heavy precipitation, i.e. the bulls-eye located near Boulder along the northern Front Range, the southeastern corner of Colorado, and the wide region over northwestern Kansas (Figure 3.7a-b). Focusing over the northern Front Range, the simulation did miss the pockets of high precipitation in the southern Front Range and had precipitation over northeastern Colorado when the observations showed little precipitation (Figure 3.7c-d). The highest value of precipitation near Boulder (denoted with an H in Figure 3.7c-d) was underpredicted by the model by 46 mm (1.8 in). Although the maximum rainfall amounts over northern Colorado were underpredicted and the areal coverage of rain amounts

greater than 50 mm were overpredicted, the general spatial distribution of precipitation and the location of the heaviest rainfall were well captured.

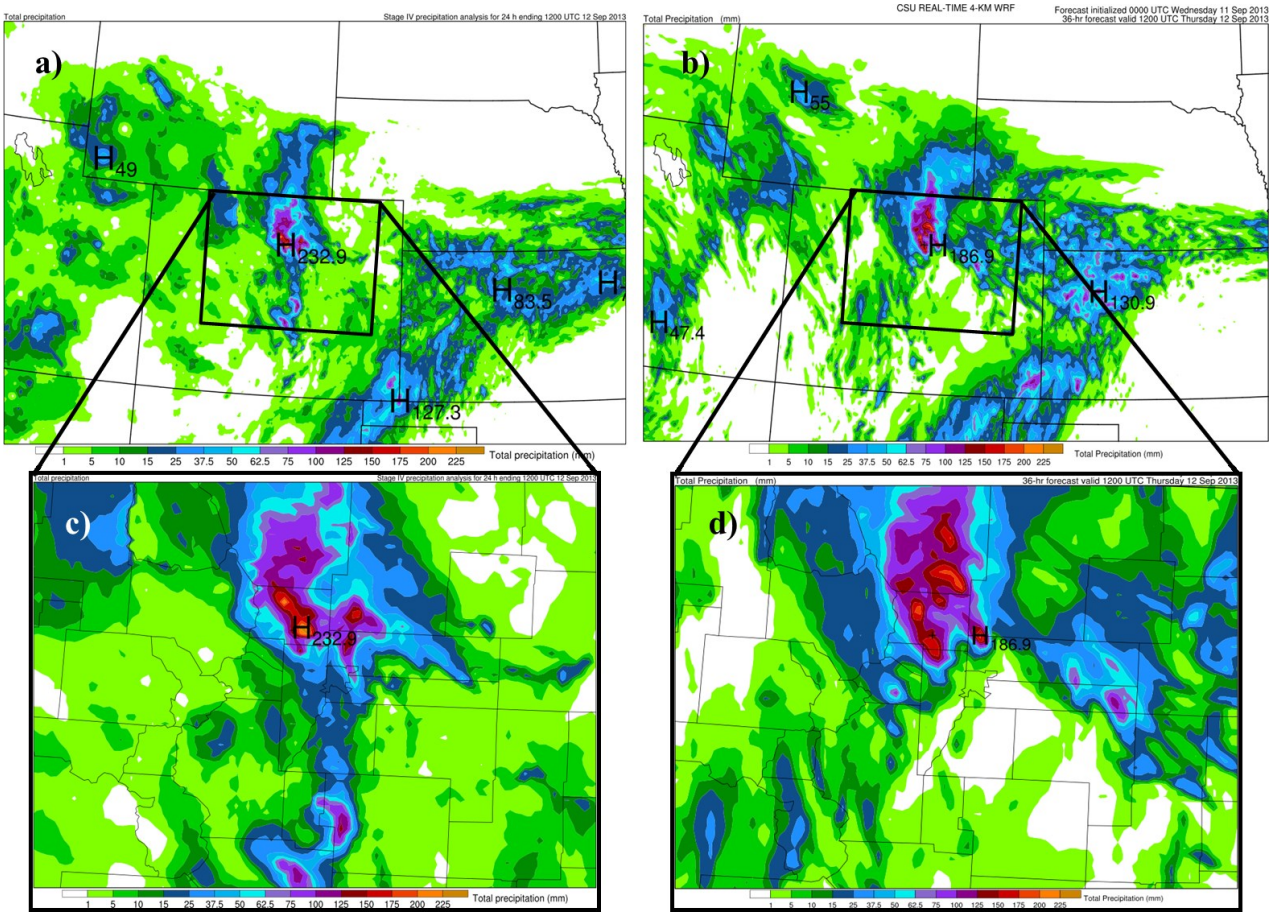

Figure 3.7: NCEP Stage IV analysis (left panels) and ARW model forecast (right panels) 24 hr accumulated precipitation (mm) valid at 1200 UTC 12 September.
(a) observations and (b) the forecast with zoomed in sections focusing over northern Colorado for each (c and d, respectively). High precipitation values in zoomed in sections are (c) 232.9 mm and (d) 186.9 mm. The "+" marker denotes the location of Boulder, CO.

In high-resolution forecasts of discrete fields (such as precipitation), traditional evaluation methods often produce scores that run counter to human evaluation because they give a "double penalty" to forecasts that have slight displacement errors but are otherwise accurate. One method for alleviating this problem is object-based evaluation, where contiguous regions exceeding a given threshold are classified into "objects" in both the forecast and observed fields.

Here, the Method for Object-based Diagnostic Evaluation (MODE; Brown et al. 2004; Davis et al. 2006) was used to conduct this type of forecast evaluation. MODE uses a filter and given thresholds to identify objects in the gridded field. These objects are then merged within a field and matched between the forecast and observations using a "fuzzy" logic scheme. The attributes analyzed here are the total interest, area ratio, centroid distance, and symmetric difference. Total interest is a summary statistic derived using fuzzy logic (value of one is good). Area ratio and centroid distance provide a quantitative measure of areal extent (forecast area/observed area) and spatial displacement (small value is good), respectively. Symmetric difference is a summary statistic describing how well forecast and observed objects matched (small value is good).

Focusing on "cluster pair 1" located over the northern Front Range (Figure 3.8), the object pair attributes were all very good for thresholds >25 mm and >100 mm (Table 3.1). These attributes essentially show that the spatial distribution of precipitation was very well forecast, especially for the >100 mm threshold (symmetric difference was much smaller than >25 mm threshold). The MODE analysis, and the traditional verification metrics discussed above, all illustrate that the model-predicted precipitation very closely resembled observations at the spatial scales of interest to this study.

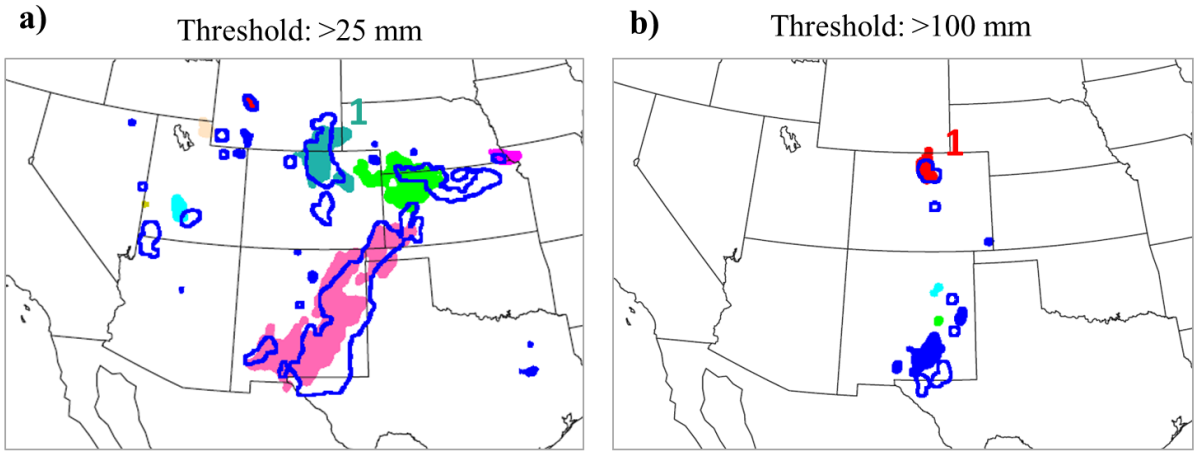

Figure 3.8: Forecast objects with observation outlines for a threshold of (a) >25 mm and (b) >100 mm.

The spatial distribution of the ARW forecasted 12-36h accumulated precipitation was verified against the NCEP Stage IV observations using the Method for Object-based Diagnostic Evaluation (MODE) built-in tool in the MET software. Precipitation thresholds used were (a) >25 mm and (b) > 100 mm. The cluster pair attributes for cluster 1 in (a) and (b) are found in Table 3.1.

Table 3.1: Object pair attributes for cluster pair 1 over the northern Colorado Front Range.

Object Pair Attribute	**Threshold: >25 mm**	**Threshold: >100 mm**	**Optimal Value**
	Cluster Pair 1	Cluster Pair 1	
Total Interest	0.9914	0.9716	1
Area Ratio	1.3528	1.4952	1
Centroid Distance	4.74 km	5.83 km	Small value
Symmetric Difference	2897 grid boxes	314 grid boxes	Small value

3.1.4 Model Representation of Mesovortex

As described in Section 1.2.3, the mesovortex was observed to originate northwest of Denver and move north-northwest towards Boulder (Figure 1.12). Horizontal plots of potential vorticity at 1 km AGL show the evolution of the vortex within the model (Figure 3.9). This specific level was selected to best demonstrate the evolution of the mesovortex in horizontal

maps. The trajectory of the simulated mesoscale vortex was similar to the observations, located between Denver and Boulder and eventually moving into Boulder (Figure 3.9). The duration and timing of the vortex was also well represented, with the circulation being strongest between 0400-0600 UTC and reaching Boulder at approximately 0600 UTC 12 September (Figure 1.12b and Figure 3.9d). The enhanced upslope flow and LLJ observed in the radial velocity (Figure 1.12b) and wind profiler observations (Figure 1.13) is also captured in the control simulation. The forecasted LLJ is located in northern Colorado, north and northeast of the mesovortex with westward winds at speeds up to 15 m/s.

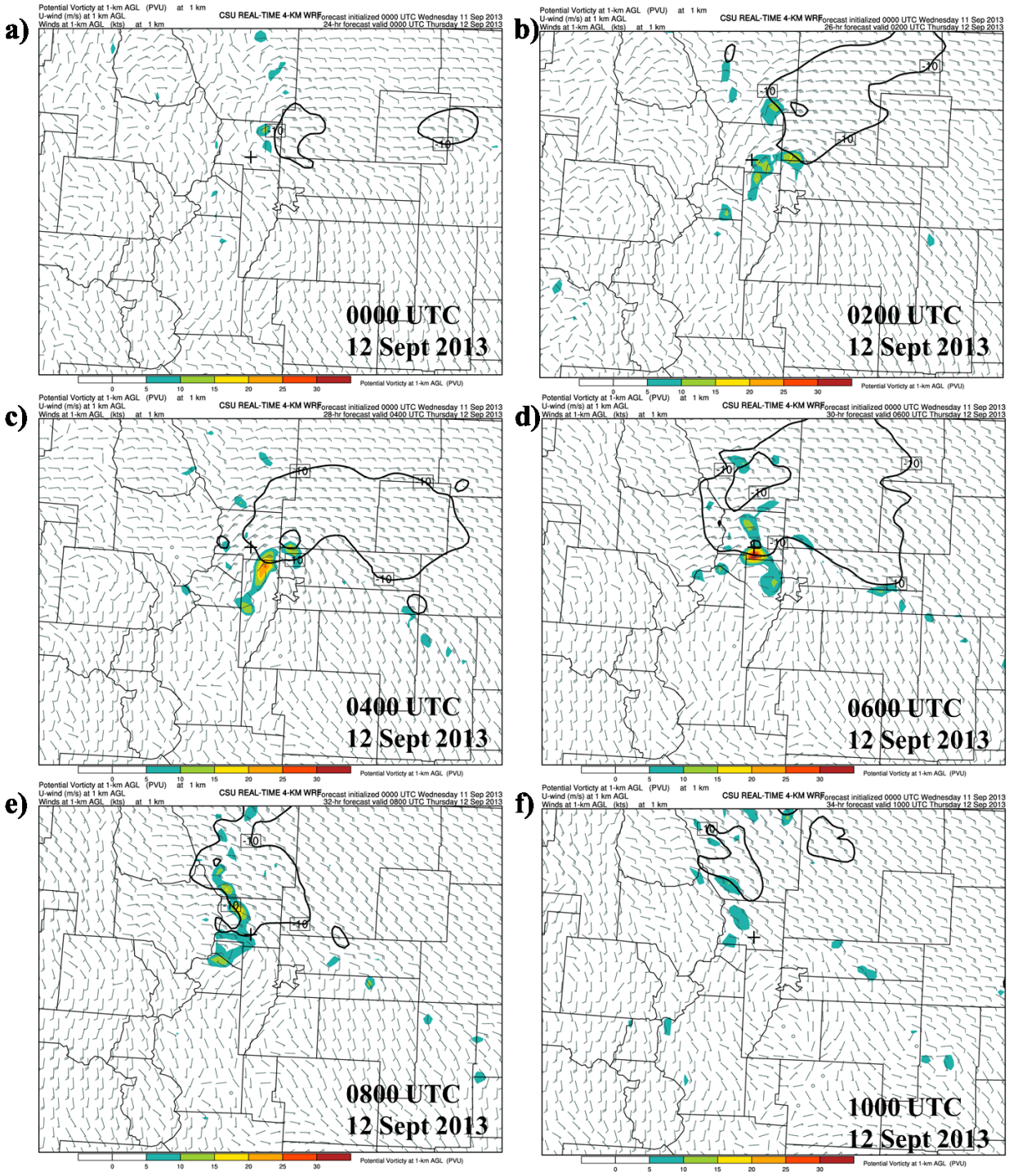

Figure 3.9: Evolution of mesoscale vortex from control simulation.
Potential vorticity (PVU; color fill), negative u-wind (m/s; solid black line), and wind barbs (kts) all at 1 km AGL for 0000, 0200, 0400, 0600, 0800, and 1000 UTC 12 September 2013 (a-f, respectively). U-wind contour interval is 5 m/s, starting at -10 m/s. A marker "+" is provided for reference and denotes the location of Boulder, CO.

The good representation of the processes of interest in the control simulation allowed us to further investigate the characteristics of the mesovortex. A west-to-east vertical cross-section at 0500 UTC 12 September of PV and radar reflectivity is provided in Figure 3.10b over the location shown in Figure 3.10a. This analysis shows PV > 5 PVU to extend from the surface up to ~10 km above mean sea level (MSL), with the PV maximum (>30 PVU) residing between approximately 3-6 km MSL. The depth of the radar reflectivity generally follows that of the vortex, with higher values located below 6 km MSL (Figure 3.10b). The location of the higher radar reflectivity values is expected due to the precipitation mainly falling as rain, i.e. if the precipitation was hail one would expect high reflectivity higher up within the storm. The local maximum in PV is co-located with areas of high radar reflectivity, signaling a relationship to convectively active regions.

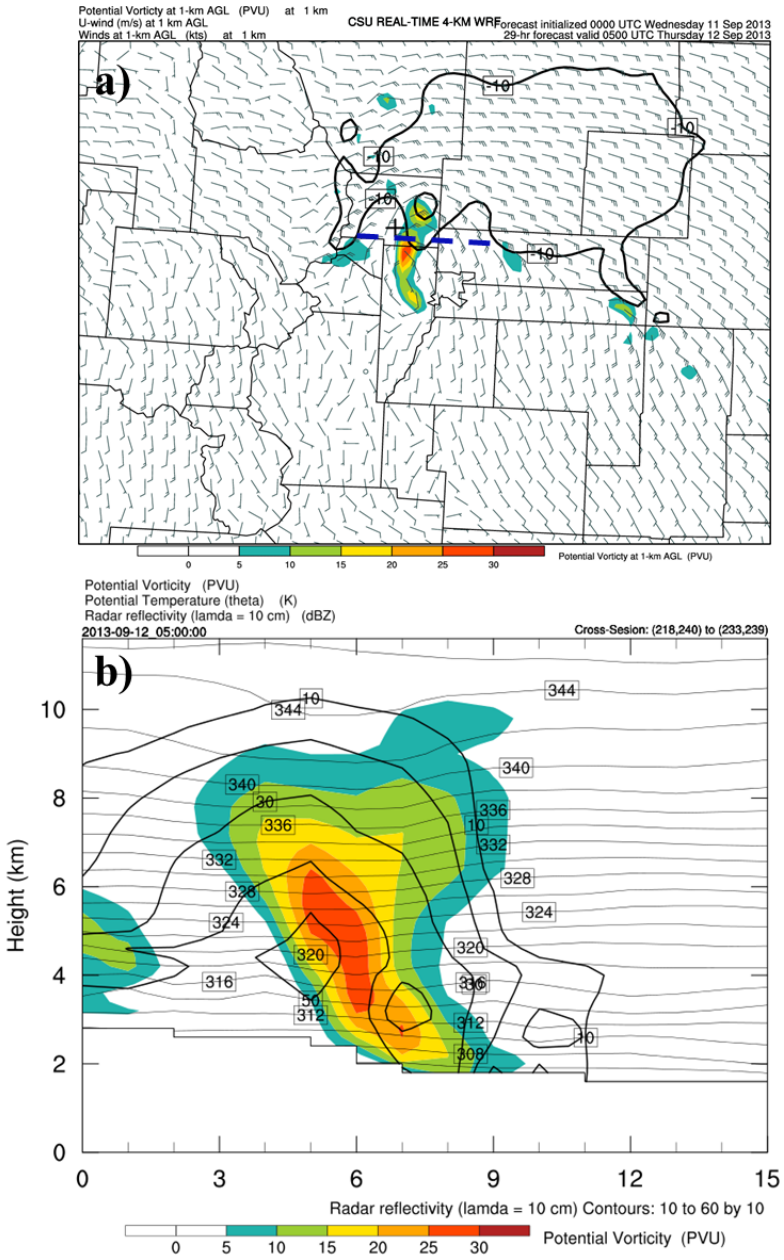

Figure 3.10: Horizontal map and vertical cross-section through the mesovortex from control simulation.

For 0500 UTC 12 September: (a) same as in Figure 3.9, (b) west-to-east vertical cross-section [denoted by dashed blue line in (a)] of potential vorticity (PVU; color filled), radar reflectivity (dBZ; black contours); and potential temperature (K; gray lines). Simulated radar reflectivity contour interval is 10 dBZ, labeled at an interval of 20 dBz; potential temperature contour interval is 2 K; vertical axis is height in km MSL and horizontal axis is number of grid points along location of cross-section in (a).

3.2 Latent Heating Experiments

3.2.1 LH_OFF Experiment

This experiment had latent heating from microphysical processes turned off for the entire simulation. This simple experiment aimed to test the relative importance of lee vortex formation and latent heating as mechanisms for vortex development during the 12 September phase of the storm. Analysis will be focused on the first 6 hours (UTC) of 12 September, when the vortex developed and moved towards Boulder, CO. The results of this experiment showed that the removal of latent heating had a severe impact on the low-level flow both along the Front Range and in much of eastern Colorado. The flow at 1 km AGL in both LH_ON and LH_OFF had a similar southeasterly direction in southern Colorado and along the mountains (west of Boulder), but along the northern Colorado Front Range the flow was dramatically different with respect to the mesovortex (or lack thereof) and LLJ (Figure 3.11). At 0200 UTC, there was no sign of a LLJ or mesovortex in LH_OFF; the flow generally remained south-southeasterly along the northern Front Range and in the northeastern plains (Figure 3.11d). At 0600 UTC, Figure 3.12d shows the lack of both the large LLJ (depicted by solid black contours of negative u-wind in Figure 3.12a) and the vortex located near Boulder (high values of potential vorticity and cyclonic flow in Figure 3.12a). Overall, LH_OFF had weaker winds (about 5 m/s lower) and maintained a south-southeasterly flow throughout the simulation.

The lack of formation of a mesovortex when latent heating was turned off suggests that lee vortex formation was not the primary mechanism for the circulation's development. The flow in the LH_OFF case was southeasterly around the Denver/Boulder area, which is the favored direction for lee vortex formation to develop a Denver Cyclone. Both simulations had the same topography, yet only the control formed a mesovortex and LLJ. These results suggest that the

development of the cyclonic circulation was not consistent with the processes that cause the Denver Cyclone.

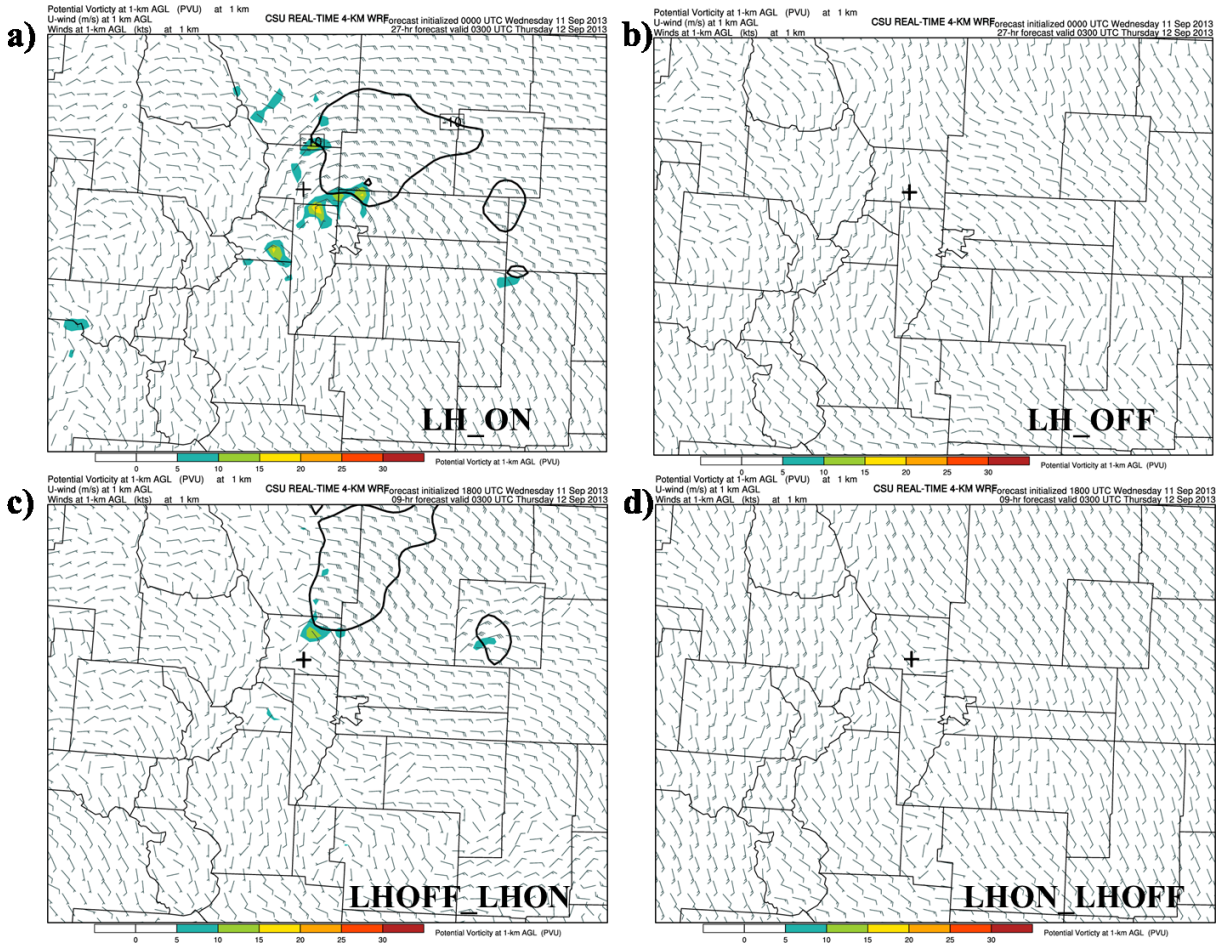

Figure 3.11: ARW model simulations at 1 km AGL of absolute vorticity (10-5 s-1, color), u-wind (m/s, solid black line), and wind barbs (kts) at 0300 UTC 11 September 2013.
(a) LH_ON (control), (b) LHON_LHOFF, (c) LHOFF_LHON, and (d) LH_OFF simulations. U-wind contour interval is 5 m/s, starting at -10 m/s. A marker "+" is provided for reference and denotes the location of Boulder, CO.

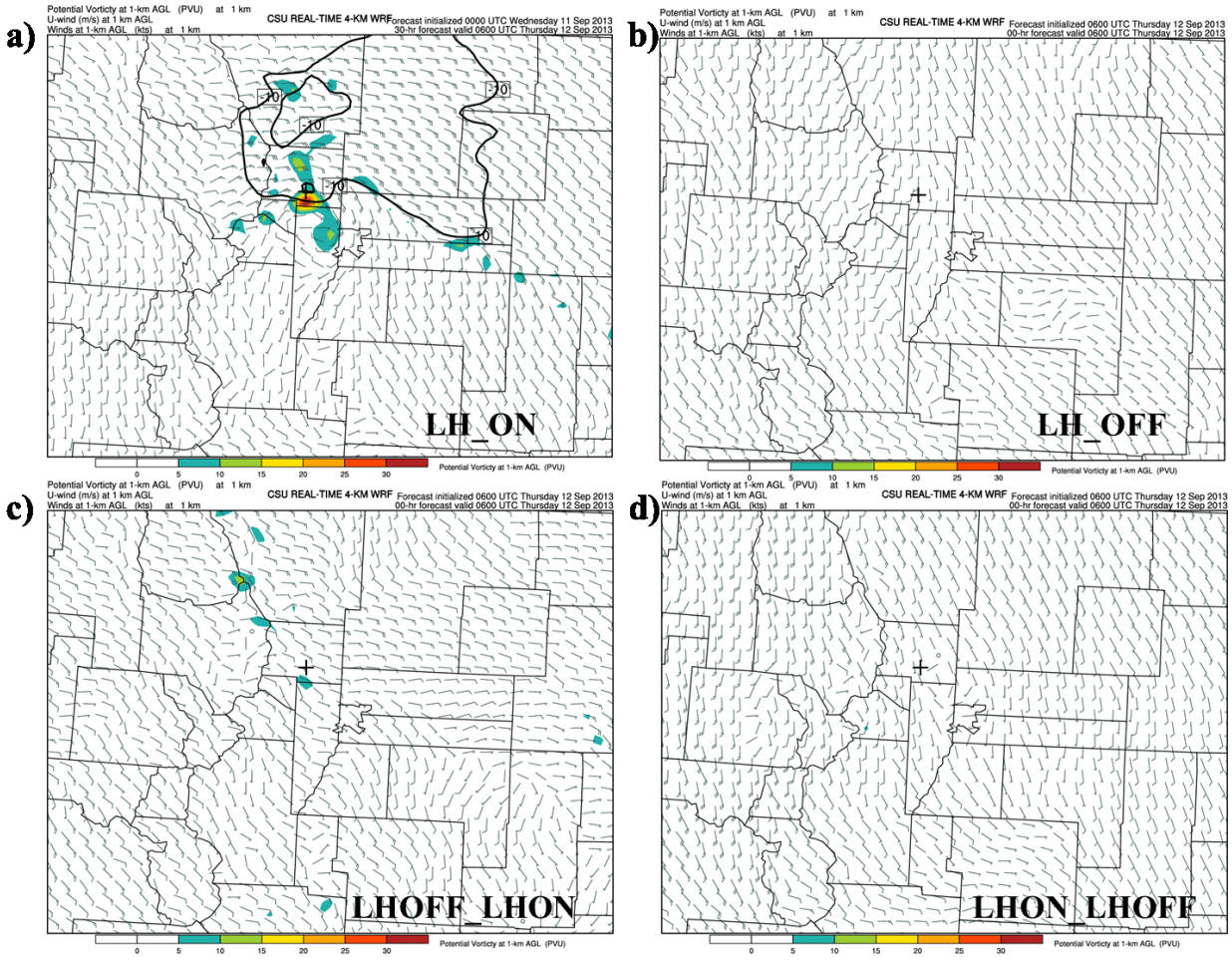

Figure 3.12: Same as Figure 3.11, but for 0600 UTC 12 September.

3.2.2 LHON_LHOFF and LHOFF_LHON Experiments

The LH_OFF results showed that latent heating was an important mechanism for the development of the mesovortex. In the following experiments, we test the role of the timing of the latent heating during the simulated storm development, in creating conditions leading to the observed mesovortex.

Similar to the LH_OFF, no LLJ is present, nor does a cyclonic circulation form during the time period that the mesovortex was observed in the LHON_LHOFF experiment (Figure 3.11d and Figure 3.12d). This test showed that the precipitation on the prior day, and any other

processes that set up the environmental thermodynamic conditions for the day being studied, were not the primary factors responsible for the development of the mesovortex or LLJ.

Testing the importance of the precipitation on the same day as the circulation developed, LHOFF_LHON has the latent heating turned off until 1800 UTC 11 September, after which it is turned on. At 0300 UTC 12 September, there is a small area of PV in northern Boulder County with an associated easterly LLJ northeast of the mesovortex along the eastern border of Larimer County (Figure 3.11c). The areal coverage of the PV is not as large as that of the control simulation at the same time, but the features are somewhat similar (e.g. hints of a cyclonic circulation are seen and the associated LLJ). By 0600 UTC, the LLJ is gone and the small areas of PV have moved west (Figure 3.12c). Although the PV in LHOFF_LHON is not as high and it dissipates earlier compared to the control, features similar to those of the mesovortex are seen. These results demonstrate that latent heat release is required for a vortex to develop on 12 September. Specifically, the latent heat released on the second day is crucial for the development of the circulation, whereas the latent heating on the day prior plays a lesser role. The LLJ and vortex setup in LHOFF_LHON is similar to that found in LH_ON, but is instead shifted to the northeast. Due to this location, the westward progression of the vortex results in enhanced upslope flow farther north. This leads to higher values of reflectivity in Larimer County (Figure 3.13).

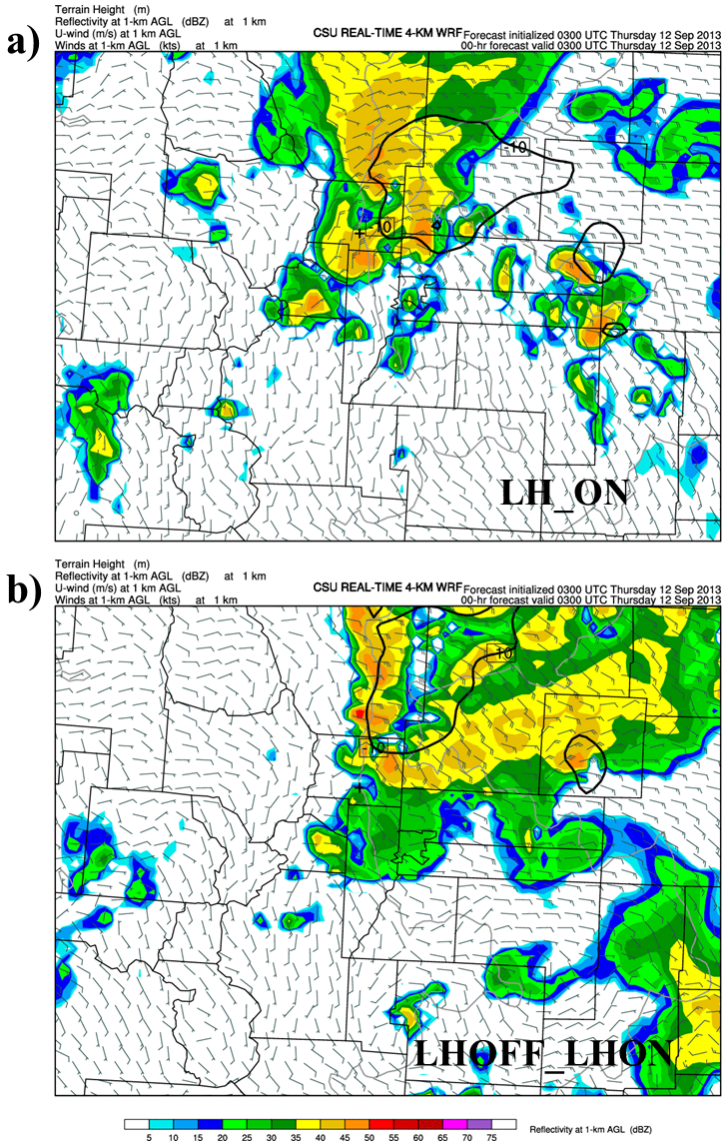

Figure 3.13: Radar reflectivity (dBZ; color filled), negative u-wind (m/s, solid black contour), and wind barbs (kts) all at 1 km AGL for 0300 UTC September 12.
(a) Control (LH_ON) and (b) LHOFF_LHON simulations. U-wind contour interval is 5 m/s, starting at -10 m/s. A marker "+" is provided for reference and denotes the location of Boulder, CO.

3.2.3 LH Feedback Mechanism

The experiments shown in the previous subsection demonstrate that the easterly LLJ over northern Colorado was enhanced in response to the upward motions caused by the large amounts

of latent heat release in convective areas. A similar result was found in a study by Lackmann (2002) which found interdependence between PV maxima and the LLJ in the warm sector of an extratropical cyclone, with the former contributing 15% to 40% to the strength of the latter. Results from the LH experiments in our study suggest that the near-surface flow responds to the release of latent heat, therefore a change in its distribution will have corresponding changes to the flow (LLJ and mesovortex) i.e. more latent heat release, more upward motion, stronger LLJ, enhanced upslope flow, more convection, and so on. These changes will in turn heavily impact the surface precipitation, as demonstrated in Figure 3.13.

3.3 Analysis of Latent Heating Profiles

As described earlier, convective and stratiform regions of precipitation have different vertical profiles of latent heating. These profiles can provide information about when and where a positive vertical gradient in latent heating occurred, leading to the concentration of PV (positive PV anomaly) and its associated cyclonic circulation. Profiles with convective characteristics would be more favorable for producing such a circulation near the surface, where it can interact with the complex terrain and lead to strong upslope flow.

To further explore latent heating and its role in the production of PV anomalies, vertical profiles of domain-averaged accumulated latent heating (due to all microphysical processes, which are broken out separately in the next section) were analyzed. The domain over which the horizontal averaging is calculated is shown as the red dashed box in Figure 1.1. Figure 3.14 shows vertical profiles of latent heating and PV representative of each day in the simulation. During the first round of precipitation (as described in Section 2.3.1) on 11 September, the heating profile has a peak in latent heating near 5.5 km MSL. As expected, higher PV is located where we find a positive vertical gradient in latent heating (Figure 3.14g). Similarly, on 12

September during which the mesoscale vortex had developed and moved over Boulder, the latent heating profile has a peak below 6 km MSL (Figure 3.14e), broader and higher in magnitude than the previous day. The low cloud base (unusually low for Colorado) would be expected to shift the condensational heating closer to the surface, leading to lower-altitude heating peaks than those found in an MCS. The PV profile shows high values of PV nearer the surface (~3 km MSL) (Figure 3.14h). This strong, positive, low-altitude vertical gradient in latent heating is believed to have induced the higher values in PV. During both these days, the radar reflectivity values were high (>40 dBZ; Figure 3.14), typical of a more convective environment. Domain-averaged hourly accumulated precipitation and vertical velocity at a height of ~5 km show generally higher amounts of precipitation and stronger updrafts (Figure 3.15), characteristics supporting more convective precipitation.

The precipitation on the third day (13 September) has heating characteristics much different than those during the first two days. The heating profile shows a peak aloft (~9 km MSL), cooling at mid-levels (6 km MSL), and a secondary peak near the surface (~3 km MSL) (Figure 3.14f). Simulated radar reflectivity shows more stratiform rain (weaker reflectivity values) within the domain on this day (Figure 3.14c), which is supported with weaker vertical velocities and less accumulated precipitation towards the end of the simulation (Figure 3.15).

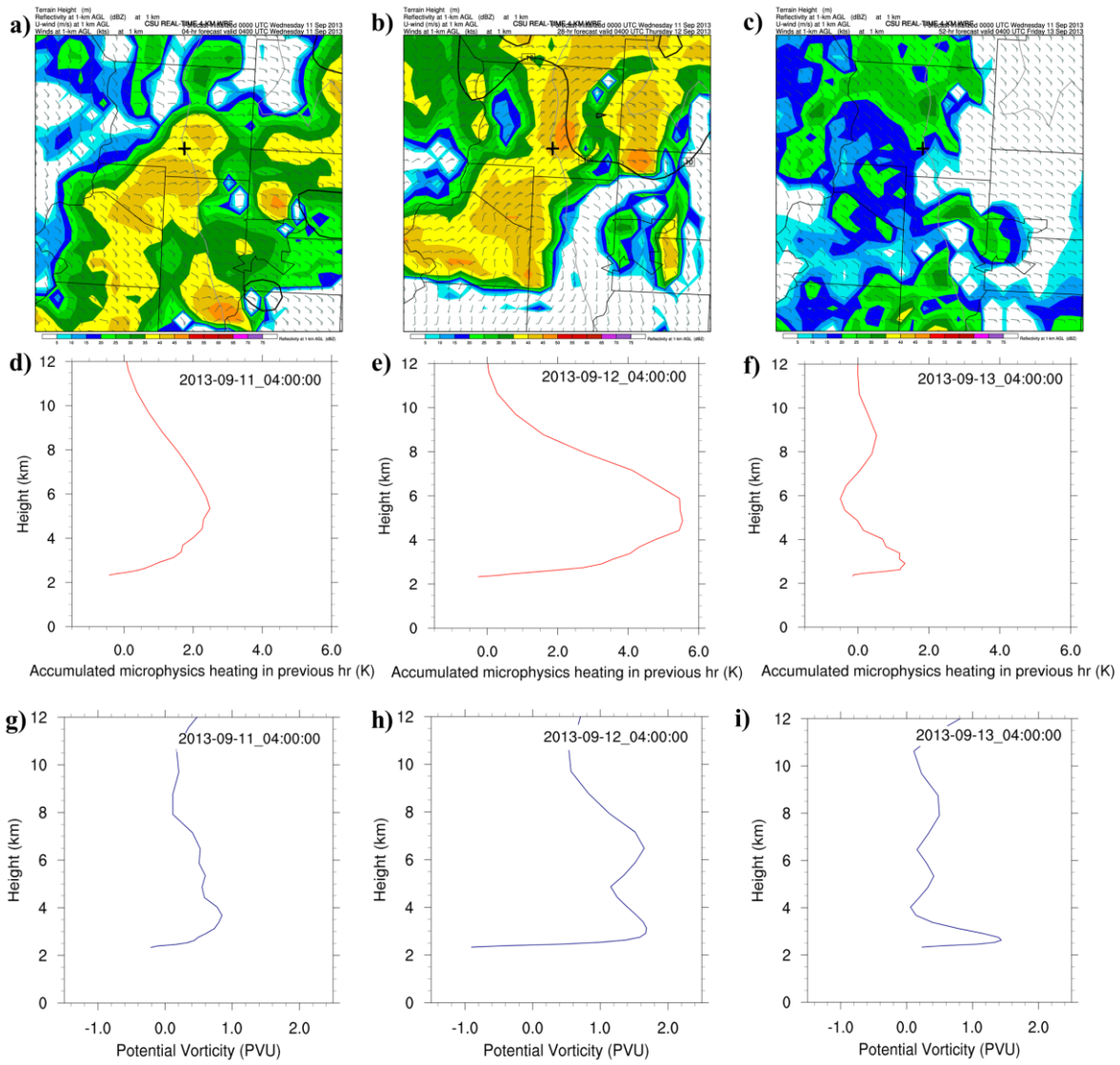

Figure 3.14: Simulated radar reflectivity, u-wind, and wind barbs at 1 km AGL (a-c; similar to Figure 3.13, except for a smaller domain), (d-f) domain-averaged vertical profiles of accumulated microphysics heating for the previous hour in the simulation (K), and (g-i) horizontally averaged vertical profiles of potential vorticity (PVU).
Left panels are at 0400 UTC 11 September, middle panels are at 0400 UTC 12 September, and right panels are at 0400 UTC 13 September. Vertical axis for profiles is geopotential height (km MSL). Accumulated microphysics heating and PV are averaged over the red dashed box in Figure 1.1. The "+" marker denotes the city of Boulder.

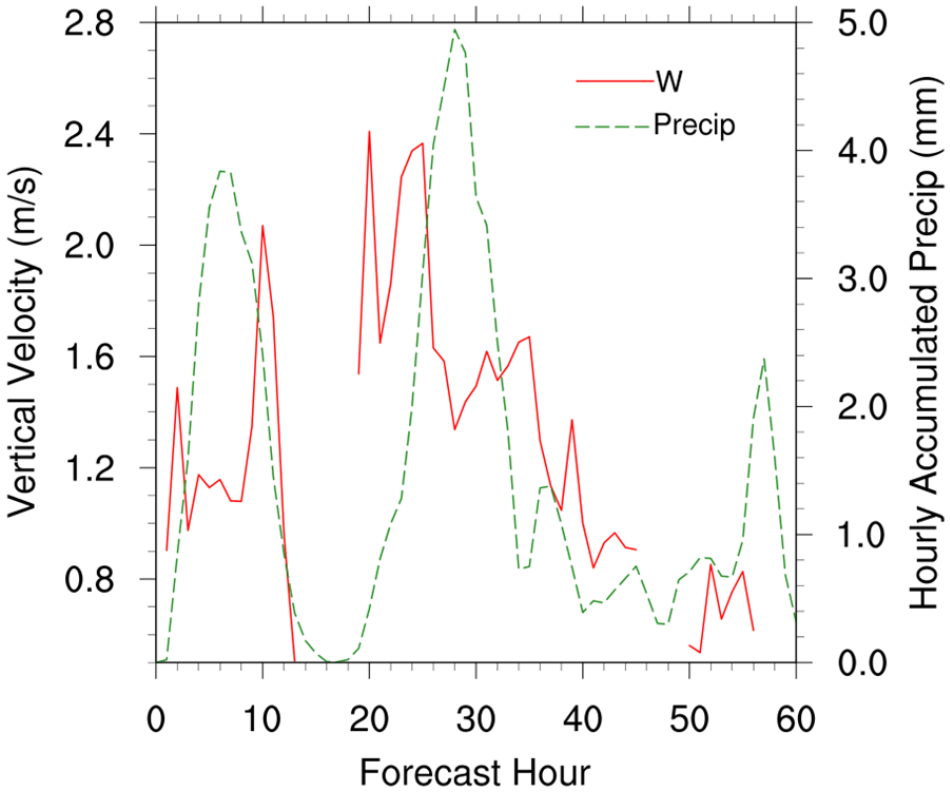

Figure 3.15: Time series of vertical velocity and hourly accumulated rain for control simulation. Both vertical velocity (m/s; red solid line) and hourly accumulated rain at the surface (mm) are domain-averaged for the area denoted in Figure 1.1 with a red dashed box. Vertical velocity is averaged at a height of approximately 5 km MSL for values greater than 0.5 m/s (y-axis origin is 0.5 m/s). Missing vertical velocity values are less than 0.5 m/s and thus, are excluded from the analysis. Horizontal axis is the forecast hour initialized at 0000 UTC 11 September 2013 and ending on 1200 UTC 13 September 2013.

Figure 3.16 shows more details of the temporal evolution of latent heating/cooling and PV during the simulation. The two periods of convective precipitation seen in the vertical profiles are shown in Figure 3.16 as maxima in latent heating in the mid-troposphere. The overall latent heating on 12 September extends further down to approximately 2.5 km MSL and has a longer duration compared to 11 September. As described above, the latent heating on 12 September was stronger and had a downward shift compared to 11 September, resulting in a stronger vertical gradient and more PV. From 0000-0600 UTC 12 September (forecast hours 24-

30), when the mesovortex developed and moved towards Boulder, a maximum in PV near 3 km MSL is found in association with this vertical gradient in heating (Figure 3.16). Note the PV maximum in the vertical cross-section in Figure 3.10b is more uniform between 3-6 km MSL, while in Figure 3.16 it shows up at 3 km MSL (most likely due to the horizontal averaging performed in Figure 3.16). The stratiform regime on 13 September is also shown in Figure 3.16 with much smaller values of latent heating and a double maximum aloft and near the surface. The lack of strong latent cooling during the convective regimes demonstrates the moist environment reducing the capability for rain evaporation. During the stratiform regime, relatively higher values of cooling were seen below 2.5 km MSL, mainly from rain evaporation.

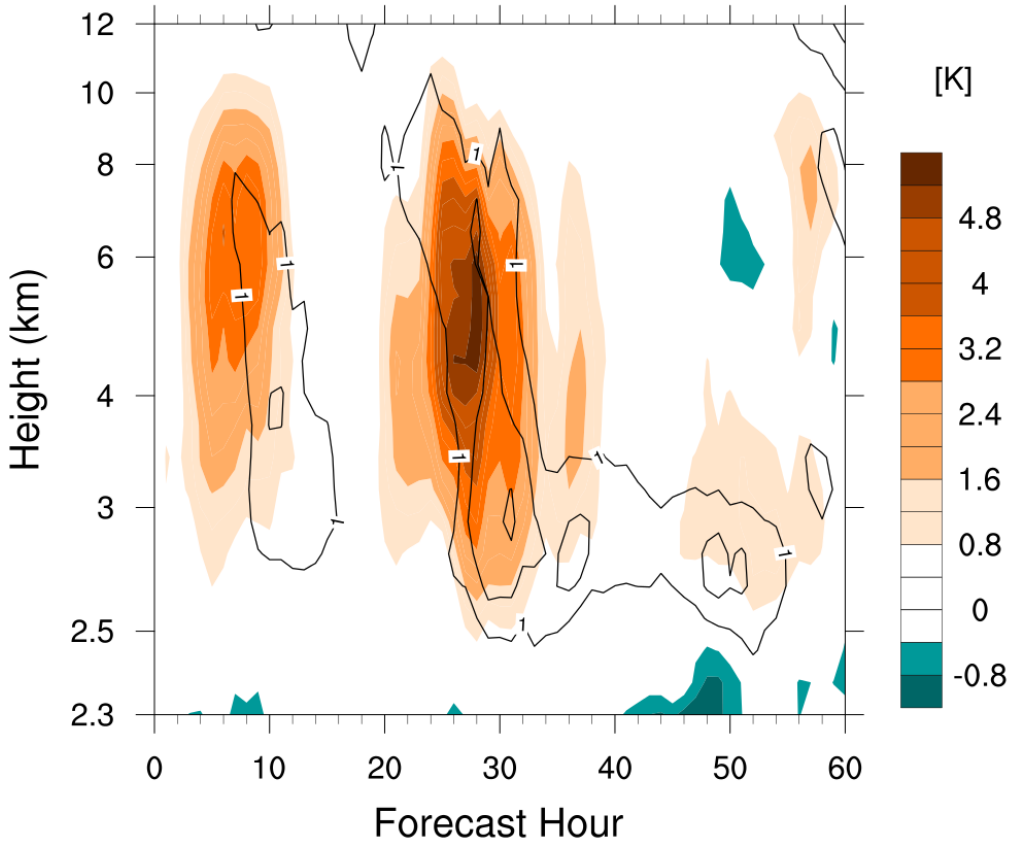

Figure 3.16: Time-height plot of accumulated microphysics heating (K; color-fill) and potential vorticity (PVU; black contours) for every forecast hour starting at 0000 UTC September 11. Potential vorticity contour interval is 0.5 PVU from 1 to 2 PVU. The vertical axis is geopotential height (km MSL).

The results of this latent heating analysis for the control simulation show that the first two days had more convective characteristics compared to the third day, which was more stratiform. This conclusion is supported by the vertical velocity analysis in Figure 3.15, where the first two days had stronger updrafts. The mesovortex formed within the strong vertical gradient in latent heating in the lower troposphere on day 2. These results suggest that the cyclonic circulation observed from 0000-0600 UTC 12 September was formed through processes similar to those that form an MCV, as described by Raymond and Jiang (1990).

3.4 Contributions of Various Microphysical Processes to Latent Heating

The latent heating analysis described above includes various microphysical processes (e.g. condensation, deposition, melting, freezing) for different species (i.e. snow, cloud ice, cloud water, rain, and graupel). To further understand the contributions of different microphysical processes to the total latent heating, an analysis separating their contributions was performed here. Vertical profiles of domain-averaged heating for the "bulk" processes of sublimation/deposition, freezing, melting, condensation/evaporation, and instantaneous freezing/melting are analyzed. A description of the individual processes summed to produce each bulk term can be found in Appendix B.

During the period from 0000-0600 UTC 12 September, condensation determines where the main peak in latent heat will be located vertically (Figure 3.17). Latent heating due to this microphysical process is much larger than the others and dominates below 6 km MSL. Rain evaporation, melting (mostly graupel), and sublimation act to decrease the heating values and change the shape of the profile. Freezing adds latent heat to the profile, sometimes helping to shift the peak in latent heat upward, higher than the condensation peak. Due to this combination of latent heat contributions, double peaks occur within the main peak (Figure 3.17b,d).

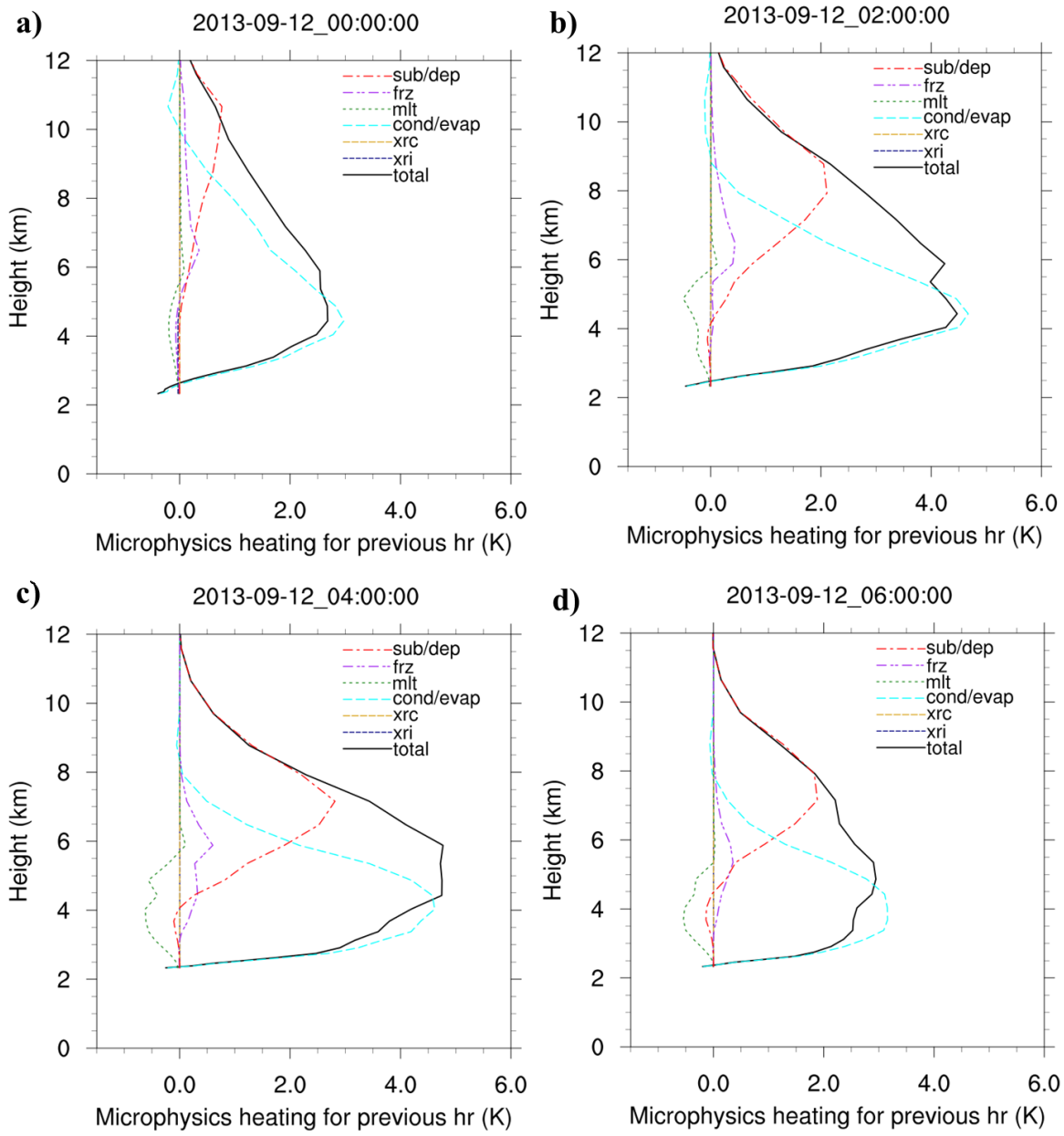

Figure 3.17: Vertical profiles of domain-averaged hourly accumulated microphysics heating (K) for each "bulk" microphysics term.

The profiles are for 12 September 2013 at (a) 0000 UTC, (b) 0200 UTC, (c) 0400 UTC, and (d) 0600 UTC. The accumulated microphysics heating is horizontally-averaged over the domain outlined in Figure 1.1. The bulk microphysics terms are: sublimation/deposition ("sub/dep"; red), freezing ("frz"; purple), melting ("mlt"; green"), condensation/evaporation ("cond/evap"; cyan), instantaneous freezing of cloud water ("xrc"; gold) and melting of cloud ice ("xri"; navy), and the sum of all the terms ("total"; black solid). The vertical axis is geopotential height (km MSL). The processes within each bulk term can be found in Appendix B.

Above 6 km MSL, vapor deposition, mostly to snow, dominates the contribution to latent heating. This result is not too surprising, considering there was much more snow relative to cloud ice within the control simulation (Figure 3.18).

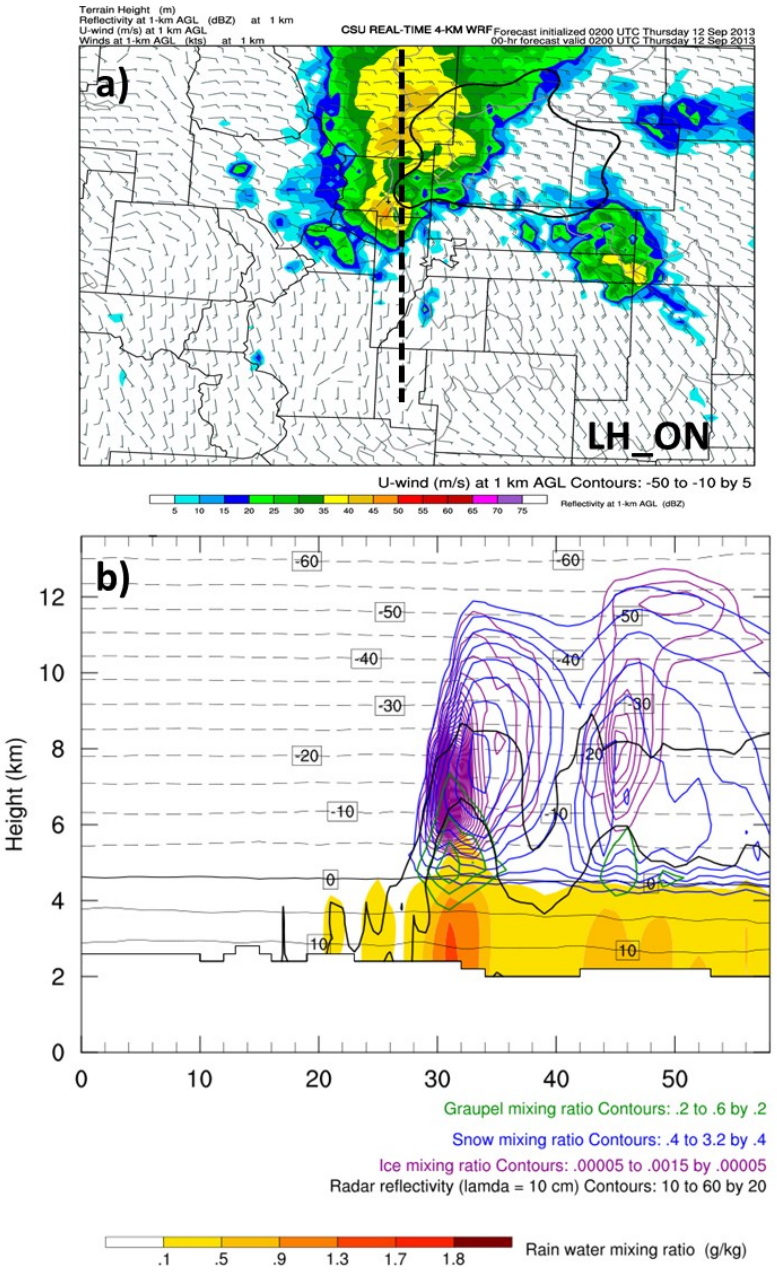

Figure 3.18: Horizontal map of reflectivity at 1 km AGL and vertical cross-section of hydrometeor mixing ratios.

Time-averaged values for 0200-0600 UTC 12 September: (a) same as in Figure 3.13, (b) south-to-north vertical cross-section [denoted by dashed black line in (a)] of mixing ratios for graupel (kg/kg; green contours), snow (kg/kg; blue contours), cloud ice (kg/kg; purple contours), and rain (kg/kg; color filled) (PVU; color filled), radar reflectivity (dBZ; black contours), and temperature (°C; gray lines). Radar reflectivity contour interval is 10 dBZ, labeled at an interval of 20 dBz; temperature contour interval is 5°C labeled at an interval of 10°C; vertical axis is height in km MSL and horizontal axis is number of grid points along location of cross-section in (a).

Focusing on the bulk condensation/evaporation term, which dominates the heating near the surface, each individual microphysical process contributing to this term is analyzed in Figure 3.19. Condensation of cloud water is the dominant process within this bulk term. Rain evaporation is much weaker than condensation during this time period, which helps in the preservation of this strong vertical gradient near the surface. Cloud water evaporation, peaking near 5 km MSL (i.e., just above the 0°C level), may be related to the Bergeron-Findeisen process by which ice or rimed particles grow at the expense of liquid particles.

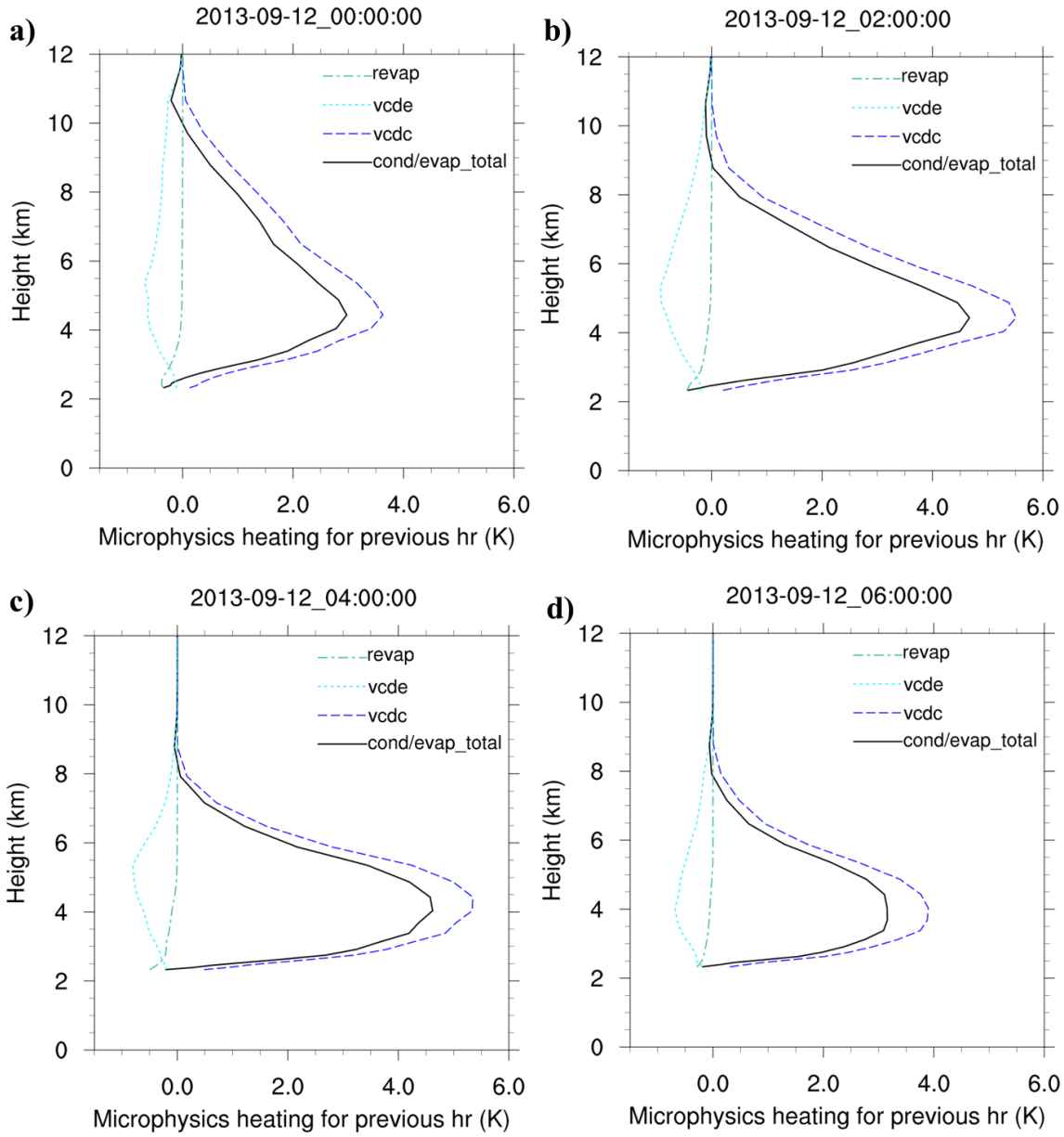

Figure 3.19: Vertical profiles of domain-averaged hourly accumulated microphysics heating (K) for the "cond/evap" term from Figure 3.17.
The profiles are for 12 September 2013 at (a) 0000 UTC, (b) 0200 UTC, (c) 0400 UTC, and (d) 0600 UTC. The accumulated microphysics heating is horizontally-averaged over the domain outlined in Figure 1.1. The processes contained in the "cond/evap" term from Figure 3.17 are: rain evaporation ("revap"; turquoise dash-dot), cloud water evaporation ("vcde"; cyan short dashes), cloud water condensation ("vcdc"; blue long dashes"), and the sum of these terms ("cond/evap"; black solid). The vertical axis is geopotential height (km MSL).

The results described here suggest that condensational growth of cloud water and low rain evaporation help to keep the positive vertical gradient in latent heating strong in the lower troposphere. Due to the large amounts of cloud water condensation near the surface (partially as a result of the low LCL height), the maximum in latent heating occurred at lower altitude than typically observed during a strong deep convective storm (CAPE on the order of 1000 J/kg). This shift helped position the PV closer to the surface, where a cyclonic circulation could form and enhance upslope flow of moist air.

3.5 Sensitivity to Strength of Latent Heating

The experiments and analysis described in the previous subsections have all suggested the importance of latent heating, in particular the latent heat released by cloud water condensation. To test the sensitivity of the mesovortex to the latent heating contribution from condensation, the heating was reduced by 50% after 1800 UTC 11 September by adjusting the physical constant directly (energy released per unit mass of water condensed), but allowing the same mass to condense. This experiment (herein LHON_LHHALF) resulted in no mesovortex development (Figure 3.20a), neither at 0600 UTC 12 September (as seen in the control) nor at any other time during the simulation. The flow was still from the southeast, but there was no easterly LLJ seen in this simulation. Again, we see the strong relationship between latent heat release and the overall flow, as described in section 3.2.3. The simulated radar reflectivity at 0600 UTC 12 September shows precipitation over eastern Larimer County and northeast of Boulder with reflectivity values up to 35 dBZ (Figure 3.20b), weaker than in the control simulation (Figure 3.5f).

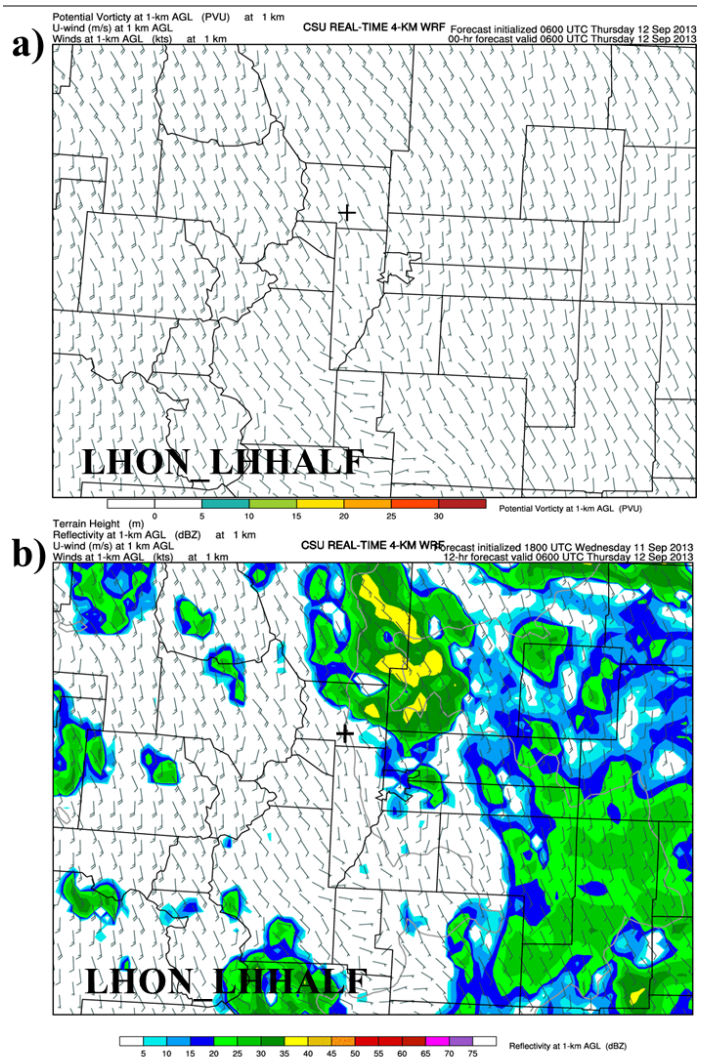

Figure 3.20: (a) Potential vorticity (same as Figure 3.11) and (b) radar reflectivity (same as Figure 3.13), both for 0600 UTC 12 September for the LHON_LHHALF experiment.

The 24 hr accumulated precipitation valid at 1200 UTC 12 September was substantially less than that for the control simulation (over 100 mm difference; Figure 3.21). This result suggests that the easterly LLJ associated with the mesovortex played a large role in the amount of precipitation that fell on 12 September. Clearly, reducing the amount of latent heating near the surface affected the development of both the mesovortex and LLJ.

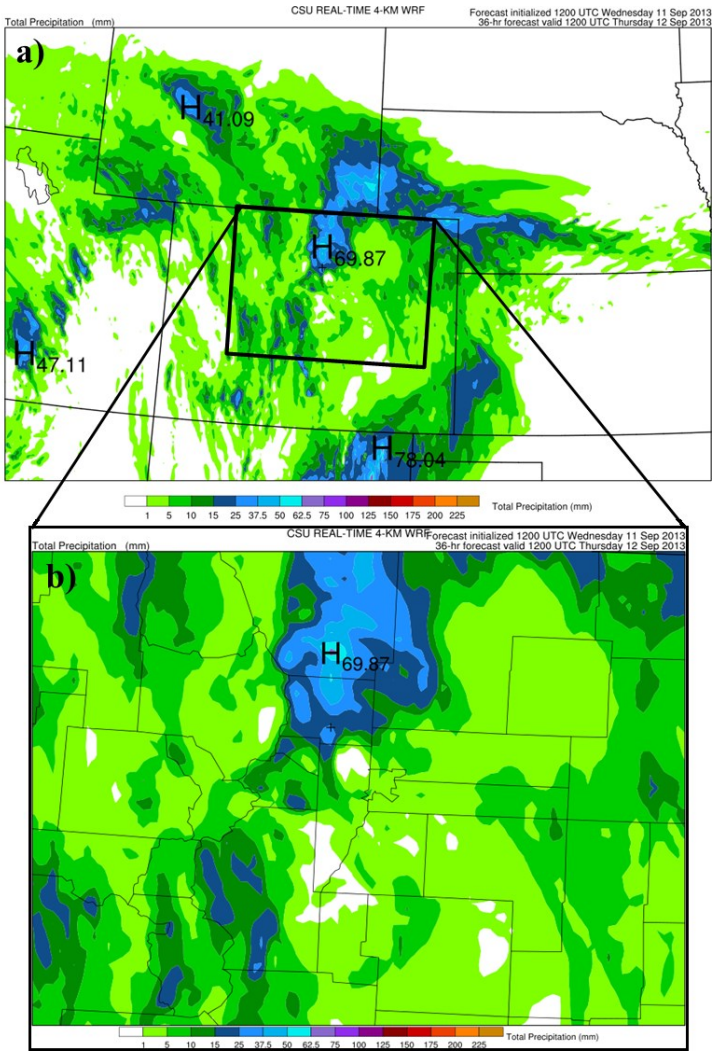

Figure 3.21: (a) 24 hr accumulated precipitation (mm) valid at 1200 UTC 12 September with (b) zoomed in section focusing over northern Colorado for the LHON_LHHALF. High precipitation value in zoomed in section is 69.87 mm.

The reduced latent heating from cloud water condensation severely reduced the overall heating, both near the surface and aloft during the 00-06 UTC 12 September (forecast hours 24-30) (Figure 3.23). The lack of a strong, positive vertical gradient in LH seems to have inhibited the generation of PV near the surface (Figure 3.23), thus impacting the development of the mesovortex. Because of the positive feedback associated with the mesovortex/LLJ and

convection, there was no enhancement of convection or precipitation from enhanced upslope flow caused by the LLJ.

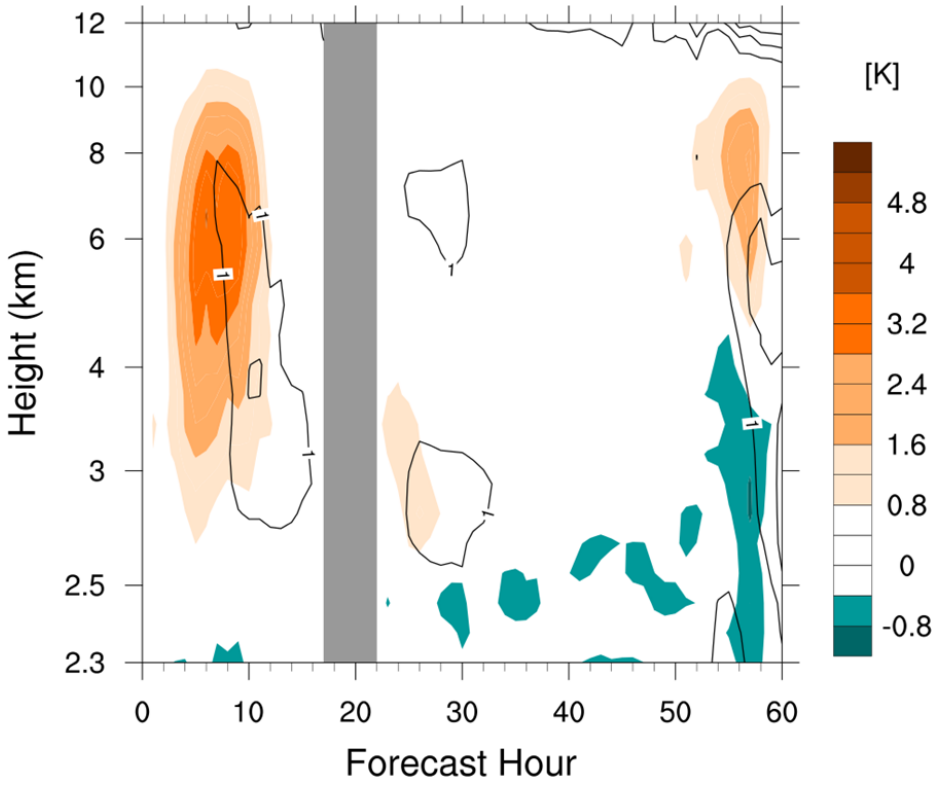

Figure 3.22: Time-height plot of accumulated microphysics heating and PV for LHON_LHHALF (same as Figure 3.16).
The gray vertical bar represents the adjustment period of the model to the reduction in latent heating; these values are neglected in the analysis. Essentially, data to the left of the gray bar is associated with the control and data to the right of the gray bar is associated with reduced latent heating.

The lack of strong heating aloft (Figure 3.23 and Figure 3.23) suggest that the vertical velocities during the time the latent heating was reduced would have been much weaker than during the control simulation (Figure 3.24). Weaker updrafts would not be able to transport much moisture aloft to either freeze or deposit into snow and cloud ice.

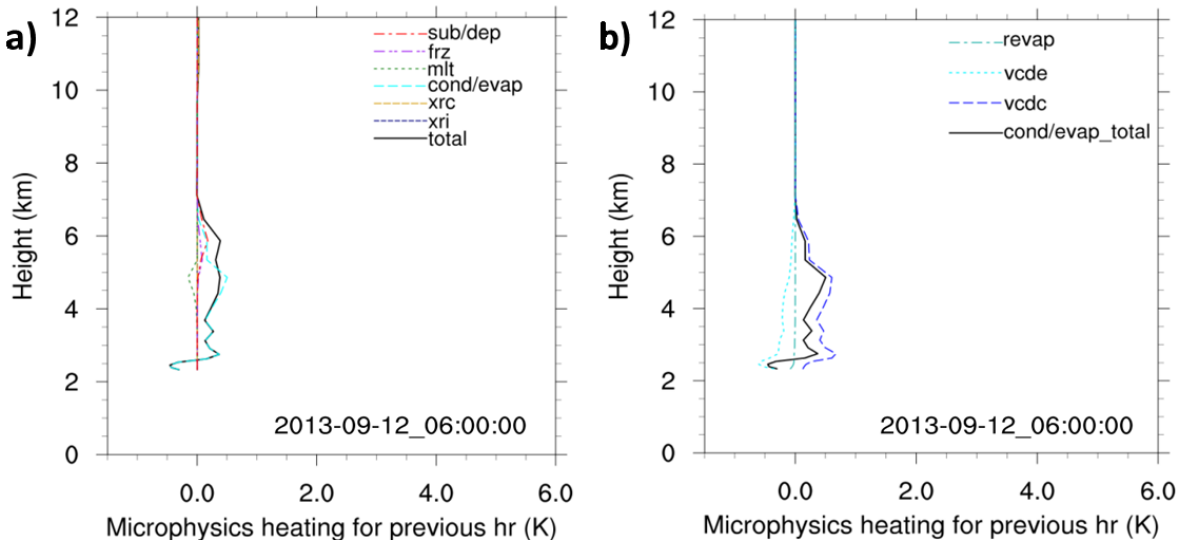

Figure 3.23: Vertical profiles of microphysics heating at 0600 UTC 12 September for LHON_LHHALF, where (a) is same as Figure 3.17 and (b) is same as Figure 3.19.

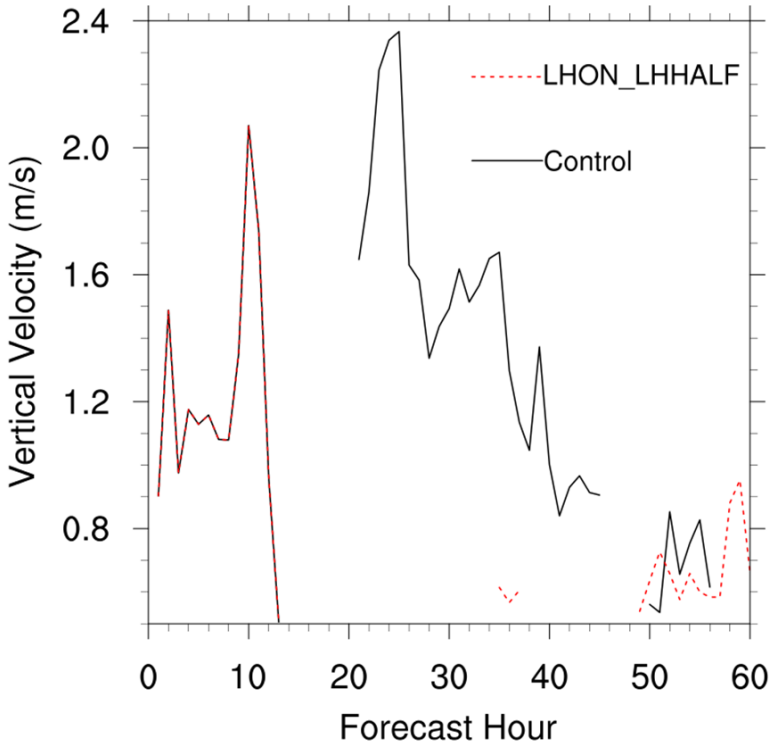

Figure 3.24: Time series of vertical velocity for LHON_LHHALF and control simulations. Same as Figure 3.15, but does not include hourly accumulated rain. Missing vertical velocity values are less than 0.5 m/s and thus, are excluded from the analysis.

4. Summary and Conclusions

4.1 Summary of Presented Results

A slow-moving low pressure system and record amounts of moisture in Colorado from 9-16 September 2013 led to heavy precipitation and flooding over a large portion of the state. Between 00-06 UTC on 12 September, a mesovortex formed near Denver, CO and moved north-northwest towards Boulder, CO. This cyclonic circulation caused an enhancement to upslope flow resulting in an increase in precipitation, adding more rain to already overwhelmed rivers and streams.

To properly model the observed mesovortex, this study used the ARW model with a configuration similar to that of an ensemble member from the CSU ARW ensemble that forecasted precipitation the best. Although precipitation amount was under predicted with this configuration, the spatial distribution of the precipitation was overall well represented. This configuration performed well in properly simulating the mesovortex of interest, which allowed for further exploration of the circulation's characteristics in lieu of observations.

This control simulation was then used to run several experiments where latent heating from microphysical processes was turned off for all or part of the forecast period. The goal of these experiments was to determine the importance of latent heat release to the development of the observed mesovortex. Turning off latent heating for the entire simulation resulted in no mesovortex developing, thus suggesting that latent heat release and *not* lee vortex formation was responsible for the circulation on 12 September. Further experiments showed that latent heat released just before and during the mesovortex event played a larger role than that on the day prior. These experiments also showed that latent heating had a strong effect on the surface flow

field, resulting from a positive feedback mechanism described by Lackmann (2002). This feedback led to increased convection, which then released more latent heat leading to further enhancement in upslope flow.

Using the control simulation to further understand the environment that formed the mesovortex, an analysis of vertical latent heating profiles found that high values of PV near the surface were associated with a strong, positive vertical gradient in latent heating located in the lower troposphere. This type of vertical profile is characteristic of a convective precipitation regime, which was supported with higher radar reflectivity echoes and stronger vertical velocities observed during 12 September. The effect of latent heat on PV generation here is analogous to the maintenance of MCSs as described by Raymond and Jiang (1990). Essentially, latent heating within convective regions produces a positive PV anomaly below the source of latent heat release where a cyclonic circulation then forms around this anomaly. The results suggest that this mechanism was responsible for the development of the mesovortex observed during 00-06 UTC 12 September.

Further analysis of the latent heating profiles found that condensation of cloud water was the dominant process responsible for the positive vertical gradient in latent heating near the surface. The lack of high rain evaporation near the surface also helped to keep the vertical gradient strong on 12 September. Deposition to snow was important for latent heat release aloft. To further explore the sensitivity to the strength of the latent heating from this dominant microphysical process, an experiment was performed where the latent heating contribution from cloud water condensation was reduced by 50% after 1800 UTC 11 September, by simply adjusting the physical parameter describing the energy released per unit mass of vapor converted to liquid, leaving the rate of mass condensation unaffected. This sensitivity study showed that

this degree of reduction in latent heating from condensation resulted in no mesovortex development and a significant reduction in precipitation along the northern Front Range of Colorado. Taken together, the simulations and sensitivity studies suggest that the mesovortex was indeed responsible for the increased rain rates observed on 12 September.

4.2 Implications

The results from this study demonstrate the important role microphysical processes play in the development of mesoscale features, such as the mesovortex studied here. Condensation of cloud water closer to the surface (due to low-altitude cloud base) led to the development of a strong, positive vertical gradient in latent heating, which was responsible for the generation of PV and its associated cyclonic circulation. This mesovortex was shown to have a strong impact on the amount of precipitation that resulted in flash flooding over Boulder on 12 September. These results suggest that the representation of microphysics may affect the ability of an operational NWP model to generate such a mesovortex and any subsequent environmental and hydrological impacts.

Within the ARW model, there are over a dozen microphysics parameterizations (Skamarock et al. 2008) and each of these packages handles the microphysical processes in a different way. Some of the microphysics packages may not be able to capture the evolution and development of the mesovortex; either due to their representation of physical processes, particle size distributions, or choice of prescribed parameters (e.g. cloud droplet number concentration, particle density, and intercept parameter). A particular microphysics scheme might have a tendency to convert cloud water to rain too quickly, thus actively removing these particles. With these particles no longer available to scavenge water vapor, the release of energy from condensation could possibly be maximized at the wrong time and wrong altitude, ultimately

leading to an improper representation of a mesovortex. Although the environment in this case was very moist, inhibiting much rain evaporation, a microphysics scheme that tends to have more rain evaporation can change the strength and location of the vertical heating gradient and thus, affect the development and position of a mesovortex. Rain evaporation can also be effected by drop size, which can be related to the growth mechanism, i.e. rain drops formed through melting of ice species would tend to be larger than those grown through collision-coalescence.

Studies have shown that sensitivities of deep convection and surface precipitation to ice microphysics exist (McCumber et al. 1991; Gilmore et al. 2004; Bryan and Morrison 2012; Van Weverberg et al. 2012). Gilmore et al. (2004b) found that for a small-graupel regime, fusion, deposition, and net condensation heating is larger compared to a large-hail regime. Van Weverberg et al. (2012) found that depositional growth and low precipitation efficiency dominate the Morrison scheme, while a different scheme (Milbrandt-Yau, also available in ARW) is dominated by riming processes and high precipitation efficiency. The energy released through deposition is an order of magnitude larger than that for freezing (riming), thus the Morrison scheme would have higher latent heating than Milbrandt-Yau.

This work, in addition to past studies, demonstrates that the rainfall forecast is closely tied to the representation of microphysical processes. Here, these microphysical processes have been found to have a physical/dynamical connection to the mesovortex and LLJ that formed during the extreme precipitation event. These relationships are therefore relevant to NWP/forecasting based on a lack of understanding of the mechanisms, timing, and location of where these mesoscale features develop, and because of their suggested association with high rain rates.

4.3 Future Work

Results from NWP models are known to be sensitive to horizontal grid spacing (Weisman et al. 1997; Bélair and Mailhot 2001; Petch et al. 2002; Adlerman and Droegemeier 2002; Bryan et al. 2003; Bryan and Morrison 2012). A recent study on the September 2013 Colorado event by Schwartz (2014) found rainfall forecasts along the Front Range for simulations at 1 km grid spacing were more consistent with observations than forecasts at 4 km grid spacing. Thus, future continuation of the research presented here would involve running the control simulation with a higher resolution nest (~1 km horizontal grid spacing) to test that our results are robust.

Further testing on the sensitivity of the mesovortex to the strength of the low-level latent heating will also be performed. A more modest reduction (10%) to the contribution of LH from cloud water condensation will be implemented. This test will follow a similar analysis as presented here to explore if a mesovortex developed and the impact on precipitation.

It is suggested that future work perform a similar analysis on the other CSU ARW ensemble members that did not predict the precipitation as well. Why did these other members perform so poorly? Did they capture a mesovortex? Although recent studies have performed comparisons between global and regional models (Lavers and Villarini 2014; Hamill 2014) and sensitivities to initial conditions and microphysics package (Schwartz 2014), most of these studies focused on verification of precipitation forecasts. Further analysis exploring the mesoscale features of this event for different models and configurations should be performed.

This study briefly explored the impact of using a different microphysics scheme (Morrison) to the development of the mesovortex. Future work could further analyze this simulation in a similar manner as done for the control. For example, an analysis of the heating

profiles for the experimental simulation could be performed to explore a similar relationship between weaker PV and a weaker vertical heating gradient.

This study found that condensation of cloud water played a large role in the lower troposphere, thus further microphysics testing could be performed that alters this process and studies its sensitivity to different parameters (i.e. rimed ice density/fall velocity, etc.). More in depth microphysics research could be performed. For example, one could compare hydrometeor type observations with the model derived hydrometeors to provide insights on what corrections would be needed within the microphysics scheme to better represent the precipitation at the surface (i.e. less snow, more ice, less graupel, etc.). Due to the limited amount of observational data, this type of study may be a challenge.

Although the sensitivity test in this study focused on testing the strength of the heating contribution from cloud water condensation, a similar test could be performed where the contribution of heating from snow deposition aloft would be reduced. From the LHON_LHHALF experiment, we saw a substantial reduction in heating aloft (from snow deposition) due to weaker updrafts caused by a reduction in latent heating near the surface. If the heating aloft were altered, how would that affect the positive vertical gradient in LH near the surface?

Another avenue for future research could be to investigate further examples of these latent heating-generated mesovortices near the surface during extreme precipitation and compare their characteristics and evolution. The results from our study suggest that these mesovortices can play an important role in enhancing convection, which depending on the environmental conditions and the topography with which they interact, could lead to extreme precipitation and flooding. A larger dataset of similarly formed mesovortices could strengthen evidence for this

hypothesis or perhaps invalidate it and suggest additional mechanisms of importance. The capability to forecast high rainfall and flash flooding is of critical importance to decision makers and the public in order to protect life and property.

5. References

Adams, D. K., and A. C. Comrie, 1997: The North American Monsoon. *Bull. Amer. Meteor. Soc.*, **78**, 2197–2213.

Adlerman, E. J., and K. K. Droegemeier, 2002: The sensitivity of numerically simulated cyclic mesocyclogenesis to variations in model physical and computational parameters. *Mon. Wea. Rev.*, **130**, 2671-2691.

Amante, C., and B.W. Eakins, 2009. ETOPO1 1 Arc-Minute Global Relief Model: Procedures, Data Sources and Analysis. NOAA Technical Memorandum NESDIS NGDC-24. National Geophysical Data Center, NOAA. doi:10.7289/V5C8276M [June 10, 2014].

Bartels, D. L., and R. A. Maddox, 1991: Midlevel cyclonic vortices generated by mesoscale convective systems. *Mon. Wea. Rev.,* **119**, 104-118.

———, J. M. Brown, and E. I. Tollerud, 1997: Structure of a midtropospheric vortex induced by a mesoscale convective system. *Mon. Wea. Rev.*, **125**, 193-211.

Bélair, S., and J. Mailhot, 2001: Impact of horizontal resolution on the numerical simulation of a midlatitude squall line: Implicit versus explicit condensation. *Mon. Wea. Rev.*, **129**, 2362-2376.

Blanchard, D. O., and K. W. Howard, 1986: The Denver hailstorm of 13 June 1984. *Bull. Amer. Meteor. Soc.*, **67**, 1123-1131.

Bolinger, B./Colorado Climate Center, cited 2014: Colorado Flood 2013. [Available online at http://coflood2013.colostate.edu/index.html.]

Brown, B.G., R.R. Bullock, C.A. David, J.H. Gotway, M.B. Chapman, A. Takacs, E. Gilleland, K. Manning, J. Mahoney, 2004: New verification approaches for convective weather forecasts. 11th Conf. Aviation, Range, and Aerospace Meteorology, 4-8 Oct 2004, Hyannis, MA.

———, J. C. Wyngaard, and J. M. Fritsch, 2003: Resolution requirements for the simulation of deep moist convection. *Mon. Wea. Rev.*, **131**, 2394-2416.

Bryan, G. and H. Morrison, 2012: Sensitivity of a simulated squall line to horizontal resolution and parameterization of microphysics. *Mon. Wea. Rev.*, **140**, 202-225.

Caracena, F., R. A. Maddox, L. R. Hoxit, and C. F. Chappell, 1979: Mesoanalysis of the Big Thompson Storm. *Mon. Wea. Rev*., **107**(1), 1-17.

Chappell, C. F., 1993: Dissecting the flash flood forecasting problem. Post Print Volume, *Third National Heavy Precipitation Workshop*, NOAA Tech. Memo. NWS ER-87, 293-297.

Chen, F., and J. Dudhia, 2001: Coupling an advanced land-surface/ hydrology model with the Penn State/ NCAR MM5 modeling system. Part I: Model description and implementation.

Mon. Wea. Rev., **129**, 569–585.

Crook, N.A., T.L. Clark, and M.W. Moncrieff, 1990: The Denver Cyclone. Part I: Generation in Low Froude Number Flow. *J. Atmos. Sci.,* **47**, 2725-2742.

Danard, M. B., 1964: On the influence of released latent heat on cyclone development. *J. Appl. Meteor.*, **3**, 27-37.

Davis, C. A., 1997: Mesoscale anticyclonic circulations in the lee of the central Rocky Mountains. *Mon. Wea. Rev.*, **125**, 2838–2855.

Davis, C., B. Brown, and R. Bullock, 2006a: Object-based verification of precipitation forecasts. Part I: Methods and application to mesoscale rain areas. *Mon. Wea. Rev*., **134**, 1772-1784.

Davis, R. S., 2001: Flash Flood Forecast and Detection Methods. *Meteorological Monographs*, **28**, 481–526. doi: http://dx.doi.org/10.1175/0065-9401-28.50.481

Developmental Testbed Center, 2013: MET: Version 4.1 Model Evaluation Tools Users Guide. Available at http://www.dtcenter.org/met/users/docs/overview.php. 168 pp.

Draxler, R.R., and Rolph, G.D., 2013: HYSPLIT (HYbrid Single-Particle Lagrangian Integrated Trajectory) Model access via NOAA ARL READY Website (http://www.arl.noaa.gov/HYSPLIT.php). NOAA Air Resources Laboratory, College Park, MD.

Doswell, C. A., III, H. E. Brooks, and R. A. Maddox, 1996: Flash flood forecasting: An ingredients-based methodology. *Wea. Forecasting*, **11**, 560-581.

Dudhia, J., 1989: Numerical study of convection observed during the winter monsoon experiment using a mesoscale two-dimensional model, *J. Atmos. Sci.,* **46**, 3077–3107.

EQECAT, cited 2014: Colorado floods likely to incur economic cost greater than $2 billion. [Available online at http://www.eqecat.com/catwatch/colorado-floods-likely-to-incur-economiccost-greater-than-2-billion-2013-09-19/.]

Gallus, William A., Richard H. Johnson, 1991: Heat and moisture budgets of an intense midlatitude squall line. *J. Atmos. Sci.*, **48**, 122–146.

Gilmore, M. S., J. M. Straka, and E. N. Rasmussen, 2004a: Precipitation and evolution sensitivity in simulated deep convective storms: Comparisons between liquid-only and simple ice and liquid phase microphysics. *Mon. Wea. Rev.*, **132**, 1897-1916.

———, ———, and ———, 2004b: Precipitation uncertainty due to variations in precipitation particle parameters within simple microphysics scheme. *Mon. Wea. Rev.*, **132**, 2610-2627.

Grell, G. A., and D. Devenyi, 2002: A generalized approach to parameterizing convection combining ensemble and data assimilation techniques. *Geophys. Res. Lett.,* **29**, 1693.

Grigg, N. S., N. J. Doesken, D. M. Frick, M. Grimm, M. Hilmes, T. B. McKee, and K. A. Oltjenbruns, 1999: Fort Collins flood 1997: Comprehensive view of an extreme event. *J. Water Resour. Plann. Manage.*, **125**, 255-262.

Gochis, D., R. Schumacher, and co-authors, 2014: The Great Colorado Flood of September 2013. Manuscript submitted to *Bull. Amer. Meteor. Soc.*, 7 April 2014.

Hamill, T., 2014: Performance of operational model precipitation forecast guidance during the 2013 Colorado Front-Range floods. *Mon. Wea. Rev.* doi:10.1175/MWR-D-14-00007.1, in press.

Hong, S.-Y., Y. Noh, and J. Dudhia, 2006: A new vertical diffusion package with an explicit treatment of entrainment processes. *Mon. Wea. Rev.,* **134**, 2318–2341.

Houze, R. A., 1989: Observed structure of mesoscale convective systems and implications for large-scale heating. *Q. J. R. Meteorol. Soc.*, **115** (487), 425-461.

Johnson, R. H., 1986: Lower-tropospheric warming and drying in tropical mesoscale convective systems: implications for the problem of cumulus parameterization. *J. Meteor. Soc. Japan*, **64**, 721-725.

Johnston, E. C., 1981: Mesoscale vorticity centers induced by mesoscale convective complexes. M. S. thesis, University of Wisconsin, 54 pp.

Lavers, D. A., and G. Villarini, 2013: Were global numerical weather prediction systems capable of forecasting the extreme Colorado rainfall of 9-16 September 2013? *Geophys. Res. Lett.*, **40**, 6405-6410.

Lackmann, G.M., 2002: Cold-frontal potential vorticity maxima, the low-level jet, and moisture transport in extratropical cyclones. *Mon. Wea. Rev.*, **130**, 59-74.

Lin, Y., and K. E. Mitchell, 2005: The NCEP Stage II/IV hourly precipitation analyses: Development and applications. Pre-prints, *19th Conf. on Hydrology*, San Diego, CA, Amer. Meteor. Soc., 1.2. [Available online at http://ams.confex.comams/Annual2005/techprogram/paper_83847.htm.]

Lukas, J. and contributors, 2013: Severe Flooding on the Colorado Front Range: September 2013 Report. CIRES/University of Colorado/NOAA ESRL/Colorado Climate Center. [Available online at http://coflood2013.colostate.edu/docs/wwa_assessment.pdf .]

Maddox, R. A., F. Caracena, L. R. Hoxit, and C. F. Chappell, 1977: Meteorological aspects pf the Big Thompson flash flood of 31 July 1976. NOAA Tech. Rep. ERL 388-APCL 41, 83 pp.

———, L. R. Hoxit, C. F. Chappell, and F. Caracena, 1978: Comparison of meteorological aspects of the Big Thompson and Rapid City flash floods. *Mon. Wea. Rev.*, **106**, 375-389.

———, C. F. Chappell, and L. R. Hoxit, 1979: Synoptic and meso-α scale aspects of flash flood event. *Bull. Amer. Meteor. Soc.*, **60**(2), 115-123.

———, F. Canova, and L. R. Hoxit, 1980: Meteorological characteristics of flash flood events over the western United States. *Mon. Wea. Rev*., **108**, 1866-1877.

Markowski, P., and Y. Richardson, 2010: Mesoscale Convective Complexes. *Mesoscale Meteorology in Midlatitudes*, John Wiley & Sons, Ltd, 265-270.

McCumber, M., W.-K. Tao, J. Simpson, R. Penc, and S.-T. Soong, 1991: Comparison of ice-phase microphysical parameterization schemes using numerical simulations of tropical convection. *J. Appl. Meteorol.*, **30**, 985-1004.

Menard, R. D., and J. M. Fritsch, 1989: A mesoscale convective complex-generated inertially stable warm core vortex. *Mon. Wea. Rev.,* **117**, 1237-1261.

McKee, T. B., and N. J. Doesken, 1997: Final report: Colorado extreme precipitation data study. Climatology Rep. 97-1, Department of Atmospheric Science, Colorado State University, 107 pp.

Mlawer, E. J., S. J. Taubman, P. D. Brown, M. J. Iacono, and S. A. Clough, 1997: Radiative transfer for inhomogeneous atmospheres: RRTM, a validated correlated-k model for the longwave, *J. Geophys. Res*., **102**(D14), 16,663–16,682.

Petch, J. C., A. R. Brown, and M. E. B. Gray, 2002: The impact of horizontal resolution on the simulations of convective development over land. *Q. J. R. Meteorol. Soc.,* **128**, 2031-2044.

Petersen, W. A., L. D. Carey, S. A. Rutledge, J. C. Knievel, N. J. Doesken, R. H. Johnson, T. B. McKee, T. Vonder Haar, and J. F. Weaver, 1999: Mesoscale and radar observations of the Fort Collins Flash Flood of 28 July 1997. *Bull. Amer. Meteor. Soc.*, **80**, 191-216.

Pontrelli, M. D., G. Bryan, and J. M. Fritsch, 1999: The Madison County, Virginia, flash flood of 27 June 1995. *Wea. Forecasting*, **14**, 384-404.

Raymond, D. J., and H. Jiang, 1990: A theory for long-lived mesoscale convective systems. *J. Atmos. Sci.*, **47**, 3067-3077.

Rogers, R. F., and J. M. Fristch, 2001: Surface cyclogenesis from convectively driven amplification of midlevel mesoscale convective vortices. *Mon. Wea. Rev*., **129**, 605-637.

Thompson, G., P. R. Field, R. M. Rasmussen, and W. D. Hall, 2008: Explicit Forecasts of Winter Precipitation Using an Improved Bulk Microphysics Scheme. Part II: Implementation of a New Snow Parameterization. *Mon. Wea. Rev.*, **136**, 5095-5115.

Trier, S. B., C. A. Davis, and J. D. Tuttle, 2000: Long-lived mesoconvective vortices and their environment. Part I: observations from the central United States during the 1998 warm season. *Mon. Wea. Rev.*, **128**, 3376-3395.

Schwartz, C. S., 2014: Reproducing the September 2013 record-breaking rainfall over the Colorado Front Range with High-Resolution WRF forecasts. *Wea. Forecasting*, **29**, 393-402.

Schumacher, R. S., and R. H. Johnson, 2008: Mesoscale processes contributing to extreme rainfall in a midlatitude warm-season flash flood. *Mon. Wea. Rev*., **136**, 3964-3986.

Skamarock, W. C., J. B. Klemp, J. Dudhia, D. O. Gill, D. M. Barker, M. Duda, X.-Y. Huang, W. Wang and J. G. Powers, 2008. A Description of the Advanced Research WRF Version 3. NCAR Technical Note, NCAR/TN-475+STR.

Smolarkiewicz, P. K., and R. Rotunno, 1989: Low Froude number flow past three dimensional obstacles. Part I: Baroclinically generated lee vortices. *J. Atmos. Sci.*, **46**, 1154-1164.

Szoke, E. J., and M. L. Weisman, 1984: A subsynoptic analysis of the Denver tornadoes of 3 June 1981. *Mon. Wea. Rev.*, **112**, 790-808.

———, 1991: Eye of the Denver Cyclone. *Mon. Wea. Rev.*, **119**, 1283-1292.

Van Weverberg, K., A. M. Vogelmann, H. Morrison, and J. A. Milbrandt, 2012: Sensitivity of idealized squall-line simulations to the level of complexity used in two-moment bulk microphysics schemes. *Mon. Wea. Rev.*, **140**, 1883-1907.

Wakimoto, R. M., and J. W. Wilson, 1989: Nonsupercell tornadoes. *Mon. Wea. Rev.*, **117**, 1113-1140.

Weisman, M. L., W. C. Skamarock, and J. B. Klemp, 1997: The resolution dependence of explicitly modeled convective systems. *Mon. Wea. Rev.*, **125**, 527-548.

Wilczak, J.M., and J.W. Glendening, 1988: Observations and mized-layer modeling of a terrain-induced mesoscale gyre: The Denver Cyclone. *Mon. Wea. Rev.*, **116**, 1599-1622.

———, and T. W. Christian, 1990: Case study of an orographically induced mesoscale vortex (Denver Cyclone). *Mon. Wea. Rev*., **118**, 1082-1102.

Young, Quentin, cited 2014: National Guard carries evacuees from Lyons, delivers supplies. The Denver Post. February 11, 2014. [Available online at http://www.denverpost.com/ci_24072743/dam-break-threatens-lyons-residents-warned-go-higher .]

6. Appendix A: Additional Simulations

6.1 Morrison vs Thompson Microphysics Scheme

A simulation (herein referred to as LHON_MORR) using the same configuration as the control, except for using the Morrison microphysics scheme, was performed. This simulation had radar reflectivity located in relatively similar locations compared to the control simulation using Thompson microphysics (Figure 6.1a). The big difference between these simulations was the location and intensity of the mesovortex. Figure 6.1b shows that at 0600 UTC 12 September the region of PV associated with the mesovortex is much weaker than that from the control simulation (Figure 3.9d). The westward low-level jet northwest of the mesovortex does not extend into Boulder and Larimer Counties as it does in the Thompson simulation, leading to more northerly and northwesterly winds along the Front Range near Boulder. This wind direction is not favored for upslope flow, which would enhance convection over the area.

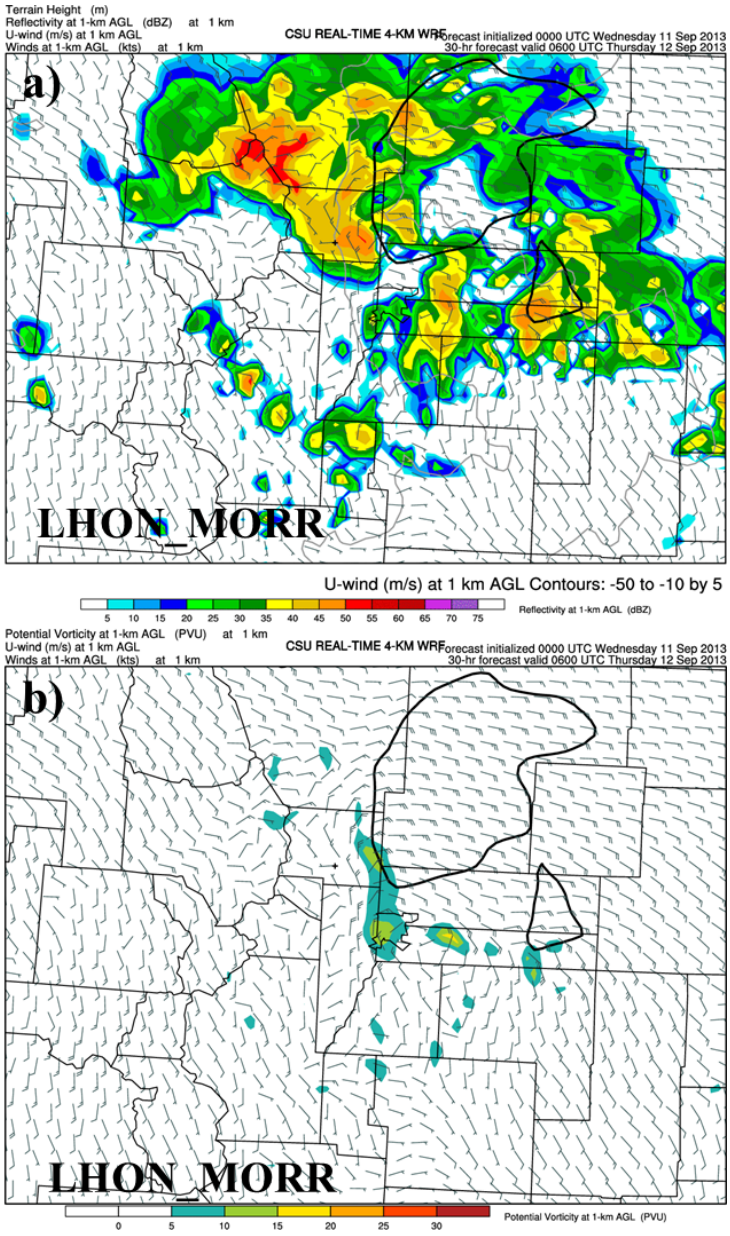

Figure 6.1: (a) Simulated radar reflectivity (same as Figure 3.13) and (b) potential vorticity (same as Figure 3.9) maps at 0600 UTC 12 September for the control simulation with Morrison microphysics.

The surface precipitation is then affected by the location of the mesovortex and associated LLJ. Figure 6.2 shows an eastern shift in precipitation maxima compared to the control simulation with Thompson microphysics. Although the amount of precipitation is more similar to the observed 24 hr total precipitation, the lack of a strong mesovortex and easterly LLJ

over Boulder County in this simulation, key features of the storm that we wished to analyze, led us to choose the configuration with the Thompson microphysics parameterization.

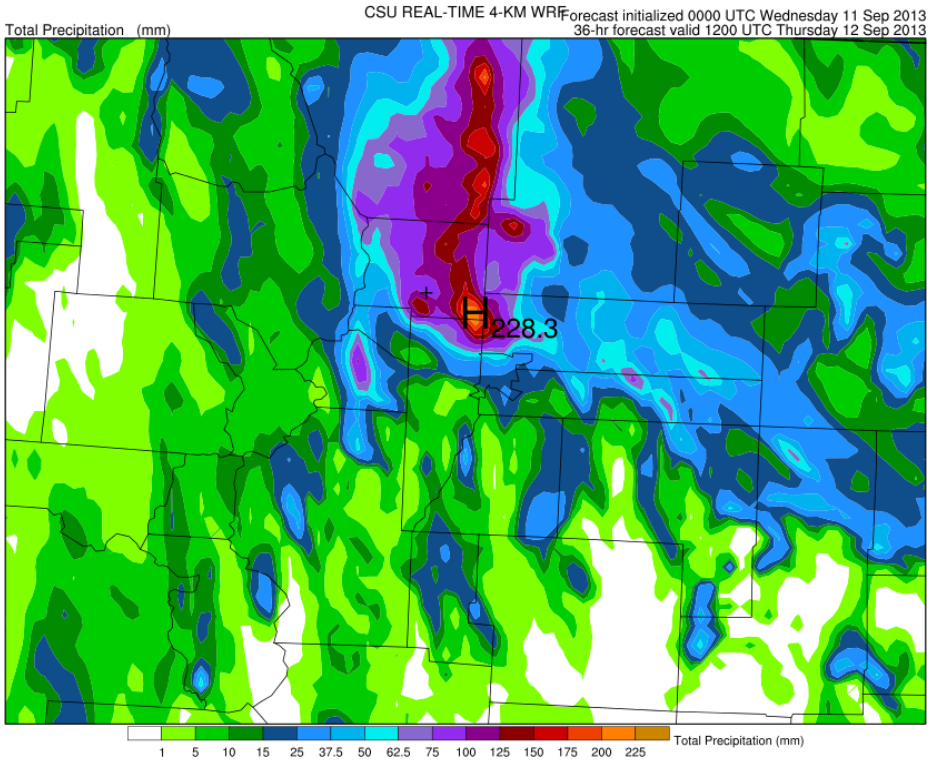

Figure 6.2: 24 hour total precipitation (mm) valid at 1200 UTC 12 September, same as Figure 6.2, but for control simulation using Morrison microphysics scheme.
High precipitation value denoted with an "H" is 228.3 mm. The "+" marker denotes the location of Boulder, CO.

6.2 Reduction of Cloud Droplet Concentration

A simulation with the same configuration as the control, except for a reduction in the cloud droplet concentration (250 cm^{-3} instead of 400 cm^{-3}) was also conducted (herein LHON_250). The droplet concentration for this experiment is the same as is the default in the Morrison microphysics scheme. We hypothesized that reducing the amount of cloud droplets would allow these drops to grow more, leading to earlier autoconversion and/or more efficient collision-coalescence (bigger drops can collect more small drops). This would have an impact on

the amount of surface precipitation, but not necessarily on the vertical gradient in latent heating. The *number* of cloud drops is reduced in LHON_250, not the size (radius), so the condensation rate should not change dramatically. Therefore, vertical gradients in latent heating should not be extremely different from the control. The formation of a mesovortex and LLJ is thus expected with this experiment.

The radar reflectivity at 0600 UTC 12 September (time when vortex was over Boulder in control) is generally similar to the control, with precipitation in north-central Colorado (Figure 6.3a). Over Boulder the radar reflectivity is weaker than in the control, suggesting less precipitation falling at this time. From 0000-0600 UTC 12 September, the reflectivities are generally higher north and east of Boulder (not shown).

The potential vorticity for LHON_250 at 0600 UTC 12 September shows that this experiment did develop a mesovortex and associated LLJ at a similar time as the control simulation (Figure 6.3b). The vortex moves into Boulder about an hour earlier (0500 UTC) and continues to move northwest into Larimer County (not shown). Although there was no inhibition to the circulation's development, the position of the mesovortex was different from the control. Here, the circulation and LLJ are shifted slightly north into Larimer County.

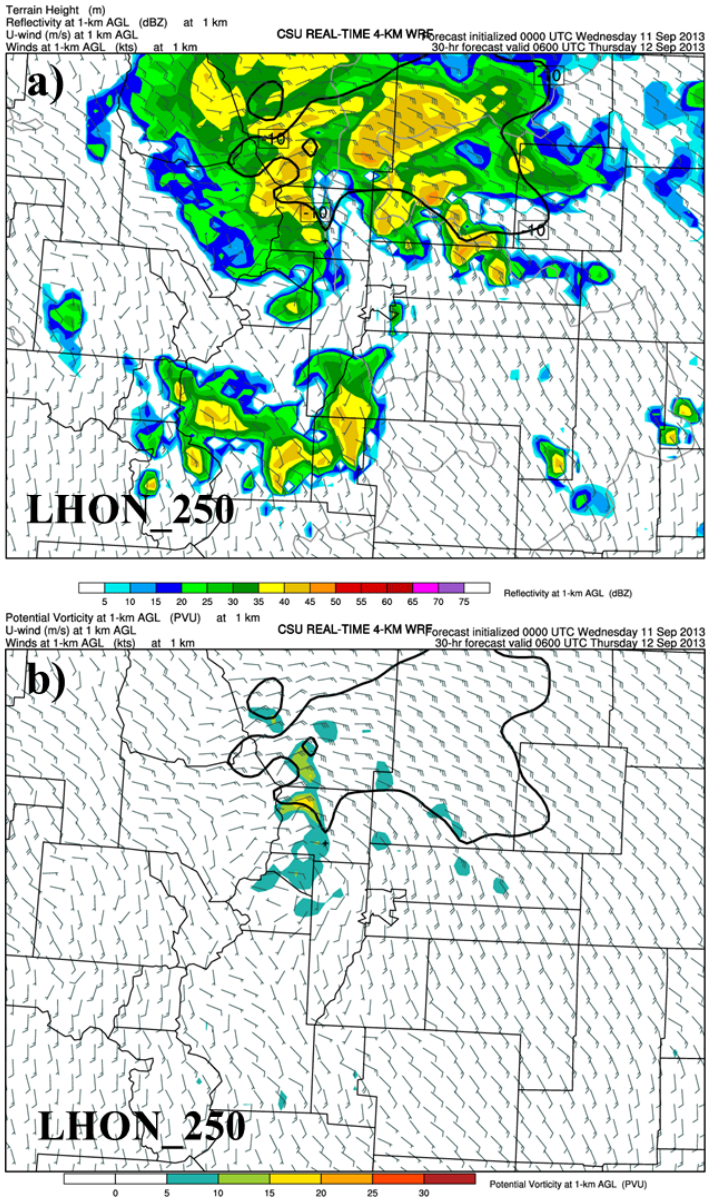

Figure 6.3: (a) Simulated radar reflectivity (same as Figure 3.13) and (b) potential vorticity (same as Figure 3.9) maps at 0600 UTC 12 September for control simulation with reduced cloud droplet concentration (LHON_250).

The slight northern shift in the mesovortex/LLJ seems to be responsible for the higher accumulated precipitation in central Larimer County (Figure 6.4), instead of near Boulder. As expected, the amount of precipitation was higher (~90 mm increase) in LHON_250 than in the control simulation (Figure 3.7d). We conclude that the specified cloud droplet concentration can

have small, but non-trivial effects on the development, motion, and location of the mesovortex and associated precipitation in this case. Thoroughly investigating the reasons for these differences is beyond the scope of this study, but could be considered for future work.

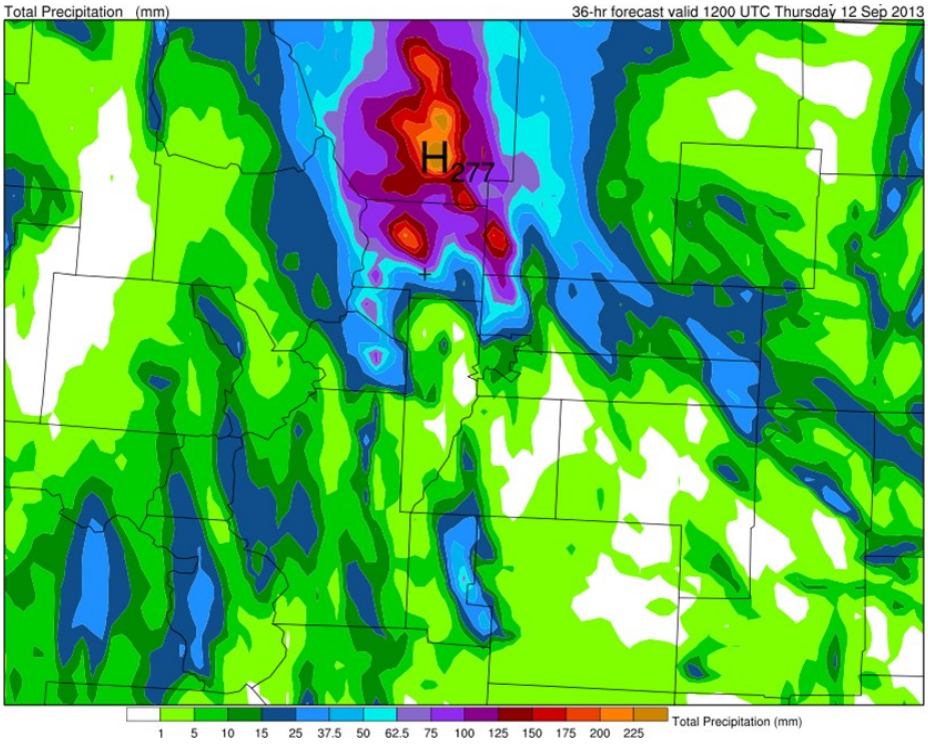

Figure 6.4: 24 hour total precipitation (mm) valid at 1200 UTC 12 September, same as Figure 6.2, but for control simulation using cloud droplet concentration of 250 cm^{-3} (LHON_250). High precipitation value denoted with an "H" is 277 mm. The "+" marker denotes the location of Boulder, CO.

7. Appendix B: Microphysics Temperature Tendency Calculations

7.1 Constants Used in Calculations

Table 7.1: List of constants used in microphysics temperature tendency calculations

Latent Heat of Sublimation, L_s (J kg^{-1} K^{-1})	$\text{lsub} = 2.834 \times 10^6$
Latent Heat of Vaporization, L_v (J kg^{-1} K^{-1})	$\text{lvap} = \text{lvap0} + (2106.0 - 4218.0)\ \text{T(°C)}$ $\text{lvap0} = 2.5 \times 10^6$ [at 0°C]
Latent Heat of Fusion (J kg^{-1} K^{-1})	$\text{lfus} = \text{lsub} - \text{lvap0}$ [L_f] $\text{lfus2} = \text{lsub} - \text{lvap}$ [L_{f2}]
Air Density (kg m^{-3})	$\rho = \frac{0.622\ \text{P}}{\text{R T(K)}\ (Q_v + 0.622)}$
Gas Constant for Dry Air (J kg^{-1} K^{-1})	R = 287.04
Air Pressure (Pa)	P
Water Vapor Mixing Ratio (kg kg^{-1})	Q_v
Heat Capacity of Air at Constant Pressure (J kg^{-1} K^{-1})	$C_p = 1004(1\ + 0.887Q_v)$,
Cloud Ice Mixing Ratio (kg kg^{-1})	Q_i
Cloud Water Mixing Ratio (kg kg^{-1})	Q_c

7.2 "Bulk" Microphysics Terms

Within the Thompson Microphysics scheme in the ARW model, various microphysics processes were included in the calculations for temperature tendencies. These temperature tendencies are used to calculate the accumulated microphysics heating within the model (seen in Figure 3.17). To further investigate which microphysics processes were responsible for the heating profile shape, we manually calculated these temperature tendencies using the same equations found within the parameterization with model output values for P, T, Q_v, and each microphysics process (*mprate*).

The microphysics processes are source/sink terms for a particular hydrometeor species. Within the parameterization they are coded in the following manner (this description is found within the code in Thompson):

- The first two characters are "pr", which represent a source/sink of mass.
- The third character represent the species that is being affected by the process, where "v" = water vapor, "r" = rain, "i" = cloud ice, "w" = cloud water, "s" = snow, and "g" = graupel.
- "The next characters represent the processes: "de" for sublimation/deposition, "ev" for evaporation, "fz" for freezing, "ml" for melting, "au" for autoconversion, "nu" for ice nucleation, "hm" for Hallet-Mossop secondary ice production, and "c" for collection followed by the character for the species being collected."
- "All of these terms are positive (except for deposition/sublimation terms which can switch signs based on super/subsaturation) and are treated as negatives where necessary in the tendency equations."

7.2.1 Sublimation/Deposition Bulk Term

For the "sublimation/deposition" term, the following equation was used to calculate the temperature tendency:

$$\Delta T = L_s \, {C_p}^{-1} \, \rho^{-1} \, mprates \qquad \text{(A1)}$$

The "mprates" or microphysics processes used for this calculation are described in Table 7.2, which also contains the process' given code and mprate number given in the model output.

Table 7.2: List of individual microphysics source/sink terms within bulk "sub/dep" term

	Code	Name	mprate#
"sub/dep"	pri_inu	Condensation freezing (ice nucleation)	mprate25
	pri_ide	Deposition/sublimation of cloud ice	mprate26
	prs_ide	Ice deposition/sublimation as a source/sink of snow	mprate10
	prs_sde	Snow deposition/sublimation	mprate12
	prg_gde	Graupel deposition/sublimation	mprate19

7.2.2 Freezing Bulk Term

For the freezing term, the following equation was used to compute its temperature tendency:

$$\Delta T = L_{f2}\, {C_p}^{-1}\, \rho^{-1}\, mprates \tag{A2}$$

The list of microphysics source/sink terms used in this bulk term is described in Table 7.3.

Table 7.3: List of individual microphysics source/sink terms within bulk "frz" term

	Code	Name	mprate#
"frz"	pri_wfz	Freezing of cloud water into cloud ice	mprate24
	pri_rfz	Freezing of rain water into cloud ice	mprate23
	prg_rfz	Freezing of rain water into graupel	mprate18
	prs_scw	Snow collecting cloud water as a source for snow	mprate8
	prg_scw	Snow collecting cloud water as a source for graupel	mprate22
	prg_gcw	Graupel collecting cloud water as a source for graupel	mprate15
	prg_rcs	Rain collecting snow as a source for graupel	mprate16

	prs_rcs	Rain collecting snow as a source for snow	mprate9
	prr_rci	Rain collecting ice as a source for rain	mprate5
	prg_rcg	Rain collecting graupel as a source for graupel	mprate17

7.2.3 Melting Bulk Term

The temperature tendency equation used for the melting term is the following:

$$\Delta T = L_f \, {C_p}^{-1} \rho^{-1} \, mprates \tag{A3}$$

Table 7.4 describes each microphysics source/sink term within the bulk melting term. All the processes are negative for this term because they are all cooling processes.

Table 7.4: List of individual microphysics source/sink terms within bulk "mlt" term

	Code	**Name**	**mprate#**
"mlt"	-prr_sml	Snow melting as a source for rain	mprate6
	- prr_gml	Graupel melting as a source for rain	mprate7
	- prr_rcg	Rain collecting graupel as a source for rain	mprate4
	- prr_rcs	Rain collecting snow as a source for rain	mprate3

7.2.4 Condensation/Evaporation Term

The temperature tendency for the condensation/evaporation term is calculated using the following equation:

$$\Delta T = L_v \, {C_p}^{-1} \, mprates \tag{A4}$$

Table 7.5 contains a description of each of the microphysics source/sink terms that are used within the calculation. Cloud water evaporation is negative because the values are positive, yet they must represent a sink for cloud water. The rain evaporation processes is negative because it is a cooling process.

Table 7.5: List of individual microphysics source/sink terms within bulk "cond/evap" term

	Code	Name	mprate#
"cond/evap"	prw_vcdc1d	Water vapor condensation	mprate45
	-prw_vcde1d	Cloud water evaporation as a sink for cloud water	mprate46
	-prv_rev	Rain evaporation as a source for water vapor	mprate30

7.2.5 XRI and XRC Terms

These terms are computed in the Thompson microphysics and contribute to the temperature tendency used to calculate the overall accumulated microphysics heating. The temperature tendency associated with the "xri" term will be calculated if the temperature is above 0°C and the value for xri (Equation A6) is greater than zero. Physically, this term acts to instantly melt any cloud ice into cloud water if it is above freezing; the melting takes up heat and thus would generate cooling near the freezing level. The following set of equations is used to calculate the temperature tendency for "xri":

$$qiten = \rho^{-1}\, mprates \tag{A5}$$

$$xri = \max\ (0.0, Q_i + qiten) \tag{A6}$$

$$\Delta T = -L_f\ {C_p}^{-1}\ xri \tag{A7}$$

The microphysics source/sink terms used in Equation A5 are described in Table 7.6.

Table 7.6: List of individual microphysics source/sink terms within bulk "xri" term

	Code	Name	mprate#
"xri"	pri_inu	Condensation freezing (ice nucleation)	mprate25
	pri_ihm	Ice multiplication from rime-splinters (Hallet-Mossop secondary ice production)	mprate27
	pri_wfz	Freezing of cloud water into cloud ice	mprate24
	pri_rfz	Freezing of rain water into cloud ice	mprate23
	pri_ide	Deposition/sublimation of cloud ice	mprate26
	-prs_iau	Autoconversion of cloud ice to snow	mprate11
	-prs_sci	Snow collecting cloud ice as a source for snow	mprate13
	-pri_rci	Rain collecting cloud ice as a source for cloud ice	mprate28

The temperature tendency for the "xrc" term is calculated when the temperature is below the homogeneous freezing temperature (235.16 K) and xrc (Equation A9) is greater than zero. Physically, this term represents the instantaneous freezing of any cloud water found below the homogeneous freezing temperature, which would act to release latent heat into the upper troposphere. Similar to "xri", the equations used to compute "xrc" are as follows:

$$qcten = \rho^{-1}\, mprates \tag{A8}$$

$$xrc = \max\,(0.0, Q_c + qcten) \tag{A9}$$

$$\Delta T = L_{f2}\, {C_p}^{-1}\, xrc \tag{A10}$$

A description of the microphysics source/sink terms used within the "xrc" bulk term can be found in Table 7.7.

Table 7.7: List of individual microphysics source/sink terms within bulk “xrc” term

	Code	Name	mprate#
“xrc”	-prr_wau	Autoconversion of cloud water to rain	mprate29
	-pri_wfz	Freezing of cloud water into cloud ice	mprate24
	-prr_rcw	Rain collecting cloud water as a source for rain	mprate2
	-prs_scw	Snow collecting cloud water as a source for snow	mprate8
	-prg_scw	Snow collecting cloud water as a source for graupel	mprate22
	-prg_gcw	Graupel collecting cloud water as a source for graupel	mprate15

8. Appendix C: Forecast Verification Methods

8.1 Traditional Verification Methods

The traditional verification methods used in this study are the Gilbert Skill Score (GSS), the Heidke Skill Score (HSS), and the frequency bias (FBIAS). These methods make use of a contingency table (Table 8.1), which helps provide information on what errors are being made by the forecast. A perfect forecast would consist of only hits and correct negatives. The skill scores were calculated by using the Grid-Stat tool available in the Model Evaluation Tools (MET) toolkit version 4.1 from Developmental Testbed Center at NCAR. This tool matches the forecast grid points to the observation grid points over a given area of interest for given precipitation thresholds. As described in Section 3.1.4, the precipitation thresholds used for these methods are >12.5 mm, >25 mm, >50 mm, >100 mm, and >150 mm.

Table 8.1: Contingency table used to derive various verification methods

2x2 Contingency Table		Forecasted Event	
		YES	NO
Observed Event	YES	**A (hits)**	**B (misses)**
	NO	**C (false alarms)**	**D (correct negative)**

The GSS is said to be an unbiased version of the Critical Success Index (CSI), which measures the amount of hits to the total amount of forecasts and misses. The CSI tends to depend on the frequency of the event. For example, the CSI would be artificially higher in a climatologically wet environment since it will generally rain more. To eliminate this bias, the

GSS removes the number of hits that arise from random chance. For the GSS: a perfect score would be one, while a "no skill" score would be zero. The HSS measures the fraction of correct forecasts (hits and correct negatives) after removing correct forecasts due to random chance. This skill score can range from negative infinity to one; a negative value meaning a random forecast is better, zero is no skill, and one is a perfect score. The FBIAS measures the amount of events forecasted to the amount of events actually observed. For this method, a value less than one means under forecasting of the event, a value greater than one is an over forecast and a value of one would be a perfect score. The formulas used to calculate the GSS, HSS, and FBIAS are described in Table 8.2.

Table 8.2: Verification methods and their respective formulas

Verification Method	Formula from Contingency Table (Table 8.1)	Range	Description
GSS	$\frac{A-H}{A+B+C-H}$ where H = hits from random chance	$-\frac{1}{3}$ to 1 Perfect score = 1 No Skill = 0	Measure how well observed events were properly forecasted accounting for H
HSS	$\frac{(A+D-E)}{(A+B+C+D-E)}$ where E = expected correct forecasts from random chance	$-\infty$ to 1 Perfect score = 1 No Skill = 0	Measures the accuracy of the forecast compared to random chance
FBIAS	$\frac{A+C}{A+B}$	0 to ∞ Perfect score = 1	Compares the frequency of forecast events to observed events

8.2 Neighborhood Methods

The Forecast Skill Score (FSS) is also computed using the Grid-Stat tool in MET, but does not utilize a contingency table. The FSS is a neighborhood method which compares each forecast grid point to the observed grid point within the given neighborhood. This method gives

credit for forecasts that have small spatial displacement errors. FSS ranges from zero to one, where one is a perfect score (Table 8.3). The neighborhood size used in this study was 9 grid points for the same precipitation thresholds used in the calculation of the "traditional" skill scores.

Table 8.3: Description of Fraction Skill Score

Method	**Formula**	**Range**	**Description**
FSS	$1 - \frac{\frac{1}{N}\sum_N (P_f - P_o)^2}{\frac{1}{N}\left[\sum_N P_f{}^2 + \sum_N P_o{}^2\right]}$ where P_f is the forecast fraction, P_o is the observed fraction, and N is the number of spatial windows in the domain	Complete Mismatch = 0 Perfect Match = 1	Compares the fractional coverage of a forecast to the observations